UNIVERSITÀ
DI SIENA
1240

Dipartimento di Biotecnologie, Chimica e Farmacia

Dottorato di Ricerca in Scienze Chimiche e Farmaceutiche

XXXIII Ciclo

Coordinatore: Prof. Maurizio Taddei

Settore Scientifico-Disciplinare: CHIM/08

PRECLINICAL CHARACTERIZATION OF SFK INHIBITORS, PYRAZOLO[3,4-*d*]PYRIMIDINE SCAFFOLD-BASED DERIVATIVES, FOR CANCER TREATMENT

Tutor

Prof.ssa Elena Dreassi

Dottorando

Enrico Rango

Firmato digitalmente
da RANGO ENRICO
C=IT

Anno Accademico: 2019/2020

This thesis work is dedicated to

Professor Maurizio Botta

ABSTRACT

Pyrazolo[3,4-*d*]pyrimidine derivatives, a promising class of Src family kinase (SFK) inhibitors have been extensively studied by Professor Maurizio Botta research group. They exhibited strong antiproliferative and pro-apoptotic effects on several cancer cell lines.

The first part of this thesis essentially focuses on the preclinical characterization of Si306, a pyrazolo[3,4-*d*]pyrimidine derivative, identified as a very promising anticancer agent. This compound has shown a favorable *in vitro* and *in vivo* activity profile against neuroblastoma (NB) and glioblastoma (GBM) models by acting as a competitive inhibitor of c-Src tyrosine kinase. Nevertheless, the good antitumor activity of Si306 is associated with sub-optimal aqueous solubility, which might hinder its further development. In this context, drug delivery systems were developed to overcome the poor aqueous solubility obtaining suitable formulations for their *in vivo* use in the treatment of NB. Si306 was encapsulated in liposomal nanoparticles: i. Stealth liposomes and ii. Immunoliposomes decorated with AntiGD2 monoclonal antibody, which specifically binds GD2 antigen expressed by NB cells. Both liposomal suspensions resulted stable and showed excellent morphological and physio-chemical properties. The liposomal suspensions exhibited increased cytotoxic activity against different NB cell lines; in particular, AntiGD2-decorated liposomes, due to the interaction with the antigen, showed the ability to bind and be internalized in different NB cells and the cellular association increases proportionally with increasing GD2 antigen expression. The pharmacokinetic (PK) and tissue biodistribution (BD) profiles were evaluated by treating healthy male mice intravenously at two dosages of 5 and 25 mg of Si306/kg of body weight. Higher plasma exposure of Si306 was observed when it is delivered by liposomes compared to Si306 administered in free form. Moreover, an immediate distribution of Si306 followed by a concentration decrease in a time-dependent manner was observed in all organs analyzed. An increased concentration of Si306

was observed in the liver, spleen, and lungs when it is delivered by liposomes. A preliminary PK and BD study on NB orthotopic mouse model demonstrated increased tumor uptake of Si306 when it is encapsulated in liposomes compared to drug-free. Finally, *in vivo* efficacy and survival studies conducted on orthotopic NB mice models revealed the ability of Si306-loaded immunoliposomes to reduce tumor growth and to significantly increase the survival rate.

In the second section, gold nanoparticles (AuNPs) conjugated to Si306 were developed to improve its solubility, but also to increase its ability to cross the blood-brain barrier and to have a therapeutic action against (GBM). This section describes the design, the preparation, and the characterization of AuNPs conjugated with Si306. AuNPs-Si306 showed a good loading efficacy (65%), optimal stability in polar media and human plasma, and a suitable morphological profile. Antitumoral activity of AuNPs-Si306 was evaluated in *in vitro* GBM model, also in combination with radiotherapy (RT). Results demonstrated that AuNPs had a basal radio-sensitization ability and that AuNPs-Si306, when used in combination with RT, was more effective in inhibiting tumor cell growth with respect AuNPs and free Si306.

In the third section, Si409, a pyrazolo[3,4-*d*]pyrimidine derivative, showed the ability to inhibit key members of SFK involved in Diffuse Large B-cell Lymphoma (DLBCL) and to reduce the proliferation of several B-cell tumor cell lines. Also, low cytotoxic activity of Si409 was measured on healthy human peripheral blood mononuclear cells (PBMCs). Si409 showed to be safe by exhibiting a reduction in hERG current but only at concentrations at least 10-fold higher than the median IC_{50} value recorded in tumor cell lines. PK studies showed high phase II metabolism caused by glucuronide conjugation, which reduces plasma levels and increases the clearance of Si409. Despite the low plasma levels, the treatment with Si409 in ABC-DLBCL xenograft mouse model revealed a considerable volumetric reduction of the tumor mass suggesting an interesting *in vivo* pharmacological potency of this compound.

SUMMARY

LIST OF FIGURES

LIST OF TABLES

INTRODUCTION

1. PROTEIN KINASE

The human kinome represents one of the largest gene families that comprise 1.7% of the human genes (Figure 1). 518 protein kinases have been identified and of these, 478 contain a domain of the eukaryotic protein kinase (ePK). The remaining 40, while maintaining kinase activity, lack sequence similarity to the ePK domain. For this reason, they are referred to as the atypical protein kinases (aPKs)[1].

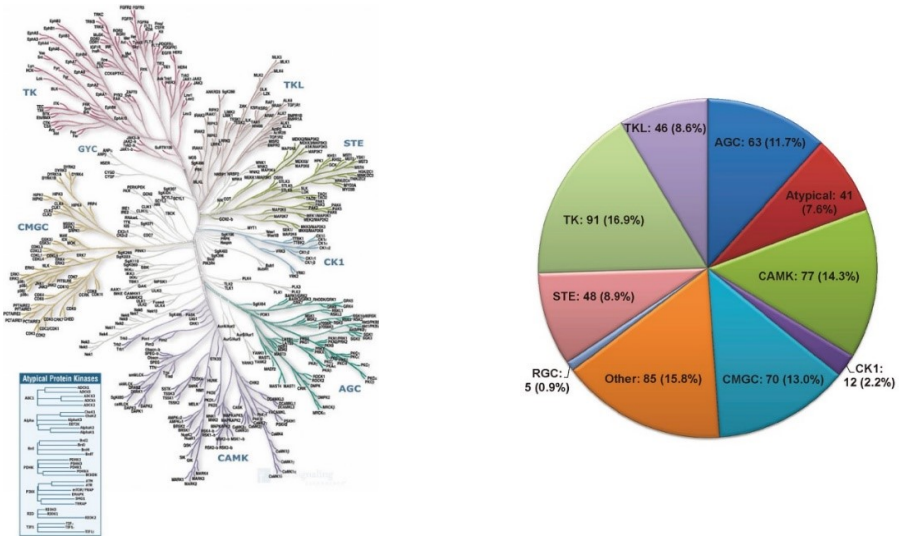

FIGURE 1. Human Kinome.

Kinases catalyze the reversible phosphorylation of about 500,000 phosphorylation sites in more than 20,000 human proteins, playing key roles in human cells as well as other eukaryotic cells[2]. Besides, kinases are involved in several cell signaling pathways, including transcription, tumor cell metabolism, cell cycle progression, apoptosis, and differentiation[3,4]. It has been estimated that more than 400 human diseases are caused by defects in the kinase signaling pathway and more than 80% of kinases have been investigated as targets for therapeutic development.

The ePKs domain is composed of approximately 250 amino acids and contains two lobes: N-terminal lobe (N-lobe) and the C-terminal lobe (C-lobe) which are separated by a cleft that contains residues important for ATP binding as well as phosphate transfer. The ePKs are classified into eight main groups based on

sequence similarity within this domain: I. TK (tyrosine kinase), II. TKL (tyrosine kinase-like), III. STE (STE20, STE11, and STE7 related), IV. CK1 (casein kinase 1), V. AGC (protein kinase A, protein kinase G, and protein kinase C related), VI. CAMK (Ca2+/calmodulin-dependent kinases), VII. CMGC (Cdk, MAPK, GSK, Cdk-like related) and VIII. RGC (receptor guanylyl cyclase)[5].

The TK group includes transmembrane receptor tyrosine kinases (RTKs) and cytosolic non-receptor tyrosine kinases (nRTKs):

- RTKs are transmembrane proteins involved in signaling at the cell membrane. Receptor TKs can be grouped into several subfamilies based on their kinase domain sequences showing a conserved modular structure consisting of an extracellular ligand-binding domain, a membrane-spanning domain, and an intracellular tyrosine kinase domain. The binding of the corresponding ligands to the extracellular domain causes receptor oligomerization and consequent activation of the tyrosine kinase domain causing autophosphorylation of some intracellular tyrosine residues within the receptor protein. At the same time, receptor-dependent phosphorylation of several cytoplasmic signaling molecules may also occur, resulting in the activation of signal transduction cascades. Some examples of members of this family are VEGFR (vascular endothelial growth factor receptor); EGFR/ErbB (epidermal growth factor receptor); PDGFR (platelet-derived growth factor receptor); FGFR (fibroblast growth factor receptor).
- nRTKs represent the remainder of TK group. They are localized in the cytoplasm and function in signal transduction to the nucleus. Some of them possess amino-terminal modifications, such as myristoylation or palmitoylation, which allow them to be anchored to the cell membrane and be activated. In addition to TK domain, nRTKs possess domains that mediate protein-protein, protein-lipid, and protein-DNA interactions. Known members of this group include c-Src, Abl, and JAK kinases.

Deregulation or abnormal activation of TKs can lead to a wide variety of diseases, including cancer, inflammatory disorders, diabetes and neurodegeneration through malignant transformation such as the over-expression of the wild-type receptor or its growth factor ligand, failure of inactivation mechanisms, or trans-activation through receptor dimerization[6].

1.1 SRC TK FAMILY

There are 11 members of the Src kinase family in humans. These include c-Src, Blk, Brk, Fgr, Frk, Fyn, Hck, Hck, Lck, Lyn, Lyn, Srm, and Yes. c-Src, Fyn, and Yes are expressed in all cell types[7]. c-Src is a non-receptor tyrosine kinase that has been studied in recent decades and it plays important roles in cell differentiation, proliferation, and survival. v-Src[7] (a viral protein) is encoded by the oncogene of the Rous sarcoma virus that causes avian cancer, and c-Src (the cellular homologue in humans, chickens, and other animals) is encoded by a physiological gene, the first of the proto-oncogenes. c-Src is expressed ubiquitously; however, in the brain, osteoclasts, and in platelets is expressed 5–200 times more than most other cells[8]. Spliced forms of c-Src are expressed in nerve cells but, there is little evidence of a functional difference among c-Src splice variants[9].

Structurally, from the N- to C-terminus, c-Src contains a myristoyl group at the N-terminal, a unique domain, an SH3 (Src homology 3) domain, an SH2 domain, an SH2-kinase linker, a protein-tyrosine kinase domain called SH1 and a C-terminal autoinhibitory domain (Figure 2). The C-terminal tails (residues 521/524–533/536) of chicken and human Src are identical, but they are completely different from those of Rous v-Src. Myristoylation facilitates the attachment of c-Src to membranes, and myristoylation is required for its operation in cells[7].

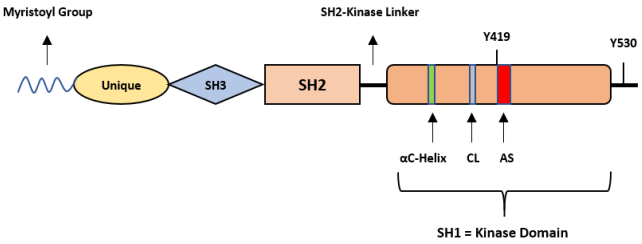

FIGURE 2. Organization of human c-Src[8]. CL, catalytic loop; AS, activation segment.

SH3 domains (≈ 60 amino acid residues) binds to sequences that may adopt a left-handed helical conformation. The SH3 domain is a β-barrel consisting of five antiparallel β-strands and two loops called RT and n-Src loops. These loops are located at either end of a surface composed of aromatic and hydrophobic residues. These sequences adopt a polyproline type II helicoidal conformation which, interacting with the aromatic side chains, complex with the SH3 domain[8].

The SH2 domain (≈100 amino acid residues) consists of a central three-stranded β-sheet with a single helix packed at each side (α1 and α2). The SH2 domain forms two recognition pockets: one coordinates phosphotyrosine and the other binds one or more hydrophobic residues C-terminal to the phosphotyrosine. The phosphotyrosine pocket contains a conserved arginine residue (Arg178 in human c-Src). The human SH2 domain binds intramolecularly to C-terminal pTyr530 that results in inhibition of protein kinase activity[8].

Tyr530 (six residues from the C-terminus) represents one of the two most important regulatory phosphorylation sites in c-Src. *In vivo* basal conditions, 90–95% of c-Src is phosphorylated at Tyr530, which binds intramolecularly with the SH2 domain. SH2 and SH3 binding partners can displace the intramolecular association that stabilizes the dormant form of the enzyme[8].

The SH2 and SH3 domains have four important functions[8]:

1. They constrain the activity of the enzyme via intramolecular contacts.
2. Proteins that contain SH2 or SH3 binding partners can interact with the SH2 or SH3 domains of Src and attract them to specific cellular locations.
3. From the intramolecular displacement of SH2 or SH3 domains, proteins lead to the activation of Src kinase activity.

4. Proteins containing SH2 or SH3 binding partners may preferentially serve as substrates for Src protein-tyrosine kinase.

In general, all protein kinases, including those of the Src family, are associated at two general kinds of conformations (Figure 3). One involves the conversion of an inactive conformation into a catalytically competent form (active conformation). Activation is typically achieved by changes in the orientation of the C-helix in the small lobe and the activation segment in the large lobe. The active kinase then changes from an open to a closed conformation as it passes through its catalytic cycle. The active enzyme, in its open form, binds Mg-ATP and the protein substrate; this is accompanied by conversion to the closed-form while catalysis occurs. After catalysis, the phosphorylated protein (substrate) and then Mg-ADP are released as soon as the enzyme is reconverted to the open form[8]. The activation of c-Src is regulated by a variety of mechanisms and mediated by many upstream kinases and phosphatases. The dephosphorylation of Tyr527 is promoted by various protein tyrosine phosphatase[10] which allow the activation of c-Src. This leads to the structural deployment of c-Src in a conformation that allows the autophosphorylation of Tyr416 residue and the access of substrates to the kinase domain.

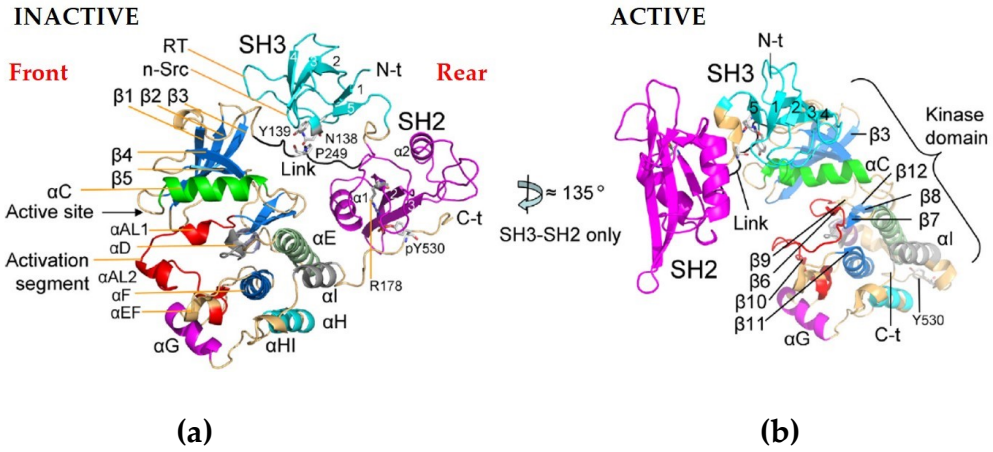

FIGURE 3. Secondary structures of (a) inactive and (b) active c-Src[8]. The SH3 domain is cyan, and the SH2 domain is magenta. C-t, C-terminus; N-t, N-terminus.

c-Src can also be activated by the displacement of the SH3 and SH2 domains mediated by intermolecular interactions with activated TK growth factor receptors,

e.g., EGFR, human epidermal growth factor receptor-2 (HER2), PDGFR, VEGFR, and FGFR[11], integrin cell adhesion receptors[12], steroid hormone receptors, G-protein-coupled receptors, focal adhesion kinase (FAK)[13] and cytoskeleton components.

1.2 c-Src-mediated Pathways in Cancer

In normal cells, c-Src is mostly in the inactive state, being only transiently activated during the essential cellular events to sustain cellular homeostasis in which it is involved and participates in numerous signaling pathways and interacts with several RTKs at the plasma membrane, cytokine receptors, steroid receptors, and G-protein-coupled receptors to regulate and/or promote numerous cellular processes[14]. By this interaction in combination with these molecules, c-Src is involved in the downstream pathways that modulate a wide variety of cellular processes including growth, survival, adhesion, and migration (Figure 4).

By contrast, c-Src activity is elevated in several types of human cancer, having a role in progression, maintenance, and survival in several tumor types: solid cancers as colon[15], breast[16], lungs[17], liver[18], prostate[19], and pancreatic[20] cancers; nervous system cancers, such as glioblastoma multiforme (GBM)[21,22] and neuroblastoma (NB)[23] and hematologic tumors such as chronic myelogenous leukemia[24] and lymphomas[25].

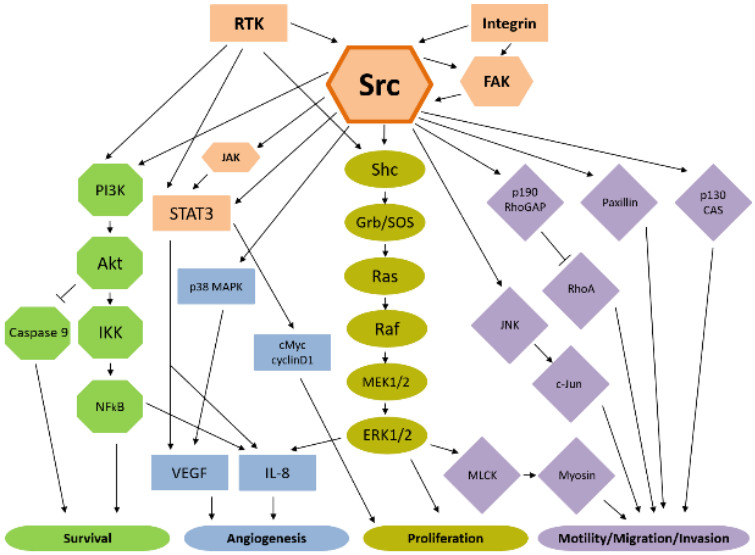

Figure 4. Selected examples of c-Src-mediated pathways.

c-Src activation leads to downstream signaling, indirectly via JAK[26] or directly through the binding to STAT3 (Signal Transducer and Activator of Transcription 3), via its SH2 domain, activating c-myc and inducing the upregulation of cyclin D1. Cyclin D1 and c-myc are involved in the regulation of cell cycle progression. Their upregulation causes cell cycle dysfunction and uncontrolled cell proliferation. Moreover, STAT3, persistently activated, stimulates tumor angiogenesis via overexpression of VEGF, but it also influences other critical angiogenic factors, including angiopoietin, chemokine, and interleukine-8 (IL-8)[27, 28]. Uncontrolled activity of VEGF leads to the formation of interrupted endothelial cell-cell vascular junctions with the consequent increase in vascular permeability, allowing the extravasation of tumor cells. It has been proved that in human solid tumor cell lines, c-Src inhibition reduces VEGF expression, reducing pro-angiogenetic activity[29]. Also, the deregulated activity of Src kinase is involved in anti-apoptotic and pro-survival signal transduction pathways, including those mediated by PI3K and Akt signaling[30]. Moreover, c-Src is involved in an altered regulation process of integrin signals, focal adhesion component proteins[31], and deposition of cell-extracellular matrix (ECM) proteins[32] and can lead to a decreased adhesiveness by disruption of cell-cell adhesion and increased turnover of ECM contacts, thereby promoting tumor cell migration, invasion, and metastasis. Besides, c-Src plays a crucial role in the activity of matrix metallo-proteases (MMPs), which have a well-established role in tumor invasion and cell migration. In particular, it has been demonstrated that the phosphorylation of MT1-MMP (membrane-type 1 matrix metalloproteinase) on its unique tyrosine residue (Tyr573) requires the kinase c-Src[33]. Furthermore, c-Src kinase promotes a critical role in cancer cell proliferation by activation of Ras/Raf/MEK/ERK pathway[34].

2. KINASE INHIBITORS

Protein kinases represent the second most targeted group for drug development, after the G-protein-coupled receptors. This large impact in research is due to their pivotal roles in signal transductions and regulation of a wide range of cellular activities in various types of human diseases and many of these kinases are associated with human cancer initiation and progression.

The development of kinase inhibitors (KIs) for the treatment of human tumors started in the mid-1970s. In subsequent years, the first protein kinase inhibitors (naphthalene sulphonamide scaffold-based) were synthesized, which served as the basis for the subsequent development of further molecules[35]. In 1991 the 3D structure of the protein kinase A (PKA) was resolved and provided clear evidence that the residues involved in the ATP binding were conserved from kinase to kinase[36]. This gave rise to the myth that it was "impossible" to develop inhibitors with a selectivity of action. Finally, in 2001 there was the turning point with the approval by the Food and Drugs Administration (FDA) of imatinib, a pyrimidine phenyl-amino derivative targeting the inactive conformation of the Abl1 kinase, for the treatment of chronic myelogenous leukemia (CML). The clinical targeting of the BCR-ABL gene, formed by the fusion of the ABL gene from chromosome 9 to the BCR gene on chromosome 22, also called the Philadelphia chromosome, has improved the clinical management of leukemia patients[37]. Since the initial development of imatinib, 28 kinase inhibitors have been FDA approved with Brigatinib and Osimertinib as the latest approvals. Apart from the approved kinase inhibitors, more than 3,000 Phase I-III clinical trials are underway for hundreds of new kinase inhibitors[38].

Initially, small molecule protein kinase inhibitors were divided into three classes: type I, small molecules that bind to the active conformation of a kinase in the ATP pocket; type II, small molecules that bind to an inactive (usually Asp-Phe-Gly, DFG-out) conformation of a kinase; and type III KIs, non-ATP competitive inhibitors or allosteric inhibitors[39].

Later, other parameters were introduced by classifying the kinase inhibitors into[38]:

- Type I: represent ATP-competitors that mimic the purine ring of the adenine moiety of ATP and interact with the conformational phosphorylated active catalytic site of the kinases. To date, many type I KIs for the treatment of cancer have been approved by the FDA including bosutinib, dasatinib, erlotinib, gefitinib, lapatinib, pazopanib, ruxolitinib, sunitinib, and vemurafenib. But these kinase inhibitors also have negative side effects showing a low selectivity, since the ATP pocket is conserved through the kinome. This low selectivity for targeted kinases may result in cardiotoxicity.
- Type II: kinase inhibitors that act by targeting the inactive conformation of kinases and interact with the catalytic site of the unphosphorylated inactive conformation of kinases. These inhibitors interact reversibly with the target kinase which leads to the formation of single or multiple hydrogen bonds with the protein in the 'hinge region' and causes extra interactions in the open DFG-out conformation. These interactions have a high degree of selectivity affecting an increase in the safety profile. This class includes imatinib and nilotinib.
- Type III (or allosteric inhibitors): this class of KIs binds outside the ATP-binding site and modulates kinase activity in an allosteric manner and exhibits the highest degree of target kinase selectivity (e.g. trametinib). This class is also divided into two subtypes: type A inhibitors bind to an allosteric site next to the adenine-binding pocket whereas the type B inhibitors bind elsewhere.
- Type IV (also called substrate-directed inhibitors): they act through a reversible interaction outside the ATP pocket, located in the kinase substrate-binding site. These inhibitors do not compete with ATP and offer a higher degree of selectivity (e.g., ON012380, which is targeted against Philadelphia chromosome-positive leukemias).

- Type V (or covalent inhibitors): this class of molecules acts as KIs through the irreversible covalent bond with a cysteine residue within the active site of the enzyme. Afatinib and ibrutinib are currently FDA-approved drugs.

Structurally, the currently FDA-approved small molecule KIs consist of a small number of nitrogen-containing compounds such as quinazolines, quinolines, isoquinolines, pyrimidines, and indoles. KIs represent a new and improved step toward targeted therapy and toward a new generation of anticancer drugs. Nevertheless, at present, KIs serve more as second- or third-line therapies rather than as primary therapy, being useful in combination with traditional chemotherapy.

2.1 c-Src Inhibitors

c-Src inhibition may play an important auxiliary role in various cancer treatments since it is involved in many pathways promoting survival and cell proliferation. For this reason, in the last decades, extensive work on the development of c-Src inhibitors has been performed.

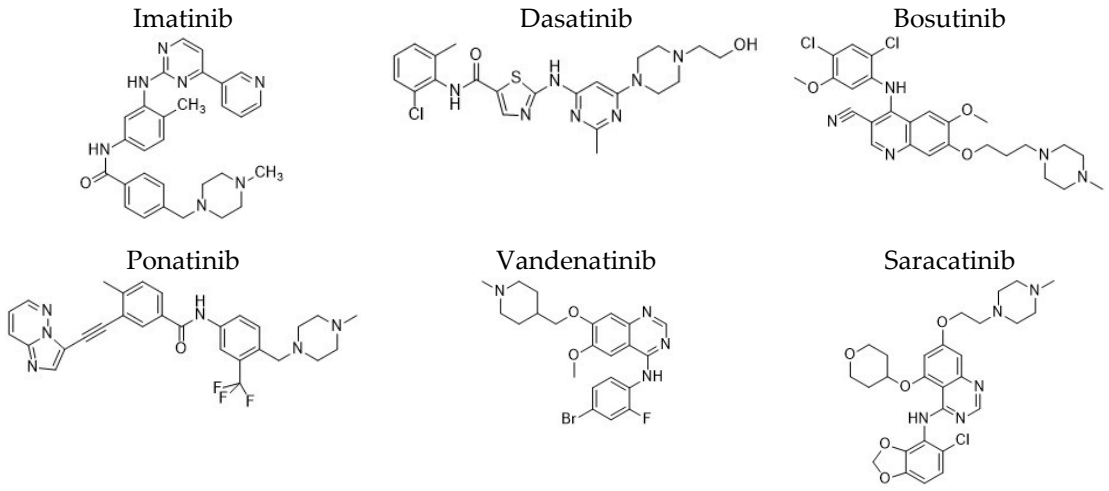

Figure 5. Chemical structures of some c-Src/multi-kinase inhibitors.

Four orally effective c-Src/multi-kinase inhibitors are FDA-approved for the treatment of various malignancies (Figure 5): (I) Bosutinib is a PDGFR, BCR-Abl, c-Src (and others SFKs such as Lyn, Hck, and Kit) inhibitor approved for the treatment of Ph+ CML and lymphoblastic leukemias (ALL). It is currently in clinical trials for the treatment of glioblastoma and breast cancer[8]; (II) Dasatinib is an inhibitor of

BCR-Abl, c-Src, Lck, Fyn, Yes, PDGFR, and other kinases that is approved for the treatment of CML. This drug is undergoing phase I and II of the clinical trials as a monotherapy and in combination for various solid malignancies and ALL[8,40]; (III) Ponatinib is an inhibitor of BCR-Abl, PDGFR, VEGFR, Src family, and other kinases that is approved for the treatment of CML and ALL. It too is undergoing clinical trials for several solid tumors[8]; (IV) Vandetanib is an inhibitor of EGFR, VEGFR, RET, Src family, and other kinases approved for the treatment of medullary thyroid carcinoma, and it too is in clinical trials for numerous solid tumors[8].

Several TK inhibitors are currently in phase II/III clinical trials in solid tumor patients. An example, is Saracatinib (AZD0530), another orally active with high selectivity against c-Src-Abl that has shown promising preclinical and clinical results for colorectal, gastric, ovarian, small cell lung cancers, non-small cell lung cancer (NSCLC), and metastatic osteosarcoma in lung[40].

2.2 PYRAZOLO[3,4-*d*]PYRIMIDINES

The earliest SFK inhibitors with a pyrazolo[3,4-*d*]pyrimidine scaffold-based were PP1 and PP2 (Figure 6). However, these inhibitors suffered from toxicity and poor selectivity[41].

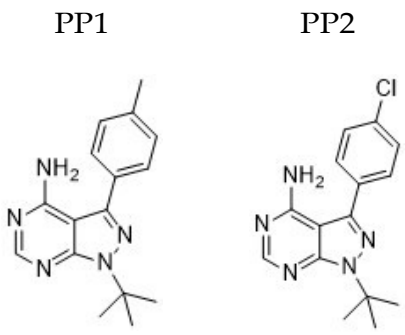

FIGURE 6. Chemical structures of PP1 and PP2, the first SFK inhibitors.

In the last years, the research group of Professor Maurizio Botta has developed a huge library of pyrazolo[3,4-*d*]pyrimidines compounds, which thanks to their isosterism with adenine, have been found to act as ATP-competitive SFK inhibitors. This class of compounds became an attractive target for the development of new

therapeutic agents against cancer, thanks to their capacity to inhibit several oncogenic tyrosine kinases (TKs). The first small group of pyrazolo[3,4-*d*]pyrimidines synthesized has been published in 2004. This work reported some compounds which inhibitory activity against c-Src and towards cell proliferation for A-431 (epidermoid carcinoma cell line)[42]. Ever since then, a wide library of compounds has been synthesized and several members were found to induce apoptosis and to reduce proliferation in different cell lines in which c-Src is overexpressed or overactivated, both from solid tumors (osteosarcoma[43], prostate[44], neuroblastoma[45,46,47], glioblastoma multiforme[48,49,50], rhabdomyosarcoma[51], mesothelioma[52], medulloblastoma[53], medullary thyroid carcinoma[54]) and hematological tumors (leukemia[55] and Burkitt lymphomas[56]).

Several members of this family showed an interesting dual Abl/c-Src inhibition and antiproliferative activity towards human leukemia cell lines[57]. Two compounds, Si163 and Si223 (Figure 7a and 7b, respectively) have been able to inhibit the Bcr-Abl T315I mutant. Moreover, they have shown a more than 50% reduction in tumor volumes in xenograft murine model inoculated with 32D-T315I cells[58]. S13 (Figure 7c) represents another compound that has shown great interest. It showed a synergic activity in combination with paclitaxel (PTX) against hormone-insensible prostate cancer both in *in vitro* cytotoxicity test and *in vivo* PC3 xenograft mouse model (subcutaneous)[59].

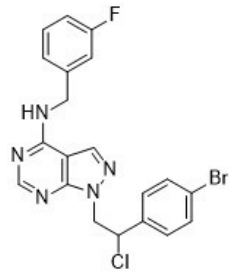

c-Src Ki = 0.045 μM
Abl Ki = 0.055 μM
Abl T315I Ki = 0.036 μM

(a)

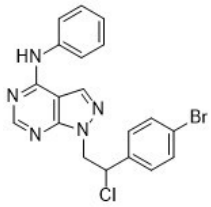

c-Src Ki = 0.064 μM
Abl Ki = 0.610 μM
Abl T315I Ki = 0.090 μM

(b)

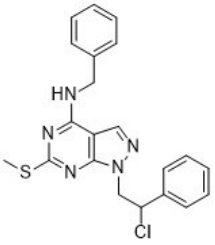

c-Src Ki = 3.0 μM

(c)

FIGURE 7. Structure and inhibitory activity of pyrazolo[3,4-*d*]pyrimidines: (a) Si163, (b) Si223 and (c) S13.

Despite the considerable activity of these compounds, their further development is precluded by their low water solubility and unfavorable ADME profiles. Therefore, to improve this aspect, a series of more soluble pyrazolo[3,4-*d*]pyrimidine derivatives have been designed and synthesized through the introduction of polar groups. Starting from the hit compound Si214 (Figure 8)[57], which showed good activity but low solubility, studies led to the identification of the compound Si192 (Figure 9), which showed both an improved *in vitro* ADME profile and a potent inhibitory activity against the isolated c-Src[45].

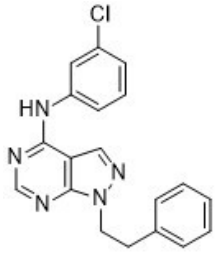

c-Src K_i = 0.09 μM

Solubility μg/mL	PAMPA P_{app} 10^{-6} cm/sec	Met. Stab. Human %
0.12	0.2	99

PAMPA: Parallel Artificial Membrane Permeability Assay;
Papp: apparent permeability;
Metabolic stability in presence of human microsomes is expressed as percentage of unmodified drug.

FIGURE 8. Si214: chemical structure and *in vitro* ADME properties.

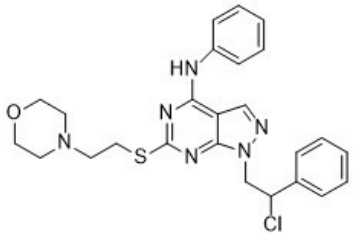

c-Src K_i = 0.21 μM

Solubility μg/mL	PAMPA P_{app} 10^{-6} cm/sec	Met. Stab. Human %
1.7	10.0	95

FIGURE 9. Si192: chemical structure and *in vitro* ADME properties.

Subsequently, computational and structure-activity relationship (SAR) studies led to the identification of the compound Si306 (Figure 10) as the best candidate for development against NB[45] and GBM[49], due to its favorable *in vitro* ADME properties and its c-Src inhibiting activity with a Ki value in the order of sub-micromolar[45].

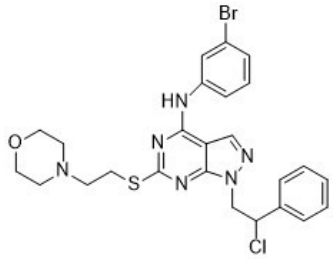

c-Src K_i = 0.13 μM
Abl K_i = 0.12 μM

Solubility μg/mL	PAMPA P_{app} 10^{-6} cm/sec	Met. Stab. Human %
3.7	5.3	96

FIGURE 10. Si306: chemical structure and *in vitro* ADME properties.

In the last years, a prodrug approach has been applied to overcome the real problem that characterizes this class of compounds, namely, aqueous solubility[50]. The position selected to design prodrugs is represented by the secondary amine in position C4, as it represents the moiety shared by most of the pyrazolo[3,4-*d*]pyrimidines already synthesized. Furthermore, as already widely demonstrated by computational studies, the -NH group in position C4 is essential for interactions within the ATP-binding site of TKs. Taken the water solubility issue into account, a N-methylpiperazino moiety, protonated at physiological pH (pKa 9.27 ± 0.1) and characterized by high water solubility (molar solubility 9.98 mol·L^{-1}, pH 7), was chosen. All the synthesized prodrugs were demonstrated to have higher water solubility when compared with parental drugs with a consequent increase in their bioavailability and biological activity. Among them, Pro-Si306 (Figure 11), the prodrug of Si306, has been selected as the most promising for its good aqueous solubility, favorable hydrolysis in human plasma, and an increased ability to cross cell membranes.

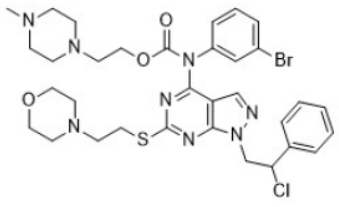

c-Src K_i > 100 μM
Abl K_i > 100 μM

Solubility μg/mL	PAMPA P_{app} 10^{-6} cm/sec	Met. Stab. Human %	Plasma half-life (h)
8.7	2.1	94	3.48

FIGURE 11. Pro-Si306: chemical structure and *in vitro* ADME properties.

In a recent work published in June 2019, the role of Si306 and Pro-Si306 as dual c-Src/P-gp inhibitors was investigated[60]. The tested compounds were found to increase the intracellular accumulation of Rho 123 (used as P-gp substrate probe for characterizing P-gp inhibitory potential), and to enhance the efficacy of paclitaxel in P-gp overexpressing cells (multidrug-resistant U87-TxR cell line). In addition, Si306 and Pro-Si306 interaction with CYP3A4 isoform was assessed *in vitro* and no significant inhibition was promoted at the highest concentration used. Protein-binding profile to HSA (human serum albumin) and AGP (α-1-acid glycoprotein) was also evaluated showing for both Si306 and its prodrug one-site binding kinetics. Si306 displayed a high affinity for HSA and AGP (K_D 0.35 and 11.49 μM respectively). On the other hand, Pro-Si306 demonstrated a lower affinity for HSA (K_D 21.45 μM) and comparable values for AGP (K_D 9.28 μM) in confront to Si306. Pharmacokinetic (PK) profile of Si306 was studied after i.v. (25 mg/kg) and *per os* (50 mg/kg) administration in healthy mice (see Table 1 and Figure 12 for PK results).

TABLE 1. Pharmacokinetic parameters for Si306[a].

Parameters	Unit	PLASMA	
Route		i.v.	*per os*
Dose	mg/kg	25	50
C_{max}[b]	μg/mL	25.45	2.97
T_{max}[c]	h	0.08	1.5
$MRT^{d}_{0\rightarrow\infty}$	h	3.78	5.70
$AUC^{e}_{0\rightarrow\infty}$	μg/mL×h	22.75	15.17
$AUC^{e}_{0\rightarrow24h}$	μg/mL×h	22.30	14.48
$V^{f}_{z/F}$	L/Kg	8.17	28.32
$CL^{g}_{z/F}$	L/h/Kg	1.10	3.29
$t_{1/2}$[h]	h	5.15	5.96

[a]Calculated with PKSolver; [b]C_{max}: maximum concentration observed. [c]T_{max}: time of maximum concentration observed. [d]MRT: mean residence time. [e]AUC: area under the curve. [f]V: volume of distribution. [g]CL: clearance. [h]$t_{1/2}$: half-life. PK data were evaluated using a non-compartment model.

Si306 was rapidly absorbed with a C_{max} of 2.97 μg/mL after 1.5 hours (T_{max}) while the observed C_{max} for i.v. treatment was 8.5 times higher. The plasma half-life ($t_{1/2}$)

also remains in the same range of values being 5.15 h and 5.96 h after i.v. and *per os* administration, respectively. Interestingly, after oral administration a large amount of Si306 has been detected (10.65 μg/g) into the brain after 30 min, then the concentration slowly decreased during the next 24 hours (Figure 12). An immediate distribution followed by a fast concentration decrease in a time-dependent manner was also observed for the liver and kidneys when Si306 was administered intravenously. On the other hand, orally administered Si306 showed its C_{max} in the liver and kidneys at 1.5 h and 2 h respectively.

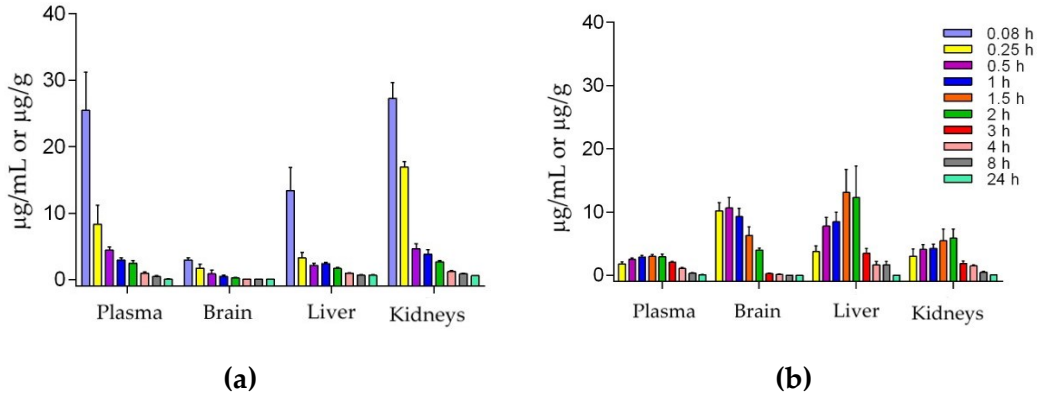

(a) **(b)**

FIGURE 12. PK of Si306 (mean ± S.E.M., n=5, plasma: μg/mL; tissues: μg/g). Distribution in mice tissues after i.v. administration over 24 h **(a)**. Distribution in mice tissues after *per os* administration over 24 h **(b)**.

Finally, the acute toxicity study was performed to provide useful information concerning the effect of acute exposure of test animals to high doses of the Si306. Treatment of mice with Si306 did not produce treatment-related mortality at the limit test dose (100 mg/kg), and besides, throughout the four days observation period, no significant changes occurred in the behavior. Moreover, no microscopic alterations were found in the brain, liver, and kidney (Figure 13).

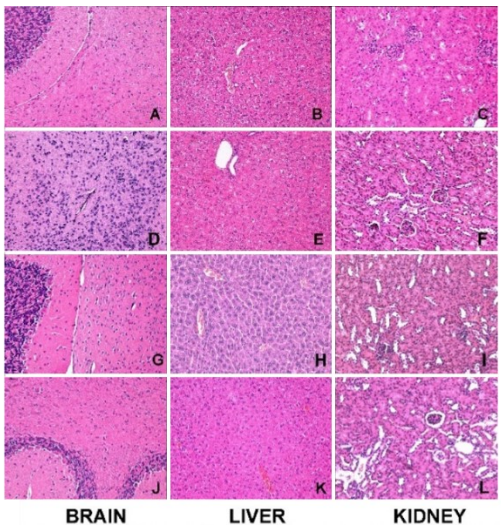

FIGURE 13. Microscopic analysis of tissues after Si306 administration in mice. Representative microscopic pictures (200X magnification) of untreated mice (A, B and C); mice treated with only vehicle (D, E and F); mice treated with dose level of 50 mg/kg of Si306 (G, H and I) and mice treated with the dose level of 100 mg/kg of Si306 (J, K and L).

Subsequent optimization studies resulted in novel pyrazolo[3,4-*d*]pyrimidine derivatives. Among these derivatives, Si409[47] (Figure 14) emerged for its favorable aqueous solubility (134.2 μg/mL) and high *in vitro* metabolic stability (99.4 %). Moreover, Si409 showed a low Ki value against c-Src (300 nM) and an interesting antiproliferative activity on neuroblastoma SH-SY5Y cell line.

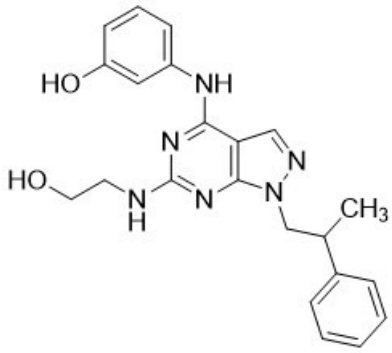

FIGURE 14. Chemical structure of Si409.

2.3 SFK INHIBITORS IN CANCER THERAPY

The role of SFK in the brain and neuronal tumors is not as extensively studied as solid tumors deriving from the breast, lung, colon, prostate, or pancreas. However, neuronal tissues do exhibit increased expression of c-Src and Fyn, and these proteins likely play a role in the proliferation and growth of tumors arising in the nervous system[61]. This paragraph will focus on the role of SFKs in the development and progression of two solid tumors arising from the nervous system: GBM and NB and in neoplasms involving the lymphoreticular system, large diffuse B-cell lymphomas (DLBCL).

2.3.1 GLIOBLASTOMA MULTIFORME

In the past two decades, there has been a tremendous influx of data describing genomic alterations in gliomas and particularly in GBM, which is the most aggressive malignant form of primary brain tumor (WHO grade IV) with an extremely poor prognosis: a 1-year and 5-years survival rate of 35.7% and 4.7%, respectively[62]. Since its low incidence rate, it is considered an orphan disease with an annual prevalence of 1-9/100,000 people[63]. The standard-of-care is surgical resection followed by adjuvant radiotherapy combined with chemotherapy. Temozolomide (TMZ) is an alkylating agent and represents the first line in treatment.

Investigators have found elevated c-Src activity in various CNS tumors, including GBM, compared with normal brain samples[64] (c-Src activity/phosphorylation is elevated in GBM samples and cell lines, including T98G and U87)[65]. In preclinical GBM models, c-Src inhibition reduces cell proliferation and viability and increases glioma cell apoptosis[65]. Also, c-Src inhibition reduces vessel density and VEGF-induced vascular permeability. The role of Src in GBM development was further supported by a study in transgenic mice expressing v-Src. These mice spontaneously developed low-grade tumors that progressed to a morphology resembling human GBM (14% of mice at 65 weeks)[66]. Many studies also showed that Src is activated in primary GBM patient samples[67].

Taking together all these evidences supporting the role of SFKs in glioma biology, it is hardly surprising that the number of clinical trials for SFK inhibitors for the treatment of GBM had exponential growth in recent years.

2.3.2 NEUROBLASTOMA

Neuroblastoma represents the most common extracranial solid tumor of neuroectodermal origin in pediatric patients. These tumors originate from primitive sympathetic ganglion cells. Neuroectodermal cells that comprise the tumor arise from the neural crest during neurodevelopment in utero[68]. Neuroblastoma tumors originate anywhere along the sympathetic chain but most often in the adrenal glands (40%), in the abdomen (25%), thorax (15%), or within pelvic sympathetic ganglia (10%). Long-term survival is only about 40% in patients with high-risk, defined by age above 18 months and disease dissemination or unfavorable histologic markers. To treat neuroblastoma, a multimodal approach is typically implemented, involving a combination of surgical resection (for primary tumors that have clear localization and well-defined borders), radiotherapy, chemotherapy, and endocrine or biological therapy[69]. Radiation therapy in neuroblastoma is utilized when tumors are unresectable or unresponsive to chemotherapy.

Several studies reported a correlation between c-Src overexpression and the ability of NB to differentiate *in vitro* and *in vivo*[70]. NB cell lines have been shown to express c-Src at levels much higher than that observed in primary cultures from noncancerous tissues[71]. The same is also true for many other neuroendocrine tumors, where c-Src was found to be in correlation with the differentiation state of the tumor[72]. Besides, overexpression of the c-Src kinase in advanced NB patients has been associated with poor outcome[73].

Inhibition of c-Src activity by dasatinib and bosutinib resulted in decreased cell proliferation and apoptosis induction in NB cells and demonstrated anti-tumor efficacy in NB mice models[74,75]. Therefore, targeting c-Src tyrosine kinase may represent a promising solution in NB therapy.

2.3.3 Diffuse Large B-cell Lymphoma

Lymphomas are neoplasms involving the lymphoreticular system. Depending on their origin, B-cell, T-cell, and NK- (natural killer) lymphomas can be distinguished[76]. Lymphomas can be further divided according to the rate of growth into indolent lymphomas: such as follicular lymphoma and cutaneous T-cell lymphoma (CTCL) and aggressive lymphomas: such as diffuse large B-cell lymphoma (DLBCL) and peripheral T-cell lymphoma (PTCL). In addition, based on histology, lymphomas are classified into non-Hodgkin's lymphoma (NHL) and Hodgkin's lymphoma (HL), the first ones represent 90% of all malignant lymphoma[77].

In B- or T-cell-derived lymphomas, deregulation of signaling pathways downstream of B- or T-cell receptors is often observed, and several members of the SFKs play a critical role, as demonstrated by several studies highlighting how simultaneous inhibition with masitinib of the three SFKs leads to complete blockade of oncogenic B-cell receptor (BCR) signals in GCB (germinal center B-cell) and ABC (activated B-cell) DLBCL cells[78,79]. Moreover, inhibition was effective not only on lymphoma cell lines but also in patient-derived xenograft models[80].

A reduction in cell growth in cells expressing activating mutations of Fyn in PTCL (Fyn Tyr531His) was observed with dasatinib treatment[81].

Besides, a study conducted in CTCL (another form of T-cell lymphoma) showed the involvement of Blk[82] and, several subsequent *in vitro* and *in vivo* studies confirmed this observation through the inhibition of CTCL proliferation after treatment with dasatinib[83,84].

3. CANCER BIOMARKERS AND GD2 EXPRESSION

Biomarker research is a way to understand the disease by providing information, other than traditional chemotherapy, on aberrant and signaling cellular processes. A characteristic of cancer cells is that proteins are sometimes over- or under-expressed relative to healthy cells. In recent years, cancer-specific protein overexpression has been the focus of the new drug development research. While both intracellular and extracellular proteins can serve as biomarkers and potential drug targets, surface-expressed proteins are being utilized to develop new targeted therapies using antibodies and drug delivery systems. For example, bevacizumab is an antibody that specifically binds VEGF and is being utilized for cancer therapy in patients with colorectal cancer, lung cancer, renal cell carcinoma, and some aggressive brain tumors[85,86].

Targeting by specific antibodies is expanding from tumor-specific protein expression to characteristic lipids and macromolecules found in tumor cells. One such example is the cancer biomarker GD2, a specialized lipid expressed by tumors of neuroendocrine origin (e.g., melanoma, ganglioneuroma, and neuroblastoma)[87,88]. GD2 is a ganglioside composed of a glycosphingolipid specifically modified with two sialic acid groups[89]. Gangliosides naturally are expressed in all vertebrate tissues and are present on the surface of cell membranes in which they are involved in multiple processes such as cell recognition and signal transduction[90,91]. Gangliosides are abundantly present in the central and peripheral nervous system where they interact with lectins and myelin-associated glycoproteins thus ensuring optimal axon-myelin cell-cell interaction, long-term axon-myelin stability, and inhibiting axon outgrowth after injury[92]. The highest levels of gangliosides expression are seen during the early stages of neurological development[93]. Alterations in the gangliosides synthesis pathways in cancer can result in high levels of gangliosides such as GD2, GD1, and GT1 in particular types of cancer[94].

Gangliosides GD2 and GD3 have been identified in the surface adhesion domains of melanoma cells and contribute to mediate adhesion of melanoma. In NB tumor cells, they interact and modulate receptors for the extracellular matrix[95,96].

3.1 ANTIGD2 AND IMMUNOTHERAPY

Since the '70s and '80s antibodies have been studied and developed in the oncological field by exploiting their binding to cancer cells, thus allowing white blood cells to target tumor cells after activation with cytokines (e.g. interleukin-2, IL-2)[97,98]. Since then, in immunotherapy, monoclonal antibodies (mAbs) have been intensively studied thanks to the simultaneous discovery of several biomarkers associated with tumors[99]. The production of mAbs is due to the inventors Georges J. F. Köhler and César Milstein in 1975 (Nobel Prize for Medicine and Physiology in 1984).

The monoclonal antibody, 3F8, which specifically binds GD2 glycolipid, was the first to be isolated after immunization of mice with lysates of neuroblastoma cells without showing cross-reactivity to other similar gangliosides such as GD1, GT1b, or GM1a[100,101]. GD2 is uniformly expressed by neuroblastoma cells in high amounts. In normal cells, its expression is limited to cells of neuroectodermal origin, including the central nervous system and peripheral nerves[102].

When AntiGD2 binds to the GD2 antigen on the surface of tumor cells, it induces cell lysis through antibody-dependent cell-mediated cytotoxicity (ADCC) and complement-dependent cytotoxicity (CDC). Because GD2 is found on some healthy nerve cells, AntiGD2 binds to those cells, causing pain[103,104].

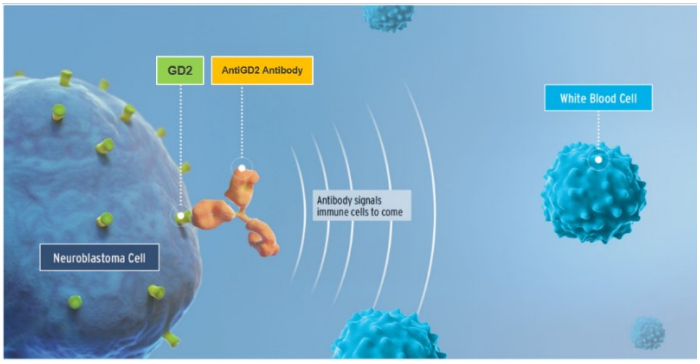

FIGURE 15. AntiGD2 monoclonal antibody that induces tumor cell lysis via multiple mechanisms.

3F8 is the first antiGD2 mAb tested in humans and developed for the treatment of neuroblastoma. A single-arm study showed that the use of 3F8 in combination with IL-2 and cytokine granulocyte-macrophage colony-stimulating factor (GM-CSF) in patients with stage 4 neuroblastoma increased 5-year progression-free survival of 62% compared to conventional treatments leading to less than 40% survival[68,105]. Also, a phase II clinical trial combining 3F8 with GM-CSF showed complete remission of bone marrow disease in 80% of 19 patients resistant to neuroblastoma chemotherapy[106].

Despite encouraging clinical results, most successes with 3F8 immunotherapy were observed as tertiary therapy in patients with the minimal residual disease compared to bulky tumor masses[107]. In addition, patients with repeated 3F8 therapies in short periods of time develop human anti-mouse antibodies (HAMA) against 3F8 antibodies, causing a decrease in anti-tumor efficacy and limiting the frequency of possible 3F8 doses[105].

Genetic techniques have been employed to humanize 3F8 antibodies and other antiGD2 antibodies such as ch14.18 by replacing mouse-specific residues with human antibodies[108]. Humanized antibodies (prefixed "hu") such as hu14.18 and hu3F8 were found to decrease the presence of HAMA, although HAMA still interferes with repeated doses[109]. Dose limitation features of 3F8 include off-target effects and inactivation by the patient's immune system. 3F8 immunotherapy is associated with significant pain and pain-associated hypertension, probably due to off-target effects due to the presence of GD2 on peripheral nerves[110]. Vascular

problems have also been observed in which blood vessels temporarily lose the ability to maintain volume, resulting in the inefficiency of gas exchange, or hypoxia[111].

Basis on the side effects profile, the need to use additional immunomodulators, and dose-limiting immune responses, there is a necessity to enhance antiGD2 immunotherapies more effectively at lower dosages.

4. NANOTECHNOLOGY IN MEDICINE

Medical nanotechnology is the use of several types of nanoscale-sized systems (1–1000 nm), which are constructed on inorganic (e.g., gold, iron oxide, lanthanide ions, and carbon nanotube) or organic materials (e.g., liposomes, micelles, dendrimers, cyclodextrins) that have nanoscale properties for medical applications and allow for encapsulation of multiple therapeutic agents (e.g., small molecules, peptides, nucleic acids).

In chemotherapy very often there are problems of toxicity (due to poor selectivity of the chemotherapeutic agent) and poor PK profiles or non-specific drug distribution in tissues and organs. All these factors can lead to failure of the treatment. Based on these considerations, the development of pharmaceutical formulations, based on nanoparticles, has demonstrated many benefits by enhancing drug delivery in the tumor site and reducing side effects.

4.1 LIPOSOMES

Liposomes (discovered by Alec D. Bangham in 1963[112]), thanks to their ease of preparation, versatility, and low cost, soon became the most used nanostructure in drug delivery.

Liposomes are spherical vesicles prepared from phospholipids of both natural and synthetic origin. They consist of one or more lipid bilayers enclosing an internal aqueous space. They are used in various pharmaceutical applications thanks to their ability to encapsulate both hydrophilic (in the aqueous core) and hydrophobic (in the lipid bilayer) compounds. Also, liposomes are biodegradable, biocompatible, and non-toxic, being made up of phospholipids. The main advantages of using liposomes as drug delivery systems are: enhancing the solubility of drugs when there are solubility problems and therefore, difficulties in administering a drug systemically, functioning as a sustained release system, providing targeted drug delivery, reducing drug side effects, providing protection against drug degradation, enhancing the half-life of a drug when it shows rapid clearance or strong metabolism and, also, being effective in overcoming drug resistance[113]. Several factors define the liposome properties: lipid composition, number of lipid bilayers (unilamellar or multilamellar), size (between 0.025 μm and 2.5 μm), surface charge, preparation method. It is also possible to use surface functionalization of liposomes with a variety of agents to improve the system for specific aims. Liposomes can be functionalized with polyethylene glycols (PEGs) to obtain so-called stealth liposomes (long-circulation), aptamers, antibodies, proteins, peptides, ligands, carbohydrates, or small molecules (ligand-targeted stealth liposomes)[114] (Figure 16).

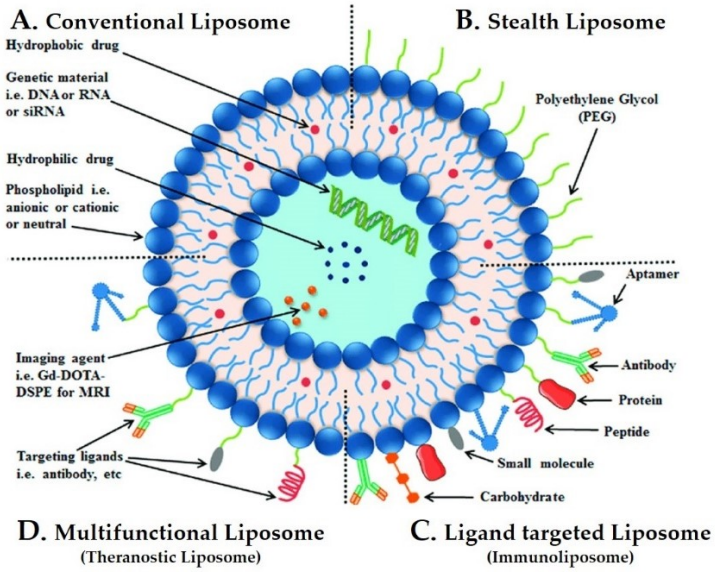

FIGURE 16. Structure of liposomes[114]: (a) conventional liposomes; (b) PEGylated/stealth liposomes; (c) targeted liposomes containing a specific ligand to target a cancer site; and (d) multifunctional liposomes, which can be used for diagnosis and treatment of solid tumor.

Doxil®, the first FDA-approved lipid vector of lipid vesicles, is the DNA intercalating agent, doxorubicin, encapsulated within lipid vesicles of approximately 100 nanometers in diameter[115]. It was introduced into the market in 1995 for the treatment of ovarian cancer and Kaposi's sarcoma. Subsequently, in 1996, DaunoXome® was introduced for the administration of daunorubicin and FDA approved for the treatment of advanced HIV-associated Kaposi's sarcoma. Over the years, several liposomal pharmaceutical products have been developed and marketed such as Mepact® and Myocet®. Recently Onivyde™, a liposomal product that carries fluorouracil and leucovorin for the treatment of metastatic adenocarcinoma of the pancreas, has been approved.

Several liposomal formulations are in phase I/II/III clinical trials, such as Lipoplatin™, containing Cis-platin and LEP-ETU, containing Paclitaxel[116].

4.1.1 STEALTH LIPOSOMES AND EPR EFFECT

One of the major drawbacks of conventional liposomes is their rapid elimination from the bloodstream. This is due to the recognition of the "naked" phospholipid membrane by plasma proteins (opsonins), triggering recognition and uptake of liposomes by the mononuclear phagocyte system (MPS), also known as the reticuloendothelial system (RES) (Figure 17). To overcome this limitation of conventional liposomes, sterically stabilized liposomes (Stealth®) have been developed through the conjugation of phospholipids (which make up the bilayer) with polymers, such as PEG, allowing this new generation of liposomes to evade MPS recognition. The inclusion of PEG or other hydrophilic polymers extends the liposome half-life from less than a few minutes to several hours. This circulation longevity is due to the ability of the hydrophilic chains of PEG to provide a "steric stabilization": PEG molecules enhance the repulsive capacity of polymer-coated liposome surface to render them impermeable to large molecules or opsonins. This effect is due not only to the molecular mass of the bound polymer and its uniformity ("molecular cloud") but also to its remarkable conformational flexibility[117].

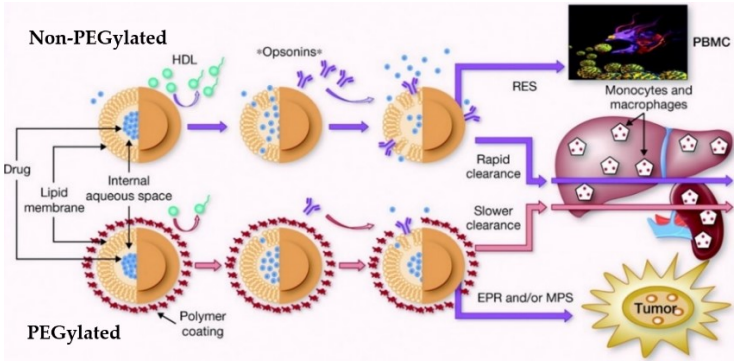

FIGURE 17. Clearance of PEGylated and non-PEGylated liposomes via the MPS. Primarily they are cleared via the monocytes, macrophages, and dendritic cells of the MPS located in the liver, spleen, and blood (in the lung and bone marrow also seem to be involved). The tumor delivery of liposomes is determined by the EPR effect and potentially MPS in tumors.

Through passive targeting, stealth liposomes can preferably be concentrated in the tumor through the permeability and enhanced retention (EPR) effect of the vasculature (Figure 17). The rapidly forming tumor blood vessels are characterized by a highly chaotic organization to obtain large amounts of oxygen and nutrients

necessary for survival and rapid proliferation. The tumor vessels have a pore size between 100-780 nm; thus, the liposomes are small enough to pass from the bloodstream to the interstitial space of the tumor. On the other hand, normal tissue junctions are <6 nm[118] and are impermeable to liposomes and other particles of this diameter. This differential accumulation of liposomal drugs in tumor tissue compared to normal cells is the basis for the increased tumor specificity of liposomal drugs. Besides, solid tumors lack adequate lymphatic drainage and therefore there is low clearance of extravasated liposomes and tumor macromolecules, resulting in the accumulation of nanoparticles in the tumor microenvironment. Passive targeting may result in an increase in drug concentrations within solid tumors by several times compared to those obtained with free drugs[119,120].

4.1.2 LIGAND-TARGETED STEALTH LIPOSOMES

As previously mentioned, liposomes can be functionalized on their surface by introducing specific ligands for antigens and tumor receptors and therefore, capable of delivering the drug to the desired site of action (active targeting). In this way, it is possible to obtain targeted liposomes that increase the specificity of the interaction of liposomal drugs with the target cells and at the same time, reduce the off-target effects of the drugs. Targeting molecules may include antibody molecules or fragments, small molecules, peptides, carbohydrates, glycoproteins, or receptor ligands (Figure 16); in other words, any molecule capable of selectively recognizing and binding to over-expressed or expressed target antigens or receptors on cancer cells. An example of this strategy is the use of liposomes conjugated with folic acid. This exploits the high affinity for folate receptors (FRs) that are overexpressed in cancer cells[121].

A more common use concerns the conjugation of the liposomal surface with antibodies, immunoliposomes (IL). ILs are obtained by chemical conjugation of antibodies (or fragments) specific to a specific tumor antigen with the liposomal surface. Promising uses of IL include antiβ1 integrin-liposomes for metastatic lung cancer[122], anti-Her2 liposomes to target breast cancer cells[123], antiGD2 liposomes to target neuroblastoma, or melanoma[124,125], and anti-CD19 liposomes to target malignant B cells[126].

Several strategies allow the conjugation of proteins on the surface of liposomes. Two of the most used modalities are N-Hydroxysuccinimide (NHS)/ethyl (dimethylaminopropyl) carbodiimide (EDC) and maleimide crosslinkers. Both NHS/EDC and maleimide chemical reagents can be used in physiological conditions to avoid disturbing the tertiary and quaternary structure of antibodies to preserve targeting capabilities. NHS/EDC reactions activate carboxylates (-COOH) for conjugation to primary amines (-NH2) but these reactions are difficult to control in mAbs due to the presence of primary amines in antibodies. This lack of specificity is overcome by using specific crosslinkers such as maleimide (Figure 18).

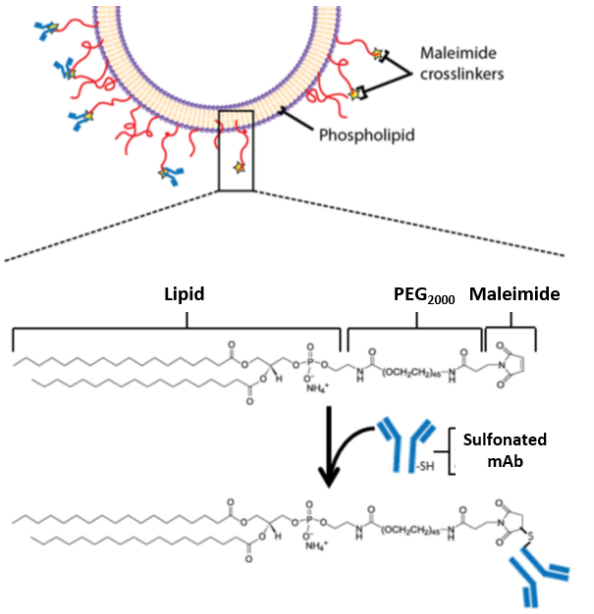

FIGURE 18. DSPE-PEG2000-Maleimide crosslinker location and reaction.

Maleimide reaction chemistry involves the specific reaction of maleimide with sulfhydryl groups (-SH). Sulfhydryl groups are located in the side chain of cysteine (Cys, C) amino acids which are often unavailable for crosslinking due to their activity in disulphide bonds (-S-S-). Hence, most cross-linking reactions first require a controlled thiolation reaction at primary amine sites using thiolation agents such as 2-iminothiolane. Traut's reagent (2-iminothiolane) is used to add sulfhydryl groups to the primary amines of lysine amino acids, found at the side chain.

4.1.3 METHODS OF PREPARATION

The most used method for the preparation of liposomal suspensions is named thin layer evaporation method (Figure 19), in which the lipid components are dissolved in an organic solvent, generally, a chloroform/methanol mixture is used. A hydrophobic drug to be encapsulated can be added to the lipid mixture (the drug, during the spontaneous formation of liposomes, intersperses between the phospholipids that make up the bilayer). The organic solvent is evaporated under vacuum, resulting in a dried lipid film. Subsequently, the lipid film is hydrated with aqueous solutions, generally buffer solutions at physiological pH, under continuous agitation at a temperature higher than the Tm (phase transition temperature; the definition in the next paragraph) of the phospholipid having the highest Tm value

(the hydrating solution can be added by a hydrophilic drug that is encapsulated in the aqueous core of the liposome).

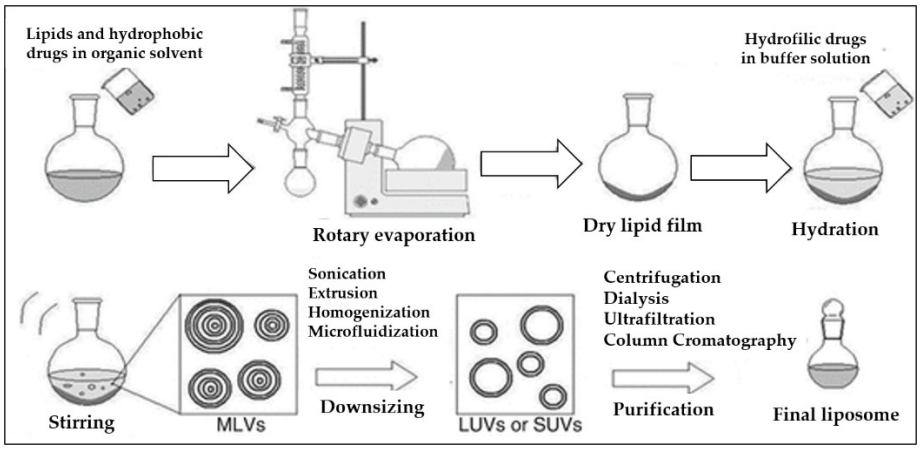

FIGURE 19. Thin layer evaporation technique passages: formation of the dry lipid film and hydration. After, downsizing and purification can be performed to obtain the final liposomal suspension.

Other methods of preparing liposomes include:

- Reverse phase evaporation: liposomes are formed by a water-in-oil emulsion of phospholipids and buffer, in excess of organic solvent.
- Lyophilization: liposomes are first cooled with the formation of ice crystals, then dried.
- Injection of ethanol: the lipids are dissolved in ethanol and rapidly injected into a buffer solution where they spontaneously form liposomes.

Techniques such as membrane extrusion, sonication, homogenization, and/or freeze-thaw are used to control the average size and size distribution and to obtain small or large single-lamellar vesicles (SUV or LUV, respectively) from multi-lamellar vesicles (MLV). Purification from remained materials after drug entrapment in liposomes can be performed using gel filtration chromatography, centrifugation, and dialysis.

4.1.4 POCKET-FORMING PHOSPHOLIPIDS

Physical features of liposomes depend largely on the nature of the lipids that make them up. Lipids, to form a bilayer, must be able to move freely near each other, and they must have the capacity to pack together to form a sphere.

A parameter that plays a key role in lipid movement and membrane flexibility is called "transition temperature, Tm", defined as the minimum temperature for lipids needed to induce a fluid-like state in which liposomes can self-assemble. This state is called the disordered liquid-crystalline state, in contrast to the ordered gel phase in which lipids are closely packed and lipid movement is limited[127]. This is important for both liposome formation and drug loading because the liquid-crystalline phase is required for liposome formation, but drug release is slower and more controlled in the ordered gel phase.

The most used lipids are phosphatidylcholine (zwitterionic), phosphatidylglycerol (negatively charged), phosphatidic acid, phosphatidylethanolamine (zwitterionic), and phosphatidylserine (negatively charged).

Dipalmitoyl-phosphatidylcholine (DPPC) is commonly used because is a lipid with a transition temperature (41°C) above that of the body's temperature (37°C) and thus DPPC liposomes would retain their loaded drugs during administration in humans or animals. In addition to temperature requirements, lipids must be chosen with volumetric properties that allow formation into small vesicles, as indicated by their packing parameter.

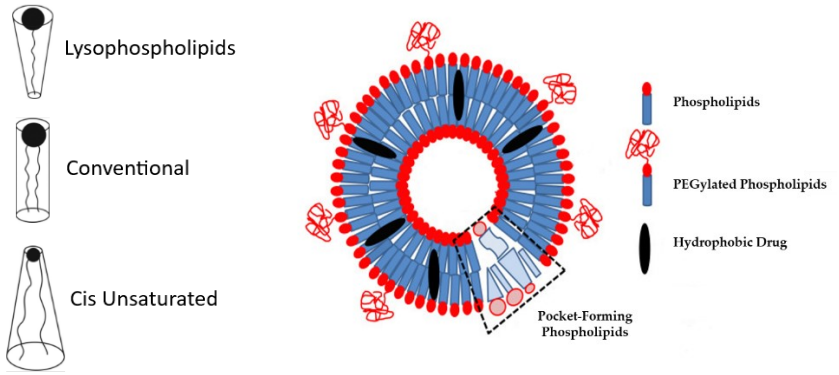

(a) **(b)**

FIGURE 20. Various types of phospholipids and their packing structure (a); Representation of cavities formed by pocket-forming lipids in a liposomal bilayer (b).

Phospholipids that possess *cis*-unsaturated fatty acid chains have an asymmetrical shape that increases the fluidity of the bilayer (Figure 20). The cis configuration forces the phospholipids to assume an angular structure of approximately 30°. Their asymmetrical shape forms cavities in the liposomal bilayer, creating "pockets" in which hydrophobic molecules can be accommodated (Figure 19). For this reason, these lipids are often used in liposomal formulations for their ability to increase the encapsulation of hydrophobic drugs[128,129]. POPC (1-palmitoyl-2-oleoyl-sn-glycero-3-phosphocholine) represents an example of cis-unsaturated phospholipid used in the liposomal formulation.

Another strategic component used in liposome formulations is represented by cholesterol. It has a modulatory effect on the properties of the lipid bilayer of the liposomes. It can increase the packing between the phospholipid molecules, resulting in more ordered conformation in the aliphatic tail region, controlling the stoutness in the liposome structure. Cholesterol is also crucial for the structural stability of liposomal membranes against environmental stress.

4.2 GOLD NANOPARTICLES

Among the different types of nanomaterials, metal nanoparticles, especially gold nanoparticles (AuNPs), have shown strong interest in the different fields of science, due to their special features: high X-ray absorption coefficient, easy synthesis manipulation, precise control of the physicochemical properties of the particle, strong binding affinity with thiols, disulphides, and amines[130].

The anisotropy of these non-spherical, hollow, and nanoshell AuNP structures is the source of plasmon absorption in the visible region as well as in the near-infrared (NIR) region, which is especially sensitive to the AuNP shape. This property has given rise to medical applications such as diagnostics and therapy[131].

Explicit physical and chemical properties make AuNPs prodigious scaffolds for various applications in therapeutics, detection and diagnostics, drug delivery[132] and imaging[133]. Also, other features of AuNPs include large surface-to-volume ratio, excellent biocompatibility, and low toxicity. In aqueous solution, AuNPs appear in a range of colors (orange, red to purple) as there is a growth of the core size from 1 to 100 nm with the exposure of the size relative absorption peak from 500 to 550 nm[134].

Generally, procedures for the synthesis of AuNPs can be arranged into physical, chemical, and biological methods.

Methods such as the γ-irradiation method, ultraviolet (UV) radiation, microwave (MW) irradiation, laser ablation, thermolytic process, and photochemical process are categorized as physical procedures[135]. The γ-irradiation method renders controllable size and high purity of nanoparticles with a diameter of 5–40 nm. In the microwave irradiation method, heating or photochemical reduction method was utilized to form AuNPs[136].

In chemical methods, chemical reactions are performed in an aqueous medium by a reduction agent. Citrate and sodium borohydride are the common reducing agents used. Among the conventional methods of chemical synthesis of colloidal gold, the Turkevich procedure is highly utilized due to the simplicity and ease of

synthesis, controllable size, and stability of colloidal nanoparticles[137]. In the standardized procedure, sodium citrate reduced and stabilized the solution. It provides spherical AuNPs with a narrow size distribution.

Biological synthesis is another route of synthesis. Reducing hazardous generated wastes and assisting "green chemistry" are the main objectives of biosynthesis. Plant-based compounds and derivatives, bacteria, fungi, algae, yeast, and viruses are employed as the common resources[137].

Gold nanoparticles of various shapes and sizes find different fields of application such as:

- Photodynamic therapy: Effective fluorescence quenching and surface plasmon resonance (SPR) absorption are the significant features of AuNPs that have been utilized in photodynamic therapy.
- Photothermal therapy (PTT) known as thermal ablation is a highly applied method in cancer therapy with minimal invasiveness. AuNPs with maximum absorption in the visible or near IR region, receive light and generate heat. The heat causes the death of malignant tumors[138].
- AuNPs have attracted the main attention as an x-ray contrast agent because it represents a high X-ray absorption coefficient, ease of synthetic manipulation, nontoxicity, surface functionalization for colloidal stability and targeted delivery.
- Considerable features of AuNPs make them an efficient nanocarrier in drug delivery systems. These effective nanocarriers are capable of transferring various drugs such as peptides, proteins, and chemotherapeutic agents[139]. Verigene (FDA-approved) and Aurimmune (Phase-II) are gold-based nanomaterials for the application of therapeutics[140].

SECTION 1

PRECLINICAL CHARACTERIZATION OF SI306-LOADED LIPOSOMES AND ANTIGD2-DECORATED IMMUNOLIPOSOMES FOR THE TREATMENT OF NEUROBLASTOMA

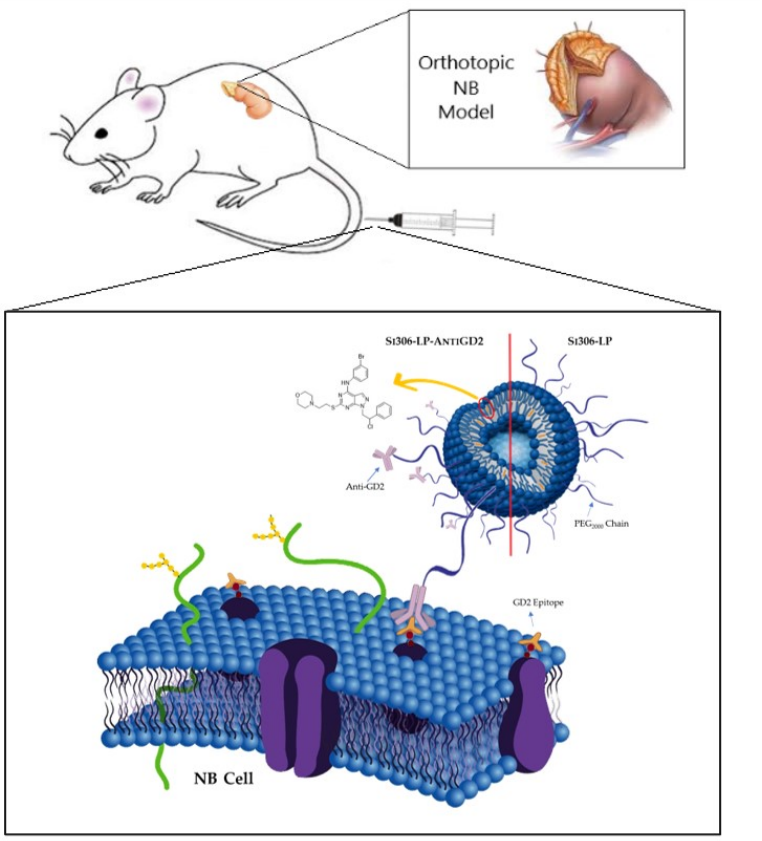

STATE OF ART: SI306 AGAINST NB

Several members of the pyrazolo[3,4-*d*]pyrimidine family showed cytotoxic activity against human NB cell lines. The compound that showed promising anticancer activity is the compound Si306. Its activity was evaluated on SH-SY5Y NB cell line showing an IC_{50} value of 2.28 μM after 72 h of incubation[141]. Moreover, the compound Si306 was shown to be safe, exhibiting a value greater than 100 μM on Wi38 cells (normal embryonic fibroblast cell line), and having a cytotoxic effect only on cancer cells. Also, the action of Si306 on the cell cycle was evaluated; this showed a significant and dose-dependent accumulation of cells in the G1 phase of the cell cycle starting from 0.1 μM. In parallel, a progressive accumulation of hypodiploid cells was observed, indicating the presence of apoptotic cells[45].

Finally, *in vivo* studies using subcutaneous NB-xenografted mice models with NB SH-SY5Y cells. Mice treated daily orally with a dosage of 50 mg/kg, showed a reduction of more than 50% in the mean tumor volume compared to control. In addition, a significant anti-angiogenic effect was observed (Figure 21a), further demonstrated by a three-dimensional *in vitro* sprouting test on endothelial cells (Figure 21b)[45].

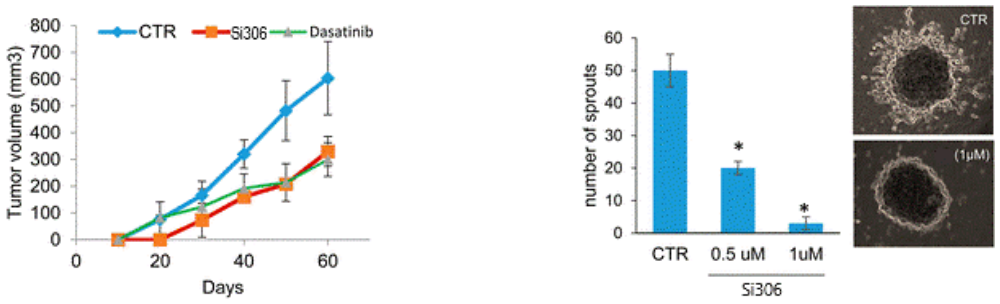

(a) **(b)**

FIGURE 21. Evaluation of the antitumoral effect of Si306 and dasatinib (reference compound) (a); anti-angiogenic effect of Si306 by sprouting assay with endothelial cells (b).

Considering the problems in terms of aqueous solubility of the compound Si306, preliminary studies of liposomal formulations have been conducted[141]. The compound Si306 encapsulated in stealth liposomes resulting in homogeneous size distribution and optimal ζ-potential value. Cytotoxicity studies on the SH-SY5Y cell

line do not show a loss of activity compared to the free compound. Furthermore, preliminary *in vivo* studies on healthy rats treated intraperitoneally at a dosage of 50 mg/kg of Si306 loaded in liposomes showed an increase in the concentration after 24 h compared to the free drug in all the organs analyzed (Figure 22).

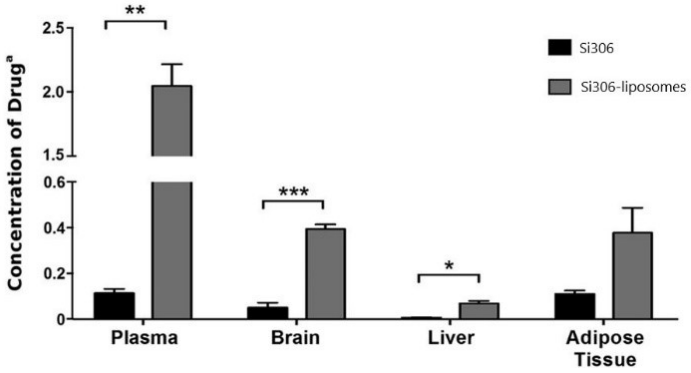

FIGURE 22. Concentration of compound Si306 determined 24 h after intraperitoneal administration in healthy rats of the free drug (black bars) and Si306-liposomes (grey bars) at a dosage of 50 mg/kg.

AIM OF THE PROJECT

In this project, the compound Si306 a pyrazolo[3,4-*d*]pyrimidine derivative, given its promising anti-tumor activity on NB, has been selected to develop liposomal formulations for its *in vivo* delivery and thus to overcome its solubility problems that could be limiting its development. More specifically, long-circulation stealth liposomes and liposomes decorated with the antiGD2 monoclonal antibody (immunoliposomes) both loaded with Si306, were developed and fully characterized in terms of morphology, stability, and physio-chemical properties. Moreover, considerable efforts were required to ensure a reproducible and reliable product before using these formulations for *in vitro* and *in vivo* biological testing.

The assumption of this work is to improve the solubility enhancing the PK properties of Si306 through its encapsulation in (1) sterically stabilized liposomes that allow a slower elimination of the drug from the systemic circulation and an improvement of its release into the tumor area, thanks to the ERP effect, and (2) liposomes conjugated with the antiGD2 monoclonal antibody which allows obtaining an active-targeted delivery system by exploiting the expression of GD2 antigen on the surface of NB cells.

RESULTS

1. WESTERN BLOT ON IMR-32-A-LUC CELL LINE

To confirm the overexpression/hyperactivation of c-Src (target of Si306) in the NB cell lines, a representative western blot analysis of phospho-c-Src and total c-Src in IMR-32-A-Luc cell line treated with Si306 at 1 and 10 μM was performed.

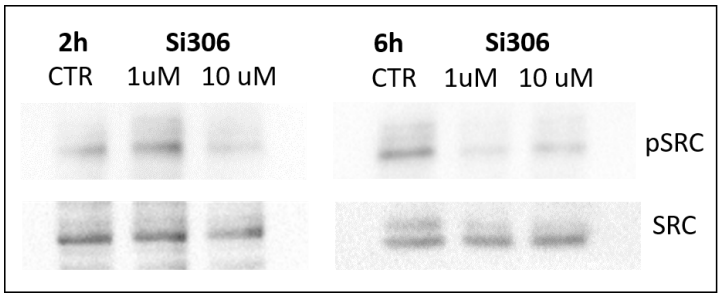

FIGURE 23. Determination of the c-Src and phospho-c-Src expression in IMR-32-A-Luc cell line after treatment with Si306 at 1 and 10 μM after 2 and 6 hours measured by Western blot analysis.

As shown in Figure 23, a pronounced concentration- and time-dependent inhibition of phospho-c-Src was observed after Si306 treatment. This result confirms the presence of c-Src in the cell line chosen for further *in vivo* studies in NB mice models.

2. Si306-loaded Stealth Liposomes: Preparation and Characterization

Si306-loaded stealth liposomes (Si306-LP) have been prepared as described in the materials and methods section, paragraph 2. Si306-LP have been characterized in terms of mean diameter, ζ-potential, and polydispersity index (PDI) through the use of Dynamic Light Scattering (DLS). The size and ζ-potential values were 126 nm and -22.6 mV, respectively. The amount of phospholipids (PLs), determined as a function of cholesterol levels detected, was 9.06 and 31.68 μmol/mL for the final Si306 dosage formulations of 5 and 25 mg of Si306/Kg, respectively, and showed a drug encapsulation efficiency percentage (EE%) equal to 76.91% and 86.23%, respectively. Results are summarized in Table 2.

Table 2. Properties of Si306-LP.

Parameters	Si306-LP
Amount of PLs (μmol/mL)[a]	
5 mg of Si306/kg	9.06 ± 0.65
25 mg of Si306/kg	31.68 ± 7.01
EE%[a]	
5 mg of Si306/kg	76.91 ± 3.19
25 mg of Si306/kg	86.23 ± 3.29
Size (nm)[b]	126 ± 15
ζ-potentials (mV)[b]	-22.6 ± 3.5
PDI[b]	0.121 ± 0.015
Thickness bilayer (nm)[c]	7.02 ± 1.79

[a]Amount of PLs in the liposomal suspension at the dosage of Si306 used for the in vivo experiments was measured by UV/LC-MS; [b]measured by DLS (Dynamic Light Scattering); [c]measured by analysis of cryo-TEM images by Image J Software. For all measurements the mean value ± S.D. is reported.

The morphology and particle size were also evaluated using Cryo Transmission Electron Microscopy (Cryo-TEM). As shown in Figure 24, the Cryo-TEM analysis

confirmed the presence of a homogeneous and unilamellar population of liposomal nanoparticles with particle sizes ranging from 90 to 120 nm. The average thickness of the phospholipidic bilayer was 7.02 nm (measured by Image J software).

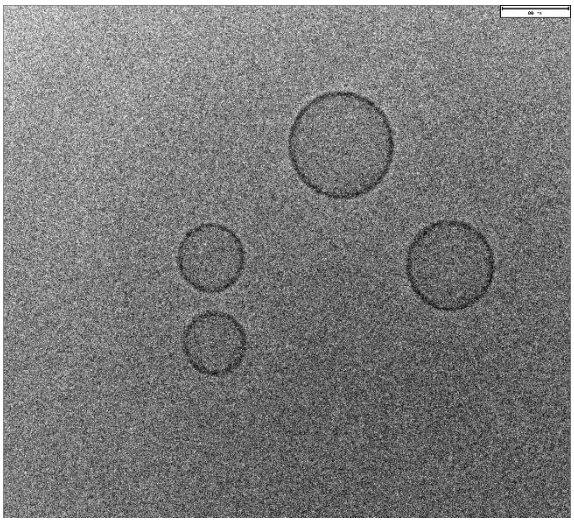

FIGURE 24. Image of Si306-LP obtained by Cryo-TEM analysis.

3. ANTIGD2-DECORATED IMMUNOLIPOSOMES: PREPARATION AND CHARACTERIZATION

AntiGD2-decorated stealth liposomes (Si306-iLP) have been prepared as described in the materials and methods section, paragraph 3. In the same manner as Si306-LP, Si306-iLP have been characterized in terms of mean diameter, ζ-potential, and PDI through the use of DLS showing values of 133 nm, -19.3 mV, and 0.120, respectively. EE% values of 56.39% and 77.33% were estimated for the liposomal suspensions at final Si306 dosages of 5 and 25 mg/kg, respectively, while the quantity of PLs was 10.80 and 20.98 μmol/mL at the final dosages of 5 and 25 mg of Si306/Kg, respectively. Results are shown in Table 3.

TABLE 3. Properties of Si306-iLP.

Parameters	Si306-iLP
Amount of PLs (μmol/mL)[a]	
5 mg of Si306/Kg	10.80 ± 1.84
25 mg of Si306/Kg	20.98 ± 2.94
EE%[a]	
5 mg of Si306/Kg	56.39 ± 3.75
25 mg of Si306/Kg	77.33 ± 4.34
Size (nm)[b]	133 ± 16,4
ζ-potentials (mV)[b]	-19.3 ± 1.56
PDI[b]	0.120 ± 0.003
Thickness bilayer (nm)[c]	7.21 ± 1.13

[a] Amount of PLs in the liposomal suspension at the dosage of Si306 used for the in vivo experiments was measured by UV/LC-MS; [b]measured by DLS (Dynamic Light Scattering); [c]measured by analysis of cryo-TEM images by Image J Software; For all measurements the mean value ± S.D. is reported.

Cryo Transmission Electron Microscopy (Cryo-TEM) has been performed to evaluate the morphology and particle size. As shown in Figure 25, the Cryo-TEM analysis also for AntiGD2-decorated liposomes confirmed the presence of a

unilamellar particle (SUV) with particle sizes ranging from 80 to 130 nm. The average thickness of the phospholipidic bilayer was 7.21 nm (measured by Image J software). Moreover, surface roughness has been noted, which is evidence of the presence of antibodies on their surface.

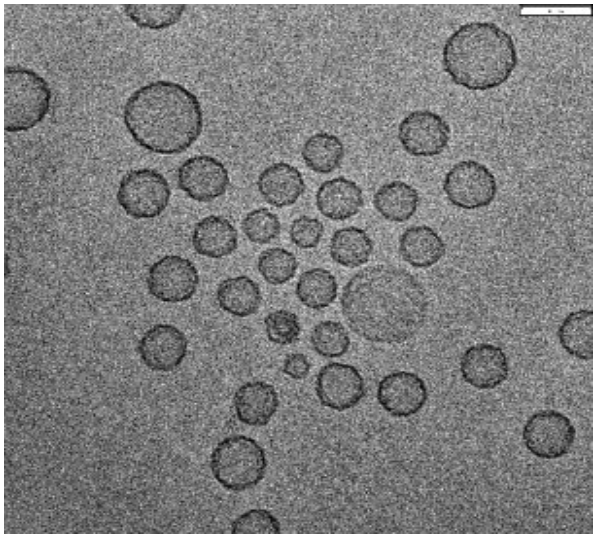

FIGURE 25. Image of Si306-iLP obtained by Cryo-TEM analysis.

Confirmation of the presence of the conjugated antibody on the liposomal surface was obtained by colorimetric protein quantification assay (BCA assay, see materials and methods section, paragraph 4.4.2). As shown in Table 4, for both immunoliposome formulations, the levels of coupled-AntiGD2 were estimated in a range of 8-14 μg/μmol of PLs (25-27 μg/200 μL of injected volume per mouse for *in vivo* experiments).

TABLE 4. Quantification of antiGD2 conjugated on Si306-iLP nanoparticles.

Si306-iLP	**BCA Assay**	
Dosages	μg mAb/μmol PLs	μg mAb/200μL injected
5 mg/kg	14.44 ± 4.64	25.71 ± 5.63
25 mg/kg	8.03 ± 1.39	27.30 ± 4.34

AntiGD2 quantified spectroscopically using BCA assay protein quantification kit, mean value ± S.D.

4. STABILITY STUDIES AND *IN VITRO* RELEASE

To determine whether Si306-LP and Si306-iLP were stable, liposomal suspensions were stored at 4°C over a period of 2 weeks and sampled periodically to measure mean particle size, ζ-potential and PDI. The stability test for both Si306-LP and Si306-iLP are summarized in Table 5. A slight change of 26 and 11 nm in mean diameter was observed for Si306-LP and Si306-iLP respectively, during the period of storage. Also, PDI increased from 0.121 to 0.300 for Si306-LP and 0.120 to 0.212 for Si306-iLP in 14 days.

TABLE 5. Stability of Si306-LP and Si306-iLP over a period of 14 days.

Parameters	Day 0	Day 3	Day 7	Day 14
		Si306-LP		
Size (nm)[a]	126 ± 15	126 ± 4	148.3 ± 11	152 ± 13
PDI[a]	0.121 ± 0.015	0.122 ± 0.011	0.176 ± 0.032	0.300 ± 0.012
ζ-potential (mV)[a]	-22.6 ± 3.48	-22.9 ± 3.12	-26.1 ± 3.15	-23.1 ± 2.6
		Si306-iLP		
Size (nm)[a]	133 ± 16,4	134 ± 14	137 ± 12.7	144 ± 15.1
PDI[a]	0.120 ± 0.003	0.121 ± 0.009	0.151 ± 0.012	0.212 ± 0.019
ζ-potential (mV [a]	-19.3 ± 1.56	- 18.7 ± 1.34	- 19.7 ± 1.66	- 20.1 ± 1.46

[a]Measured by DLS (Dynamic Light Scattering).

Furthermore, both liposomal formulations showed minimal drug leakage, estimated using the dialysis bag method, over a period of 96 h (Figure 26). Liposomes have proved to retain >95% of the encapsulated compound after the incubation period.

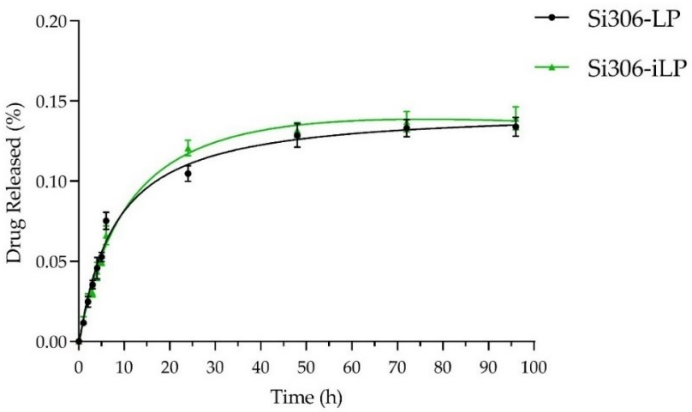

FIGURE 26. *In vitro* release of Si306-loaded liposomes (black curve) and immunoliposomes (green curve).

5. *IN VITRO* CYTOTOXICITY STUDIES

Si306 in DMSO solution, Si306-LP and Si306-iLP were evaluated for their cytotoxicity against human NB cell lines (IMR-32-A-Luc, HTLA-230, and SH-SY5Y) and human fibroblasts. Dose-dependent growth inhibition of cells by Si306-LP and Si306-iLP or free Si306 was performed treating cells with different concentration (0.1, 1, 10, and 100 μM) of each sample for 1, 6, and 24 h respectively, followed by washing (at the end of each treatment time) and further incubation for 96 h. MTT assay was assessed at the end of incubation and the cytotoxicity of Si306, either free or encapsulated in Si306-LP and Si306-iLP, was compared as a function of time.

TABLE 6. Cytotoxicity of various formulations of Si306 against GD2-positive (IMR-32-A-Luc HTLA-230, and SH-SY5Y) and GD2-negative (Fibroblasts) cell lines.

Cell Lines	IC_{50} (μM) ± S.D.[a]		
	Si306 in DMSO	**Si306-LP**	**Si306-iLP**
IMR-32-A-Luc			
1h	40.9 ± 3.3	28.7 ± 1.2	27.2 ± 1.5
6h	21.6 ± 2.2	30.5 ± 2.3	27.4 ± 1.1
24h	5.9 ± 1.4	3.3 ± 0.5	2.3 ± 0.6
HTLA-230			
1h	55.1 ± 4.3	36.8 ± 5.2	20.3 ± 8.7
6h	28.1 ± 2.7	4.4 ± 0.9	3.2 ± 1.1
24h	2.9 ± 0.3	0.6 ± 0.1	0.5 ± 0.1
SH-SY5Y			
1h	31.2 ± 2.4	47.5 ± 3.4	29.2 ± 1.5
6h	23.7 ± 2.6	46.7 ± 5.3	27.2 ± 1.7
24h	19.6 ± 0.7	34.5 ± 1.3	16.8 ± 0.2
Fibroblasts			
1h	157.9 ± 6.1	170.8 ± 5.2	125.0 ± 3.4
6h	94.1 ± 7.3	127.4 ± 3.1	111.7 ± 4.7
24h	26.6 ± 2.7	64.9 ± 2.7	46.4 ± 1.5

[a] IC_{50} was evaluated as dose-response inhibition of MTT assay. Data are means ± S.D. of three independent experiments each done in triplicate.

As summarized in Table 6, the IC_{50} has almost always decreased as the exposure of cells to the drug increased from 1 h to 24 h. After 24 h of incubation Si306-iLP were 2-fold more cytotoxic than free drug against IMR-32-A-Luc and SH-SY5Y cell lines and almost 6-fold more cytotoxic on HTLA-230 cells. While comparing the IC_{50}

values (after 24 hours) of Si306-iLP with Si306-LP, it can be seen that both liposomal formulations showed comparable IC_{50} values against the IMR-32-A-Luc and HTLA-230 cell lines. In contrast, AntiGD2-decorated immunoliposomes showed 2-fold more cytotoxicity than naked liposomes against the SH-SY5Y cell line. Overall, both liposomal formulations lead to higher cytotoxic activity than Si306 dissolved in DMSO on all NB cell lines, except for Si306-LP on the SH-SY5Y cell line.

Finally, both liposomal formulations proved to be safer than the free drug, showing IC_{50} values against fibroblasts ≈2-fold more than free Si306.

6. Cellular Association and Uptake of Si306-loaded Liposomes

The levels of cellular association of Si306-iLP or non-targeted liposomes (Si306-LP) were evaluated by Flow Cytometry (FACS). 0.1 mol% of PE-CF (1,2-dioleoyl-sn-glycero-3-phosphoethanolamine-N-(carboxyfluorescein) ammonium salt), a fluorescent lipid, was added during the lipid thin layer preparation. The evaluation was conducted on GD2-positive and GD2-negative cell lines summarized in Table 7.

Table 7. GD2 antigen expression in NB cell lines[142].

Cell line	GD2 Expression
HTLA-230 IMR-32 IMR-32-A-Luc	High
SK-N-AS	Medium
SH-SY5Y SK-N-SH NB-1	Low
NK	GD2-negative
B-16	Control

Each aliquot of cells was incubated for 1 h at 4°C or 37°C with different formulations (Si306-LP and Si306-iLP, 400 nmol of phospholipid/mL). Then, cells were washed subsequently with PBS and the binding (4°C) or both binding and cellular uptake (37°C) were evaluated. As show in Figure 27, the cellular association after incubation at 4°C reporting how the level of cellular binding of liposomes is

dependent on GD2 expression in the different cell lines. Si306-iLP showed a 2-5 times higher cell association to all the GD2-positive cell lines compared to non-targeted liposomes (Si306-LP). In contrast, GD2-negative cell lines showed low levels of liposomes associated with cells for both targeted and non-targeted liposomes. These results confirm the ability of mAb to bind to the antigen and produce cellular internalization of liposomal particles.

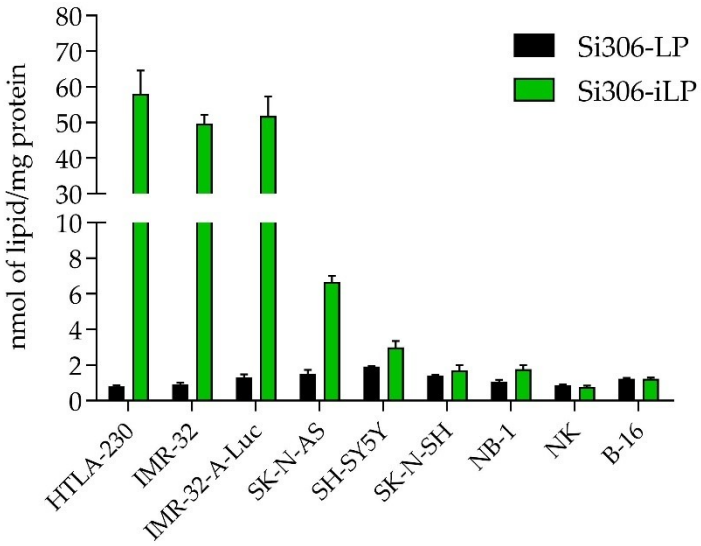

FIGURE 27. Binding evaluation at 4°C of Si306-LP (black bars) and Si306-iLP (grey bars) on GD2-positive cell lines (HTLA-230, IMR-32-A-Luc, SK-N-AS, SH-SY5Y, SK-N-SH, and NB-1), GD2-negative (NK), and control cell line (B-16). Liposomes were incubated with 1×10^6 cells at 400 nmol phospholipid/mL.

Table 8 showed an illustrative example of the cellular association at 4°C and 37°C using IMR-32-A-Luc as GD2-expressive, SH-SY5Y as GD2-low expressive, and NK cell line as GD2-negative cells.

TABLE 8. Cellular association of Si306-LP and Si306-iLP with GD2-positive and negative cell lines.

Cell lines	Binding (4°C)		Uptake (37°C)	
	Si306-LP	Si306-iLP	Si306-LP	Si306-iLP
IMR-32-A-Luc	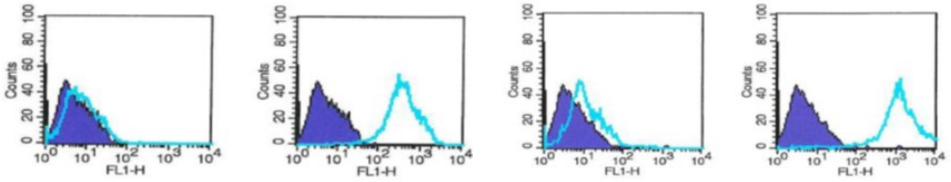			
SH-SY5Y	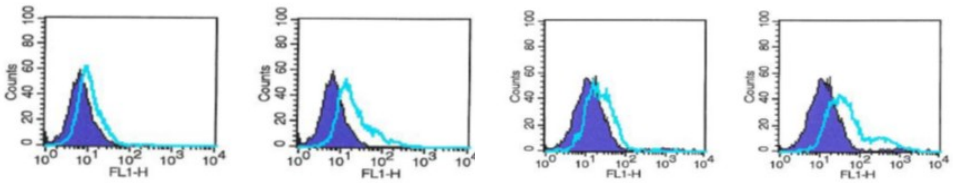			
NK (GD2-neg)	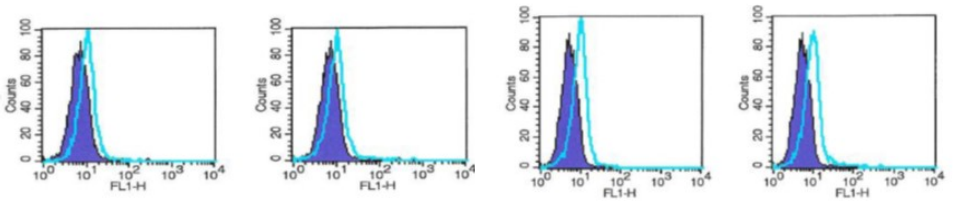			

Cellular association of liposomal formulations evaluated after incubation with cells for 1 h at 4°C and 1 h at 37°C with Si306-LP and Si306-iLP respectively, followed by washing. The cells were enumerated by FACS. Purple area: cells only, blue line: liposomes with cells.

7. PHARMACOKINETIC STUDIES

PK and biodistribution (BD) studies were performed to evaluate the *in vivo* profile of Si306 dissolved in citric acid solution in presence of Tween80 and benzyl alcohol as co-solvents, and both Si306 liposomal formulations (Si306-LP and Si306-iLP) to prove the development of a long circulation drug delivery system for Si306. Experiments were conducted on BALB/c healthy male mice by intravenous (i.v.) injection of two dosages of Si306 at a single dose of 5 and 25 mg/kg (for experimental methodology, see Materials and Methods section, paragraph 6). After treatment, at prefixed time points, mice were sacrificed and blood, lungs, kidneys, liver, and spleen were collected and the concentration of Si306 was determined. LC-MS/MS analysis was performed to the quantification of Si306 administered at the dosage of 5 mg/kg while, UV/LC-MS analysis was used for the quantification of Si306 injected at the dosage of 25 mg/kg.

7.1 DOSAGE OF 5 mg/kg IN HEALTHY MICE

Plasma concentration-time curves of Si306-Tween80 and both liposomal formulations at the dosage of 5 mg/kg are shown in Figure 28 and corresponding PK parameters are presented in Table 9. Organ biodistributions are shown in Figure 28. As can be observed from the plasma concentration-time curves, both liposomal formulations have shown higher concentrations than Si306-Tween80 which results in long circulation of the drug delivered by liposomes and slower elimination from the bloodstream in a time-dependent manner, until Si306 is eliminated from blood at 48 h. Si306 encapsulated in liposomes showed higher C_{max} values (5.42 and 4.73 μg/mL for Si306-LP and Si306-iLP, respectively) than the free drug (3.42 μg/mL). Both Si306-LP and Si306-iLP showed values of $AUC_{0\rightarrow 48h}$ twice higher than Si306-Tween80 and the same is also true for the MRT parameter where Si306-LP showed MRT value 2-fold higher while Si306-iLP is slightly higher than the free drug. Also, plasma clearance values confirm the slower elimination of the drug from the circulatory stream when it is delivered by liposomes.

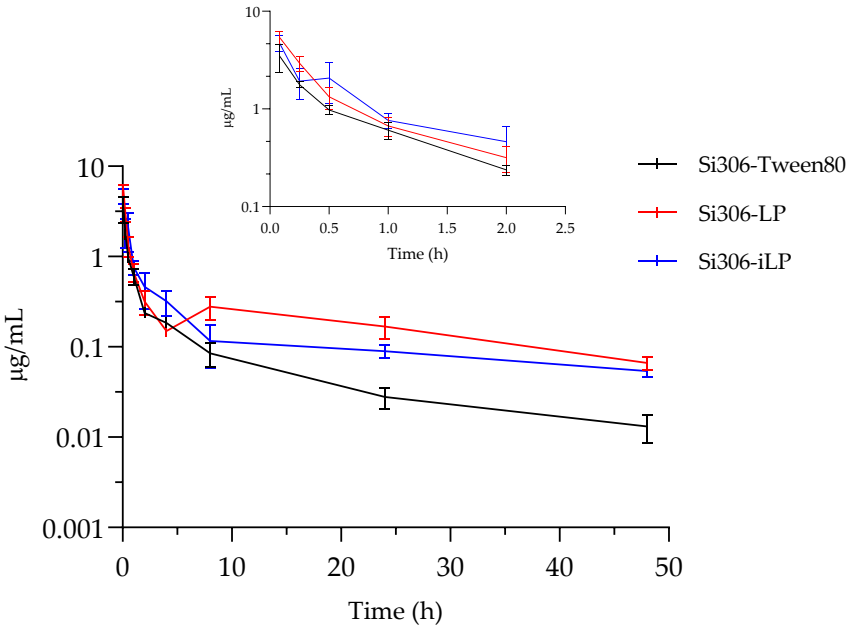

FIGURE 28. Plasma concentration-time curves (mean ± S.E.M., n=5) after i.v. administration of a single dose of Si306-Tween80 (black curve), Si306-LP (red curve) and Si306-iLP (blue curve) at the dosage of 5 mg/kg. The plasma concentration in the y-axis is expressed as $\log_{10}$ scale.

TABLE 9. Plasma PK parameters[a] of free Si306, Si306-LP and Si306-iLP evaluated after injection of a single dose of 5 mg/kg.

Parameter	Unit	Plasma		
		Si306-Tween80	Si306-LP	Si306-iLP
Dose	mg/kg	5	5	5
$t_{1/2}$[b]	h	15.31	17.10	15.74
T_{max}[c]	h	0.08	0.08	0.08
C_{max}[d]	µg/mL	3.42	5.42	4.73
$AUC_{0\rightarrow 48h}$[e]	µg/mL×h	4.30	10.35	8.34
$AUC_{0\rightarrow \infty}$[e]	µg/mL×h	4.59	11.73	9.05
$MRT_{0\rightarrow \infty}$[f]	h	11.29	20.43	14.76
V_z[g]	L/Kg	120.36	52.57	12.54
CL[h]	L/h/Kg	5.45	2.13	0.55

[a]Calculated with PKSolver; [b]$t_{1/2}$: half-life. [c]T_{max}: time of maximum concentration observed. [d]C_{max}: maximum concentration observed. [e]AUC: area under the curve. [f]MRT: mean residence time [g]V: volume of distribution. [h]CL: clearance. PK data were evaluated using a non-compartment model.

In all tissues analyzed, an immediate distribution followed by a concentration decrease in a time-dependent manner was observed (Figure 29a, b and c). Si306-LP showed the highest concentration of Si306 in the lungs (68.61 µg/g after 4 h)

compared to Si306 free and Si306 encapsulated in liposome-AntiGD2 where the highest tissue concentration was observed after 4 h (6.48 μg/g) and 15 minutes (39.40 μg/g), respectively. In contrast, Si306-iLP showed high drug concentration in the liver after 15 minutes (17.49 μg/g) compared to Si306-LP (4.94 μg/g after 5 minutes) and the free drug (4.69 μg/g after 5 minutes). In splenic tissue, however, the maximum concentration of Si306 in free form was observed after 5 minutes (4.43 μg/g) while after 4 h comparable tissue concentrations for both liposomal formulations were observed.

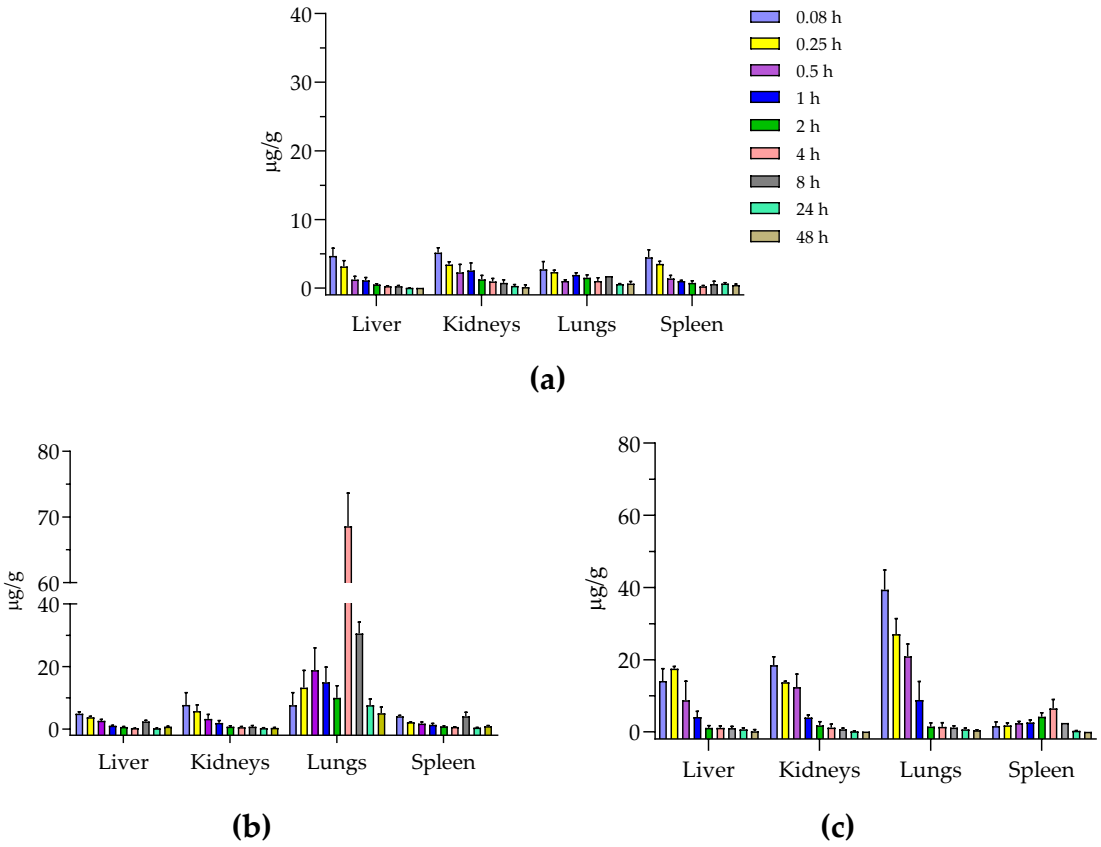

FIGURE 29. Biodistribution of **(a)** Si306-Tween80, **(b)** Si306-LP and **(c)** Si306-iLP at the dosage 5 mg/kg over 48 h (mean ± S.E.M., n=5) for the analyzed organs: liver, kidneys, lungs, and spleen.

As shown in Table 10, both liposomal formulations showed higher values of $AUC_{0\rightarrow 48h}$ than Si306 administered in free form in liver, lungs, and spleen while comparable values of $AUC_{0\rightarrow 48h}$ in kidneys were obtained. In lungs, Si306-LP showed an $AUC_{0\rightarrow 48h}$ value more than 10-fold higher than Si306 delivered by

immunoliposomes while comparable $AUC_{0\rightarrow 48h}$ values for other tissues were obtained.

TABLE 10. $AUC_{0\rightarrow 48h}$ of liver, spleen, lungs, and kidneys after i.v. administration of Si306 formulated as Tween80 solution and both liposomal formulation at a single dose of 5 mg/kg.

	$AUC_{0\rightarrow 48h}$[a] (μg/mL×h)		
Tissue	**Si306-Tween80**	**Si306-LP**	**Si306-iLP**
Liver	8.05	43.04	44.48
Spleen	29.28	67.04	60.43
Lungs	45.16	762.41	64.79
Kidneys	24.60	26.43	31.01

[a]*Area Under the Curve evaluated using a non-compartment model (PKSolver Software).*

This trend can be explained by the fact that splenic and hepatic tissue (RES-rich organs) are the site of action of the mononuclear phagocyte system[143]. The large distribution in lungs is explained by the ability of the drug delivered by liposomes to quickly reach lung tissue after intravenous administration and several studies explain the affinity between liposomes and lung tissue[144,145]. This might seem a potential disadvantage of this drug delivery system in terms of lung toxicity, but it has been seen that negatively charged liposomes showed no toxicity unlike cationic liposomes causing inflammation and inducing lung cells to produce ROI (reactive oxygen intermediates)[146,147].

7.1.1 MATRIX EFFECT, RECOVERY AND PROCESS EFFICIENCY EVALUATION

The matrix effect (%ME) during validation of analytical methods in biological samples can best be examined by comparing the MS/MS response (peak areas) of Si306 at a given concentration spiked post-extraction into plasma or tissue extract (**B**, Eq. 1), with the MS/MS response (**A**, Eq. 1) of the same analyte in the "neat" mobile phase (for more details see Paragraph 6.2 -Materials and Methods section). The matrix effect values, evaluated using the ESI interface in plasma and tissue extracts and calculated according to Eq. 1, are summarised in Table 11. A value of 100% indicates that the response in the mobile phase and in the plasma/tissue extracts were the same and no absolute matrix effect was observed. A value of >100% indicates an ionization enhancement and a value of <100% indicates ionization suppression.

Besides, recovery (%RE) is determined using Eq. 2 as the ratio of mean peak areas of Si306 spiked *before* extraction (**C**) and mean peak areas of Si306 spiked *after* extraction into plasma/organ extracts (**B**) (for more details see Paragraph 6.2 - Materials and Methods section). In this way, "true" recovery values that are not affected by the matrix has been obtained.

TABLE 11. Matrix Effect and Recovery of Si306 in mice plasma, liver, kidneys, spleen, and lungs.

µg/mL of Si306	Matrix Effect (%)					Recovery (%)				
	Plasma	Liver	Kidneys	Spleen	Lungs	Plasma	Liver	Kidneys	Spleen	Lungs
0.1	62.77	-	-	-	-	109.73	-	-	-	-
1	73.75	112.03	132.08	131.62	117.84	106.50	115.61	99.06	99.48	109.25
5	-	-	-	-	-	-	-	-	-	-
10	83.62	133.89	130.83	132.18	104.99	104.76	95.49	104.12	93.19	111.80
50	94.99	-	-	-	-	100.42	-	-	-	-
100	-	135.99	135.50	106.09	118.69	-	97.12	97.05	86.27	91.18

%ME data suggest a moderate ionization enhancement for Si306 in all tissues while a very small ionization suppression for Si306 in plasma samples was observed. Ultimately, %ME and %RE data suggest that the developed LC-MS/MS analysis

method can be successfully applied to the PK and BD studies for the determination of Si306 in biological plasma and tissues. Furthermore, from the evaluation of %ME and %RE it is possible to calculate the process efficiency (Table 12) which expresses the trueness of the LC-MS/MS instrument applying Eq. 3 (see Paragraph 6.2 - Materials and Methods section).

TABLE 12. Process Efficiency of LC-MS/MS using ESI interface.

μg/mL of Si306	Process Efficiency (%)				
	Plasma	Liver	Kidneys	Spleen	Lungs
0.1	68.88	-	-	-	-
1	78.55	129.52	130.84	130.93	128.75
10	87.60	127.85	136.22	123.18	117.39
50	95.30	-	-	-	-
100	-	132.06	131.51	91.53	108.22

7.2 DOSAGE OF 25 mg/kg IN HEALTHY MICE

Regarding the plasma concentration-time curves and PK parameters of Si306-Tween80 and liposomal formulations at the dosage of 25 mg/kg, as shown in Figure 30 and Table 13, a similar trend to that obtained for the 5 mg/kg dosage was observed with higher plasma levels of Si306 and slower elimination from the bloodstream in a time-dependent manner when it is delivered by stealth liposomes compared to liposomes conjugated with AntiGD2 antibody. Si306 encapsulated in immunoliposomes showed higher C_{max} values (37.80 μg/mL) than the free drug and stealth liposomes (25.45 and 14.43 μg/mL, respectively). Both Si306-LP and Si306-iLP showed values of $AUC_{0\rightarrow 48h}$ higher than Si306-Tween80. Si306 delivered by stealth liposomes showed an $AUC_{0\rightarrow 48h}$ value almost 4- and 3-fold higher than Si306 free and Si306-iLP. In contrast, MRT of values 2- and 7-fold higher were observed for Si306-iLP compared to Si306-LP and Si306-Tween80, respectively. In addition, as previously observed at a dosage of 5 mg/kg, the slow elimination of the drug from the circulatory stream when it is administered by liposomes has been confirmed by plasma clearance values.

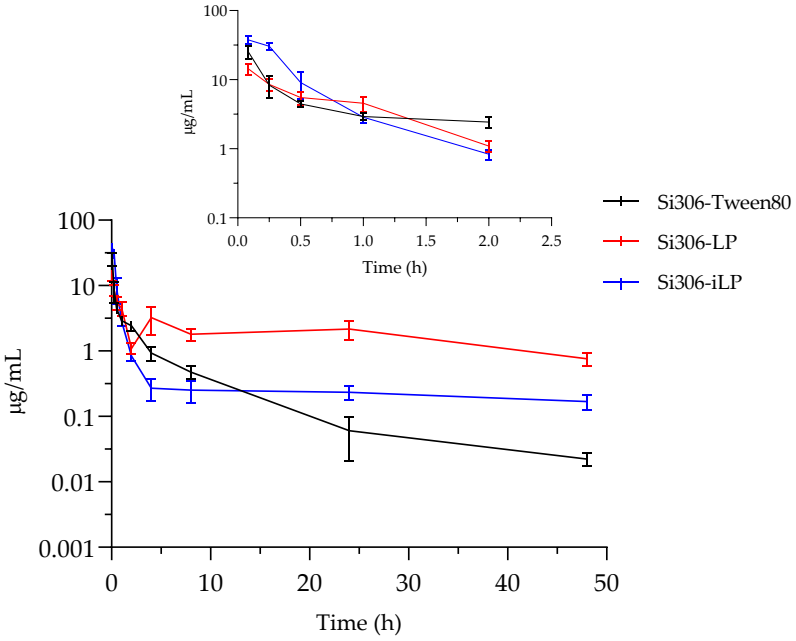

FIGURE 30. Plasma concentration-time curves (mean ± S.E.M., n=5) after i.v. administration of a single dose of Si306-Tween80 (black curve), Si306-LP (red curve) and Si306-iLP (blue curve) at the dosage of 25 mg/kg. The plasma concentration in the y-axis is expressed as $\log_{10}$ scale. The previously published plasma concentration-time curve of Si306-Tween80[152] is shown for comparison with those obtained from treatment with liposomal systems (except for the 48 h experimental points).

TABLE 13. Plasma PK parameters[a] of free Si306, Si306-LP and Si306-iLP evaluated after injection of a single dose of 25 mg/kg. The previously published PK parameters of Si306-Tween80[152] is shown for comparison with those obtained after treatment with liposomal systems.

Parameter	**Unit**	**Plasma**		
Formulation		**Si306-Tween80**	**Si306-LP**	**Si306-iLP**
Dose	mg/kg	25	25	25
$t_{1/2}$[b]	h	5.15	7.55	32.15
T_{max}[c]	h	0.08	0.08	0.08
C_{max}[d]	µg/mL	25.45	14.43	37.80
$AUC_{0\rightarrow 48h}$[e]	µg/mL×h	22.30	83.06	29.65
$AUC_{0\rightarrow \infty}$[e]	µg/mL×h	22.75	83.67	37.48
$MRT_{0\rightarrow \infty}$[f]	h	3.78	15.50	26.16
V_z[g]	L/Kg	8.17	3.25	30.95
CL[h]	L/h/Kg	1.10	0.30	0.67

[a]Calculated with PKSolver; [b]$t_{1/2}$: half-life. [c]T_{max}: time of maximum concentration observed. [d]C_{max}: maximum concentration observed. [e]AUC: area under the curve. [f]MRT: mean residence time [g]V: volume of distribution. [h]CL: clearance. PK data were evaluated using a non-compartment model.

By comparing the tissue distribution profiles obtained to the dosages of 5 and 25 mg/kg, a similar trend was observed for Si306 in free form as well as liposomal formulations, with proportionally higher tissue concentrations corresponding to the 5-fold higher dosage. Similarly, a high distribution of Si306 was observed in the lungs, liver, and spleen when the drug is delivered by liposomes (Figure 31a, b and c). In particular, for both liposomal formulations, the maximum tissue concentration in lungs was obtained after 30 minutes (128.48 and 303.78 μg/g for Si306-LP and Si306-iLP, respectively) while Si306 administered in free form reach its maximum concentration after 15 minutes (21.07 μg/g). In hepatic tissue, Si306 free (13.41 μg/g after 5 minutes) showed tissue concentrations 5- and 2.3-fold lower than Si306-LP (68.30 μg/g after 2 h) and Si306-iLP (30.32 μg/g after 5 minutes), respectively. The same trend is also observed in splenic tissue.

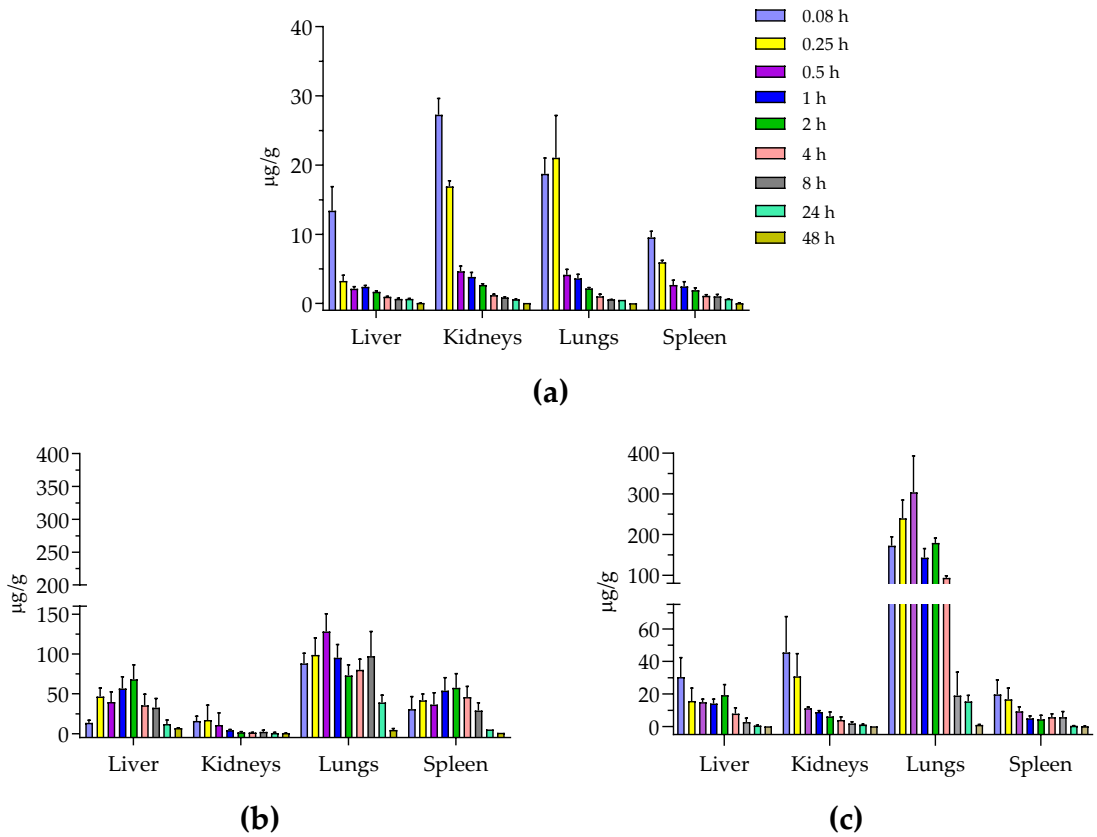

FIGURE 31. Biodistribution of **(a)** Si306-Tween80, **(b)** Si306-LP and **(c)** Si306-iLP at the dosage 25 mg/kg over 48 h (mean ± S.E.M., n=5) for the analyzed organs: liver, kidneys, lungs, and spleen. The previously published liver and kidneys distribution of Si306-Tween80[152] is shown for comparison with those obtained from treatment with liposomal systems (except for the 48 h experimental points).

The $AUC_{0\rightarrow 48h}$ values reported in the Table 14 confirmed the higher tissue uptake of Si306 when it is vehiculated by liposomes.

TABLE 14. $AUC_{0\rightarrow 48h}$ of liver, spleen, lungs, and kidneys after i.v. administration of Si306, formulated as Tween80 solution and both liposomal formulations at a single dose of 25 mg/kg.

	$AUC_{0\rightarrow 48h}$[a] (μg/mL×h)		
Tissue	**Si306-Tween80**	**Si306-LP**	**Si306-iLP**
Liver	31.80	931.21	116.98
Spleen	35.88	698.58	105.42
Lungs	34.48	2314.30	1361.65
Kidneys	41.69	65.69	89.78

[a]*Area Under the Curve evaluated using a non-compartment model (PKSolver Software).*

As far as liposomal formulations are concerned, the main difference between the two PK studies carried out is certainly the amount of phospholipids administered. To reach a dosage 5-fold higher, it was necessary to increase the amount of lipids to achieve an optimal encapsulation efficacy of the drug. Regarding the PK carried out at a dosage of 5 mg/kg, liposomal suspensions with a mean phospholipid concentration of 8-10 mg/mL were administered. On the contrary, for PK studies carried out at the dosage of 25 mg/kg, the mean PLs concentration was 18-21 mg/mL. Apparently, this could be an indication of toxicity but, comparing these liposomal formulations with the phospholipid concentrations of Doxil (the first FDA-approved lipid vector encapsulating doxorubicin), it can be noted that the total lipid content is approximately 16 mg/mL[147].

Moreover, the treatment of mice with Si306 free and encapsulated in liposomes did not produce treatment-related mortality at the doses of 5 and 25 mg/kg, and also, throughout the observation period, there were no significant changes in behavior, such as apathy, hyperactivity, vomiting, diarrhea, and morbidity, among the animals tested. During the experiment, all animals treated and sacrificed after 24 and 48 h were examined for any clinical signs, and no behavioral changes such as motor activity or posture were observed.

7.3 PK and Tumor Uptake in Neuroblastoma Orthotopic Mice Model

A preliminary evaluation of the PK and the distribution profile of Si306-Tween80 and Si306 delivered by both liposomal formulations was performed in an orthotopic mouse model of NB. Female athymic Nude-Foxn1nu mice (3 mice/group) were housed under pathogen-free conditions and injected in the right adrenal gland with 1 x 10^6 IMR-32 cells. Mice were i.v. treated 1 week after NB cells challenge, with 5 mg/kg of Si306 (Si306-Tween80, Si306-LP and Si306-iLP). Plasma concentration-time curves and PK parameters are shown in Figure 32 and Table 15, respectively. Plasma $AUC_{0\rightarrow 48h}$ values confirmed the results obtained in healthy mice: both liposomal formulations allow for a longer plasma circulation of the Si306 with $AUC_{0\rightarrow 48h}$ values 5- and 7-fold (Si306-LP and Si306-iLP, respectively) higher than the drug injected in free form.

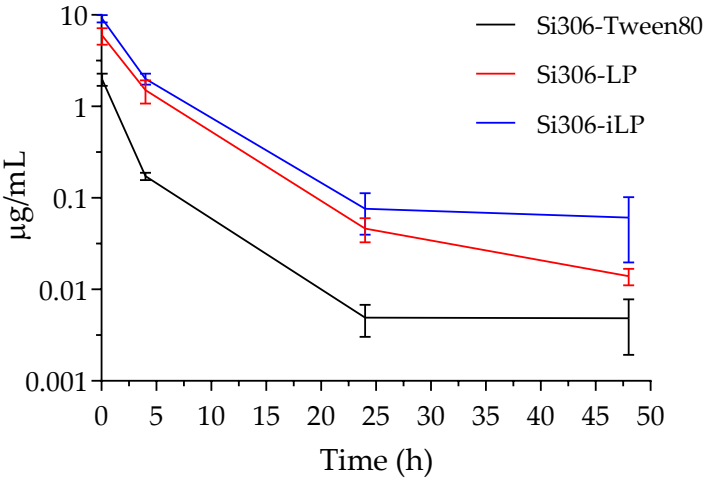

FIGURE 32. Plasma concentration-time curves (mean ± S.E.M., n=3) after i.v. administration of a single dose of Si306-Tween80 (black curve), Si306-LP (red curve) and Si306-iLP (blue curve) at the dosage of 5 mg/kg in IMR-32 tumor-bearing female mice model. The plasma concentration in the y-axis is expressed as $\log_{10}$ scale.

TABLE 15. Plasma PK parameters[a] of free Si306, Si306-LP and Si306-iLP evaluated after injection of a single dose of 5 mg/kg in IMR-32 tumor-bearing female mice model.

Parameter	**Unit**	**Plasma**		
Formulation		**Si306-Tween80**	**Si306-LP**	**Si306-iLP**
Dose	mg/kg	5	5	5
$t_{1/2}$[b]	h	8.83	6.63	9.29
T_{max}[c]	h	0.08	0.08	0.08
C_{max}[d]	µg/mL	1.98	5,95	9.11
$AUC_{0\rightarrow 48h}$[e]	µg/mL×h	6.27	31.32	45.06
$AUC_{0\rightarrow \infty}$[e]	µg/mL×h	6.33	31.45	45.97
$MRT_{0\rightarrow \infty}$[f]	h	2.80	3.59	5.05
V_z[g]	L/Kg	10.06	1.52	1.45
CL[h]	L/h/Kg	0.79	0.57	0.11

[a]Calculated with PKSolver; [b]$t_{1/2}$: half-life. [c]T_{max}: time of maximum concentration observed. [d]C_{max}: maximum concentration observed. [e]AUC: area under the curve. [f]MRT: mean residence time [g]V: volume of distribution. [h]CL: clearance. PK data were evaluated using a non-compartment model.

In tumor masses, a higher concentration of Si306 was detected when the drug is delivered by liposomes (Figure 33). Mice treated with Si306-iLP showed drug concentrations in tumor mass almost 2- and 4-fold higher than Si306-LP and Si306-Tween80 for both experimental points (24 and 48h) due to the presence of AntiGD2 which ensures active targeting of the drug by directing it towards the tumour mass.

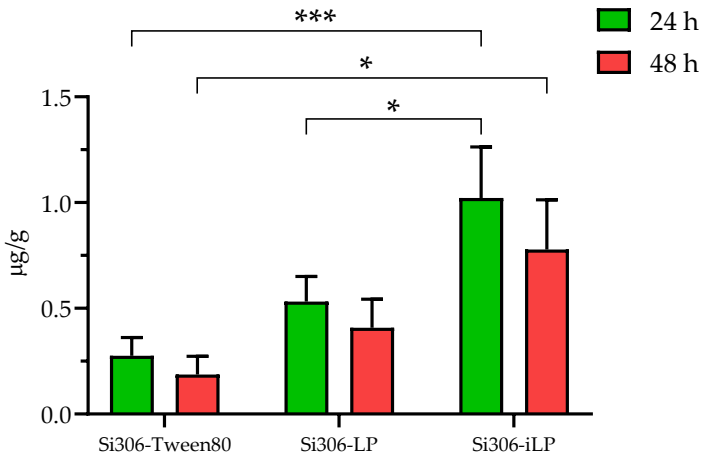

FIGURE 33. Amount of Si306 detected in tumor mass (mean ± S.E.M., n=3) at 24 and 48 h after treatment with Si306-Tween80, Si306-LP and Si306-iLP at the dosage of 5 mg/kg. A Tukey's two-way multiple comparisons test (ANOVA) was performed to test the significance of the observed differences. *indicates statistically significant differences between each treatment *vs* CTRL (*p<0.05, **p<0.01 and ***p<0.001).

8. *IN VIVO* THERAPEUTIC STUDIES

In vivo preliminary therapeutic study was performed on female athymic Nude-Foxn1nu mice [n=13 (CTR, n=12)] injected in the right adrenal gland with $1x10^6$ IMR-32-A-Luc cells on day 0, and treated on days 8, 14, 17, 21, and 24 post-inoculation of cells at a dose of 5 mg Si306/kg in free form and encapsulated in both liposomal formulations. The growth of the tumor masses was monitored daily by bioluminescence imaging (BLI). As shown in Figure 34, on day 29 no significant differences were observed for the treated mice groups compared to the controls (Figures 33a and 33b). On day 50, only mice treated with Si306-iLP showed a significant reduction ($p<0.01$) in tumor mass growth of approximately 50% compared to controls (Figure 33c).

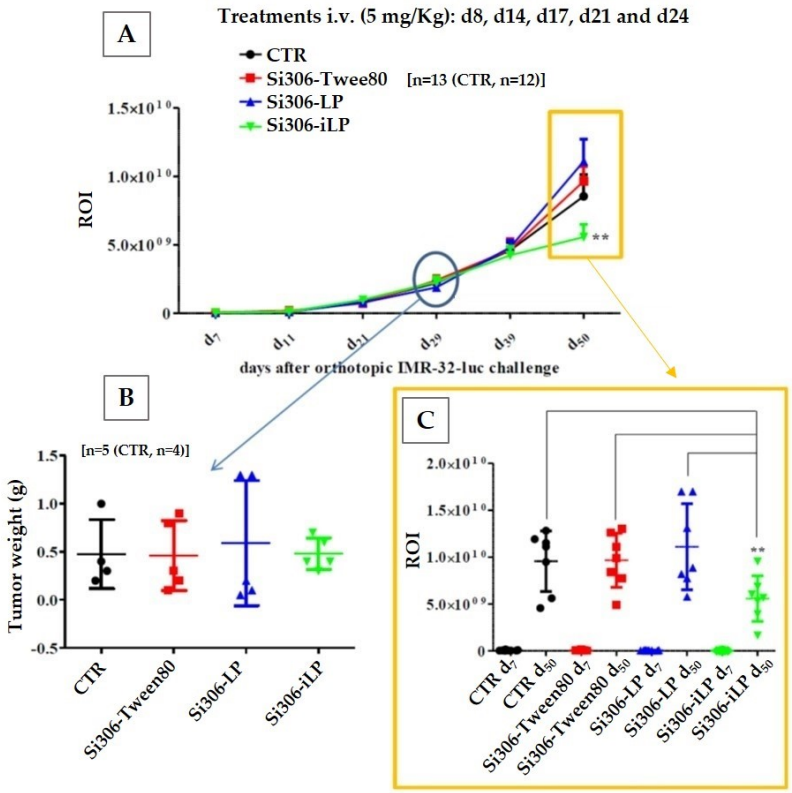

FIGURE 34. *In vivo* preliminary therapeutic assay on female athymic Nude-Foxn1nu mice [n=13 (CTR, n=12)]. Mice were injected into the right adrenal gland with $1x10^6$ IMR-32-A-Luc cells on day 0 and treated on days 8, 14, 17, 21, and 24 post-inoculation of cells at the dose of 5 mg Si306/kg in free form (Si306-Tween80, in red), encapsulated in stealth liposomes (Si306-LP, in blue), encapsulated in immunoliposomes (Si306-iLP, in green) and Hepes buffer (control, in black). (A) Tumor mass monitoring from day 0 to day 50 using BLI. (B) Tumor masses collected and weighed 29 days post-inoculation of cells. (C) Si306-iLP showed a significant reduction (**$p<0.01$) in tumor mass growth of approximately 50% compared to controls.

The results obtained from the preliminary *in vivo* therapeutic study performed on tumor-bearing mice at the dosage of 5 mg Si306/Kg, led to the decision to proceed with the survival study at the dosage of 25 mg/kg. In this study, female athymic Nude-Foxn1nu mice (n=7/group) were injected into the right adrenal gland with $1.5x10^6$ IMR-32 cells on day 0 and treated on days 6, 9, 13, 16, 20, 23, 27, and 30 post-inoculation of cells. As shown in Figure 35 and Table 16, Si306 encapsulated in stealth liposomes (Si306-LP) showed a significant 4-day increase in survival rate compared with control; whereas mice treated with Si306 free (Si306-Tween80) did not show an increase in survival. Instead, a significant median survival (11 days longer) was obtained for mice treated with Si306-iLP compared to controls and mice treated with Si306-Tween80.

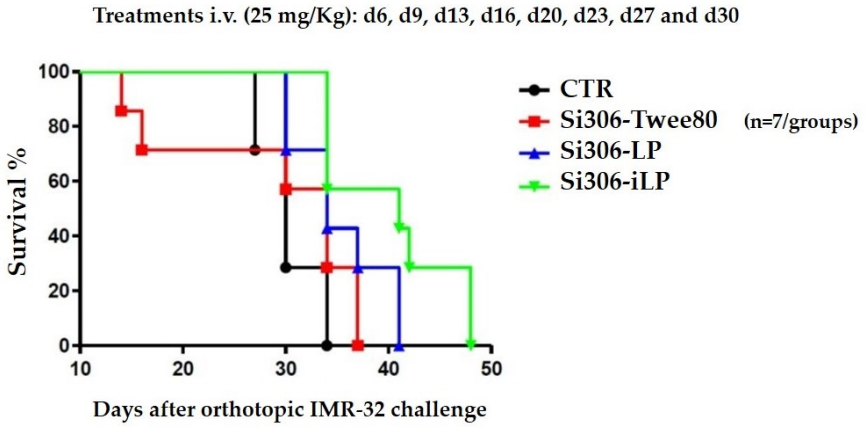

FIGURE 35. Survival of tumor-bearing mice after various treatments. Treatment groups (n=8/group) consisted of Si306-Tween80 (in red), Si306-LP (in blue) and Si306-iLP (in green), and Hepes buffer (control in black). Mice were injected in the right adrenal gland with $1.5x10^6$ IMR-32 cells on day 0 and treated on days 6, 9, 13, 16, 20, 23, 27, and 30 post-inoculation of cells at a dose of 25 mg Si306/kg.

TABLE 16. Median survival days after treatments. P-values for significant differences observed between the different experimental groups.

Treated group	Median Survival	Statistics (p- value[a])	
CTR	30 days	CTR *vs.* Si306-LP	0.0305 (*)
Si306-Tween80	30 days	CTR *vs.* Si306-iLP	0.0029 (**)
Si306-LP	34 days	Si306-Tween80 *vs.* Si306-iLP	0.0191 (*)
Si306-iLP	41 days		

[a]Tukey's two-way multiple comparisons test (ANOVA) was performed to test the significance of the observed differences (*p<0.05, **p<0.01 and ***p<0.001).

DISCUSSION AND CONCLUSIONS

Si306, a pyrazolo[3,4-*d*]pyrimidine derivative, has been identified as a very promising agent for the treatment of neuroblastoma. This compound has shown a favorable *in vitro* and *in vivo* activity profile against NB models. Nevertheless, the good antitumor activity of Si306 is associated with sub-optimal aqueous solubility, which might hinder its further development. In this context, drug delivery systems were developed to overcome the poor aqueous solubility obtaining suitable formulations for their *in vivo* use in the treatment of neuroblastoma. Si306 was encapsulated in I. Stealth liposomes (Si306-LP) and II. immunoliposomes decorated with AntiGD2 monoclonal antibody (Si306-iLP), which specifically binds GD2 antigen expressed by NB cells. Liposome suspensions were prepared by the thin layer evaporation method and were characterized in terms of encapsulation efficiency (EE%), size, and ζ-potential. Si306-LP showed an EE% greater than 77% while Si306-iLP showed EE% values in the range of 57-77%. Both liposomal formulations were suitable for their *in vivo* use showing mean size and ζ-potential of Si306-LP and Si306-iLP of 126 nm and -22.6 mV and, 133 nm and -19.3 mV, respectively. Furthermore, Si306-LP and Si306-iLP were characterized by cryo-TEM and images suggested the presence of a homogeneous population of unilamellar liposomes with size around 100 nm, free from oversized or multilamellar liposomes and free from drug crystals. Particle size has a significant impact on circulation time in that, particle size affects cellular uptake and especially the rate of clearance by the MPS (the larger the nanoparticles, the faster their recognition and consequently elimination)[148]. The optimal size to facilitate extravasation is about 150 nm or less. In this context, this study has shown that both liposomal formulations represent a suitable drug delivery system with optimal average size. Another important feature for the stability of nanoparticle dispersion is the ζ-potential, which indicates the degree of electrostatic repulsion between the particles. In detail, nanoparticles with ζ-potential values greater than +25 mV or less than -25 mV typically have high degrees of stability[149]. Both liposomal formulations have been proved to be stable

over a period of 14 days, with no significant increase in mean particle diameter and PDI values. Also, liposomes showed very poor leakage, retaining >95% of encapsulated drug, for 96 h. Confirmation of the presence of the conjugated antibody on the liposomal surface (Si306-iLP) has been obtained by colorimetric protein quantification (BCA assay). The levels of coupled-AntiGD2 were estimated in a range of 8-14 μg/μmol of PLs (25-27 μg/200 μL of injected volume per mouse for *in vivo* experiments).

Liposomal suspensions showed enhanced cytotoxic activity against NB cell lines. Si306-iLP showed higher cytotoxic activity than Si306 dissolved in DMSO in all NB lines tested. In addition, both liposomal formulations were found to be safer, in terms of cytotoxicity on human fibroblast cell line, showing a 2-fold higher IC_{50} values than the free drug. Taking into consideration the data obtained from stability testing and *in vitro* release, it seems likely that the cytotoxicity results for liposomal formulations (especially for Si306-iLP) are not attributable to the release of Si306 from the liposomal nanoparticle and subsequent cellular uptake of the drug released in free form, but rather to their internalization and subsequent release of Si306 at the intracellular level. This is particularly evident for Si306-iLP that thanks to the presence of antiGD2, makes them able to bind to the cell membrane facilitating the internalization. This aspect has been confirmed by cell association assays where only liposomes decorated with AntiGD2, due to the interaction with the antigen, showed the ability to bind and be internalized in different NB cells and the cellular association increases proportionally with increasing GD2 antigen expression.

The pharmacokinetic (PK) and tissue biodistribution (BD) profiles were evaluated by treating BALB/c healthy mice intravenously at two dosages of 5 and 25 mg/kg. Six groups of mice were treated with three formulations: I. Si306 dissolved in citric acid solution in presence of Tween80 and benzyl alcohol as co-solvents, II. Si306-LP and III. Si306-iLP. By comparing the plasma concentration-time curves, a higher plasma exposure of Si306 was observed with a slower elimination from the

bloodstream of the drug when it is delivered by liposomes compared to Si306 administered in free form. This trend is also confirmed by comparison of PK parameters obtained after administration at both dosages where MRT and CL values confirm a higher permanence of Si306 when it is administered and delivered by liposomes. This represents the achievement of one of the primary objectives of this work: the development of a long-circulating drug delivery system, which allows increased blood exposure to the drug. An immediate distribution of Si306 followed by a concentration decrease in a time-dependent manner was observed in all organs analyzed. An increased concentration of Si306 was observed in the liver, spleen, and lungs when it is delivered by liposomes, with a larger amount of Si306 available for a more efficient target of the tumor area. This hypothesis was confirmed by a preliminary evaluation of the PK and the tumor distribution profile of Si306-Tween80, Si306-LP, and Si306-iLP in an orthotopic mice model of NB. 24 and 48 hours post-treatment with Si306 5 mg/kg, blood and tumor masses were collected from all mice and analyzed. Results showed an increased tumor uptake of Si306 when it is encapsulated in liposomes compared to free drug, especially for Si306-iLP which showed 2- and 4-fold higher drug concentration in tumor masses than Si306-LP and Si306-Tween80, respectively.

Finally, *in vivo* efficacy and survival studies were conducted on orthotopic NB mice models. Si306-iLP showed a significant 50% reduction in tumor growth and more importantly, showed an increased survival rate (by 11 days) compared to controls and mice treated with Si306-Tween80.

In conclusion, a long-circulating liposomal drug delivery system for Si306 has been developed, capable of high encapsulation efficiency and stability during the time. The liposomal systems have been proved to reach the tumor in high concentration and with a very slow clearance, exploiting not only passive targeting (EPR effect) but especially active targeting mediated by AntiGD2 antibody. AntiGD2 decorated immunoliposomes encapsulating Si306 led to a greater therapeutic response, showing a reduction in tumor growth and a significant increase in survival rate.

MATERIALS AND METHODS

1. DRUGS AND MATERIALS

Si306 was synthesized, characterized and published by our group[150]. AntiGD2 monoclonal antibody was purchase from Polo GGB - Siena, Italy. All reagents, solvents and materials were purchased from Sigma Aldrich Srl (Milan, Italy). Phospholipids used for the preparation of liposomes were purchased from Avanti Polar Lipids (Alabama, USA).

2. PREPARATION OF SI306-LP

Stealth liposomes loaded with Si306 were prepared using the thin layer evaporation method.

Si306 and the phospholipids DPPC (1,2-dipalmitoyl-sn-glycero-3-phosphocholine), POPC (1-palmitoyl-2-oleoyl-sn-glycero-3-phosphocholine), DPPE-PEG_{2000} (N-(Carbonyl-methoxypolyethylenglycol2000)-1,2-dipalmitoyl-sn-glycero-3-phosphoethanolamine sodium salt) (molar ratio 0.3:0.7:0.04, respectively) and cholesterol (15% of the total moles of DPPC, POPC and DPPE-PEG_{2000}) were dissolved in a mixture of chloroform/methanol (3:1 v/v) and transferred into a round-bottom flask. The organic solvents were removed by rotary evaporation under vacuum at 37 °C and then under nitrogen flow to remove any remaining solvent residues. The dried lipid film obtained was then hydrated in 25 mM HEPES and 140 mM NaCl buffer (pH 7.4) under continuous mechanical agitation at 60 °C. The liposomal suspension was extruded at a temperature of 60° C through polycarbonate membranes with a pore size of 0.2 μm (5 passages) first, and 0.1 μm (10 passages) then; mainly unilamellar vesicles were obtained. Residues of unencapsulated Si306 were removed from the liposomes by size-exclusion chromatography, passing the liposomal suspension through a Sephadex G-25 column in 25 mM HEPES and 140 mM NaCl buffer (HEPES buffer), pH 7.4. Finally, drug encapsulation efficacy (%EE) and amount of cholesterol were determined by UV/LC-MS analysis.

3. PREPARATION OF SI306-ILP

AntiGD2-decorated immunoliposomes loaded with Si306 composed by phospholipids DPPC, POPC, DPPE-PEG_{2000}, DSPE-PEG_{2000}-Maleimide (molar ratio 0.3:0.7:0.04:0.006 respectively) and cholesterol (15% of the total moles of DPPC, POPC and DPPE-$mPEG_{2000}$) have been prepared in the same way described above for the preparation of Si306-LP, obtaining unilamellar veshicles with maleimide-terminated polyethylene glycol-DSPE chains. To obtain the coupling between AntiGD2 and maleimide terminus, AntiGD2 molecules (previously concentrated from 2.5 to 8-10 mg/mL, using Amicon filters 30K) are firstly functionalized via Traut's reagent (2-iminothiolane, 25mM) at a molar ratio of 20:1 (Traut's: mAb) for 1 h at room temperature in HEPES buffer pH 8.0 (Figure 36). This takes advantage of the selective reaction between the primary amine groups and 2-iminothiolane by obtaining amidines with terminal sulfhydryl groups. The use of this reagent is very advantageous as it does not alter the charge properties of the protein and consequently, its solubility. Unreacted Traut's reagent was removed via size-exclusion chromatography using Bio-Gel P-6 desalting Cartridge column. The quantification of activated-AntiGD2 was performed by using Bradford protein quantification assay (for more details see paragraph 4.4.1). In parallel, performing Ellman assay (see paragraph 4.3), 1 free -SH group per antibody has been estimated.

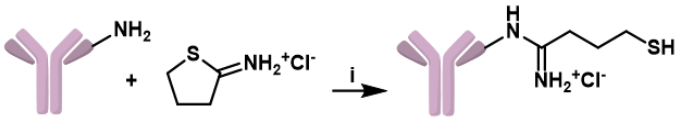

FIGURE 36. AntiGD2 activation via Traut's reagent reaction. i) 1 h at room temperature in 25 mM HEPES and 140 mM NaCl buffer (pH 8.0).

After that, the activated-AntiGD2 solution was concentrated using Amicon filters 30K. The rationale of this step is to obtain a smaller volume of activated antiGD2 solution to minimize the dilution of the Si306-loaded liposomal suspension for the final coupling reaction.

Finally, the coupling reaction was run at a molar ratio of 1:4500 (AntiGD2: PLs), for 16 h at 5 °C in continuous slow magnetic stirring (Figure 37). Uncoupled mAb

molecules were separated from the liposome suspension passing the coupling mixture through a Sepharose CL-4B column in HEPES buffer (pH 7.4).

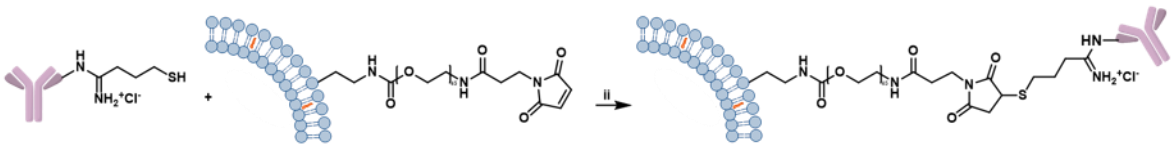

FIGURE 37. Coupling reaction. ii) 16 h at 5 °C in 25 mM HEPES and 140 mM NaCl buffer (pH 7.4).

The quantification of the coupled AntiGD2 was performed by using bicinchoninic acid assay (BCA assay, see paragraph 4.4.2), then quantification of Si306 and cholesterol were determined by UV/LC-MS analysis by reference to the appropriate calibration curve.

4. CHARACTERIZATION OF LIPOSOMAL FORMULATIONS

Both liposomal formulations have been fully characterized by evaluating their drug encapsulation efficiency, amount of PLs (by quantifying cholesterol), morphology, and physiochemical properties. For AntiGD2-decorated liposomes (Si306-iLP), the quantification of liposome surface-conjugated mAb was also performed.

4.1 DRUG ENCAPSULATION EFFICIENCY

Encapsulation efficiency percentage (EE%) for both liposomal formulations was determined by UV/LC-MS analysis. Liposomal suspension aliquots were treated with ethanol in 1:10 v/v ratio to extract, which was quantified by UV/LC-MS by reference to the appropriate calibration curve (for details regarding instrumentation and analysis condition, see Paragraph 7. of the Materials and Methods section). Liposomal encapsulation was measured with respect to the amount of compound initially added to the organic solution, using the following equation:

$$EE\% = \frac{Encapsulated\ Drug\ (mg)}{Total\ Drug\ (mg)} \cdot 100$$

EE% is a measure of how much drug must be used to load a given amount of drug.

4.2 PHYSIO-CHEMICAL PROPERTIES

Liposomes were analyzed by Zeta Sizer Nano ZS90 (Malvern Instruments) for mean size (nm), PDI and ζ-potential (mV). The liposomal suspension was diluted with ultrapure water to achieve the suitable scattering intensity to obtain optical density (OD) of 0.1 unit of absorbance at 420 nm and then measured at 25° C with a scattering angle of 90°. Z-potential measurements were carried out using folded capillary cells (Malvern). Results are expressed as mean values ± S.D. calculated from three independent experiments (n=3).

Liposome morphology was also observed by cryo-TEM. Briefly, 3 µL of the sample were applied on Quantifoil® holey carbon grids and then frozen in liquid ethane to achieve sample vitrification. Frozen samples were stored in liquid nitrogen until EM imaging. Vitrified samples were imaged using a CM200 FEG transmission EM. EM images were acquired at 27,500x magnification (pixel size 0,602 nm) at -12, -18 µm defocus.

4.3 ELLMAN ASSAY

Ellman's reagent is 5,5'-dithio-bis-(2-nitrobenzoic acid), also known as DTNB, has been used to quantify the free sulfhydryl groups obtained following the activation of AntiGD2 with Traut's reagent. A solution of this compound produces a yellow product when reacting with the sulfhydryl groups. This yellow-colored product can be quantified using a spectrophotometer based on its strong absorbance at 412 nm (Figure 38).

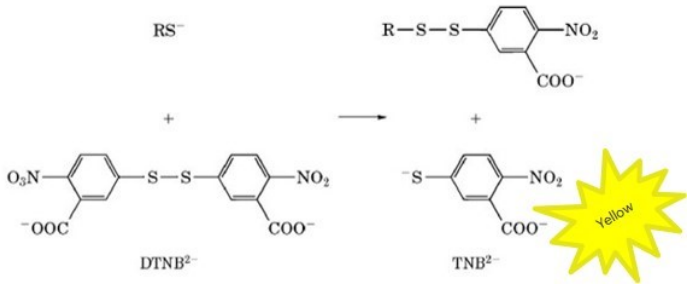

FIGURE 38. DTNB reaction with free sulfhydryl groups.

Briefly, in a 96-well plate, 25 µL of sample/standard solution in PBS 0.1 M pH 8.0 containing 1 mM EDTA were added to 50 µL of Ellman's 5 mM reagent solution in

PBS 0.1 M pH 8.0. This was mixed and incubated for 15 min at room temperature. At the end of the incubation period, quantification was performed by spectrophotometry (Multiskan™ FC Microplate Photometer, Thermo Fisher Scientific) by measuring the absorption at 412 nm. The -SH groups on the mAb were quantified using an appropriate calibration curve prepared with L-cysteine.

4.4 AntiGD2 Quantification Assays

4.4.1 Bradford Assay

The quantification of AntiGD2, after functionalization with Traut's reagent, was performed via colorimetric protein determination with Coomassie Brilliant Blue G-250 (Bradford Assay, Figure 39). Briefly, in a 96-well plate, 10 µL of each sample/standard solution was added to 200 µL of a solution composed by Coomassie Brilliant Blue: ultrapure H_2O (1:0.5 v/v). After 15 min of incubation, the determination was performed spectrophotometrically by measuring the absorption at 595 nm (Multiskan™ FC Microplate Photometer, Thermo Fisher Scientific).

Figure 39. Absorbance shift of the dye Coomassie Brilliant Blue G-250 in which under acidic conditions the red form of the dye is converted into its bluer form to bind to the protein being assayed.

The quantifications were performed by reference to the appropriate calibration curve freshly prepared using a generic rabbit IgG.

4.4.2 BCA ASSAY

The Quantification of AntiGD2 conjugated on the liposome surfaces was performed by using QuantiPro™ BCA Assay Kit. The principle of the bicinchoninic acid (BCA) assay is relying on the formation of a Cu^{2+}-protein complex under alkaline conditions, followed by reduction of the Cu^{2+} to Cu^{1+}. The amount of reduction is proportional to the amount of protein present in the sample (Figure 40).

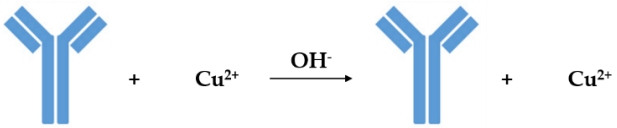

FIGURE 40. Cu^{2+}-protein complex under alkaline conditions following reduction to Cu^{1+}.

BCA forms a purple-blue complex with Cu^{1+} in alkaline environments, thus providing a basis to monitor the reduction of alkaline Cu^{2+} by proteins (Figure 41).

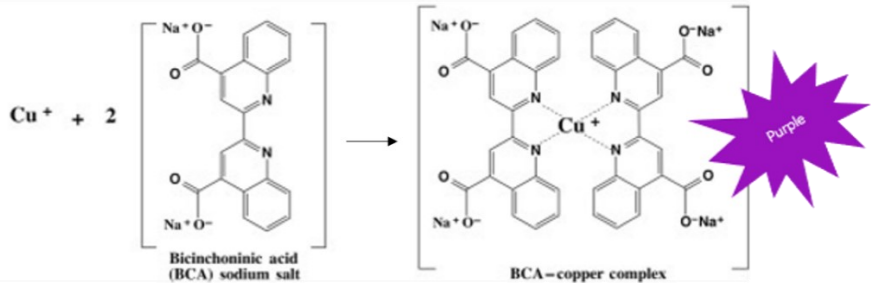

FIGURE 41. BCA-Copper (I) complex.

The QuantiPro Working Reagent is prepared by mixing 1 part of Reagent QA (Na_2CO_3, sodium tartrate, and $NaHCO_3$ in 0.2 M NaOH, pH 11.25) with 1 part of Reagent QB (bicinchoninic acid solution 4% w/v, pH 8.5). After QA and QB have been combined, 0.04 parts of Reagent QC (copper (II) sulfate) were added and mixed until a uniform color is obtained. Briefly, in a 96-well plate, 50 µL of sample/standard solutions were mixed with 50 µL of QuantiPro Working Reagent (1:1 v/v). After 2 h of incubation at 37 °C, the determination was carried out spectrophotometrically by measuring the absorption at 562 nm (Multiskan™ FC Microplate Photometer, Thermo Fisher Scientific) and the quantifications were performed by reference to the appropriate calibration curve freshly prepared using a generic rabbit IgG. The blank solution required for spectroscopic analysis (pre-

coupling liposomal suspension) was diluted with HEPES buffer pH 7.4 according to the amount of cholesterol in the sample (Si306-iLP) to obtain the same lipid amount. Subsequently, both the blank and the sample were diluted 1:10 with ultrapure H_2O to obtain an antibody concentration not exceeding 0.5-30 mg/mL.

4.5 STABILITY STUDIES

Both liposomal formulations were stored at 4°C for 2 weeks. The samples were analyzed for the changes in particle size, ζ potential, and PDI at fixed time intervals by DLS measurements.

4.6 *IN VITRO* RELEASE

Si306 release from its liposomal formulations was evaluated by dialysis. The release assay for Si306 has been evaluated for both Si306-LP and Si306-iLP. Si306-loaded liposomal samples have been sealed in a dialysis bag (cut off 10 kDa) and dialyzed against 20 mL of PBS (pH 7.4), 50 mg/mL of BSA (Bovine serum albumin at physiological plasma concentration). The entire release medium was gently stirred at 37 °C. At predetermined time intervals (0, 1, 2, 4, 6, 24, 48, and 72 h), 0.5 mL of release medium was collected and complemented with fresh PBS buffer at the same temperature. The sample solution was treated with 1.5 mL of ACN and centrifugated at 5000 rpm for 20 minutes. The supernatant obtained was dried under nitrogen, resuspended in 0.1 mL of methanol, and analyzed by UV/LC-MS as described in the Materials and Methods section, Paragraph 7.

5. ANIMALS FOR PK AND BD STUDIES

Naive BALB/C mice (aged 4-6 weeks, Charles Rivers - Milan, Italy) were maintained under pathogen-free conditions and given food and water *at libitum*. The adaption period to the environment was not less than seven days. All the procedures used on animals in this study were approved by Institutional Animal Use and Care Committee at Università degli Studi di Siena and authorized by the Italian Ministry of Health, according to Legislative Decree 116/92, which implemented the European

Directive 86/609/EEC on laboratory animal protection in Italy. Methods for all the conducted experiments were performed in accordance with regulations, standards, and guidelines of the Animal Use and Care Committee of Università degli Studi di Siena.

6. *IN VIVO* ADMINISTRATION OF SI306

To compare the PK and BD profile of Si306-loaded stealth liposome and immunoliposome formulations with its "free drug" profile, Si306 was dissolved in a mixture of Tween80 (10% v/v), benzyl alcohol (1% v/v) and a 10 mM solution of citric acid. For all formulations, the compound was administered intravenously (caudal tail vein) as a single dose of 5 and 25 mg/kg in 200 μL of volume. At several time points (0.08, 0.25, 0.5, 1, 2, 4, 8, 24 h, and 48 h), after drug administration, mice were treated intraperitoneally with heparin (5000 U/kg) and sacrificed under CO_2. Five animals were used for each time point. Blood, liver, lungs, spleen, and kidneys were collected. Approximately 500-600 μL of blood was collected from each animal and transferred to a tube containing 10 μL of heparin and mixed briefly. The quantification of Si306 in blood and organs after treatment with a dosage of 5 mg/kg was performed by LC-MS/MS, while for the dosage of 25 mg/kg the analyses were carried out using LC-UV/MS. The PK parameters, including area under the concentration-time curve (AUC), maximum plasma concentration (C_{max}), half-life ($t_{1/2}$), apparent volume of distribution (V), clearance (CL) and mean residence time (MRT), were calculated by non-compartmental analysis using PKSolver software[151].

6.1 SAMPLE PREPARATION

Blood samples were centrifuged at 5000 rpm for 20 min to separate the plasma fraction, which was subsequently collected in a test tube. 1 mL of ACN solution containing Si34[152] (a pyrazolo[3,4-*d*]pyrimidine compound already used as internal standard, IS) at the concentration of 5 μg/mL was added to each sample to denature proteins. Samples were centrifuged at 5000 rpm for 20 min, and the supernatant was recovered, dried un nitrogen flow, solubilized again in MeOH (100 μL), and

analyzed. Organs (approx. 200 mg of tissue) were homogenized using a T10 basic ULTRA-TURRAX® homogenizer; to extract the compound from the tissue, ACN IS solution was added (1.5 mL at the concentration of 5 μg/mL), and the homogenate was centrifuged at 5000 rpm for 20 min. The supernatant was recovered, filtered, and analyzed. The quantification of each compound was performed by reference to the appropriate calibration curve.

6.2 Evaluation of the Matrix Effect and Assay Validation

The evaluation of the possible absence or presence of matrix effect %ME (ionization suppression or ionization enhancement) was evaluated by analyzing 3 sets of solutions:

- **A.** Si306 solutions present in the neat reconstitution solvent (LC mobile phase) were directly analyzed at prefixed concentrations.
- **B.** Mice plasma/organs samples were first extracted and spiked *after* extraction with Si306 in the same solvent (mobile phase). Any additional variability of the peak areas for Si306 than those observed in set **A** would be indicative of an effect of sample matrix since Si306 at the same concentrations were spiked into plasma/organ extracts.
- **C.** Si306 was spiked *before* extraction into plasma/organ samples as in set **B**.

Each concentration point for each set of solutions (**A**, **B** and **C**) was prepared in triplicate.

By using the mean peak areas obtained in Si306 neat solution (**A**), the corresponding mean peak areas for Si306 spiked *after* extraction into plasma/organ extracts (**B**), and mean peak areas for Si306 spiked *before* extraction (**C**), the %ME, recovery (%RE) and process efficiency (%PE) can be calculated as follows[153]:

$$\%ME = \frac{B}{A} \times 100 \quad (1)$$

$$\%RE = \frac{C}{B} \times 100 \quad (2)$$

$$\%PE = \frac{(\%ME \times \%RE)}{100} \quad (3)$$

The matrix effect and recovery of the IS were evaluated in a similar manner.

7. UV/LC-MS AND LC-MS/MS METHODS

UV/LC-MS analyses were performed by using Agilent 1100 LC/MSD VL system (G1946C) (Agilent Technologies, Palo Alto, CA) constituted by a vacuum solvent degassing unit, a binary high-pressure gradient pump, an 1100 series UV detector, and an 1100 MSD model VL benchtop mass spectrometer. MSD single-quadrupole instrument was equipped with the orthogonal spray API-ES (Agilent Technologies, Palo Alto, CA). The pressure of the nebulizing gas and the flow of the drying gas (nitrogen used for both) were set at 40 psi, 9 L/min, respectively. The capillary voltage, the fragmentor voltage, and the vaporization temperature were 3000 V, 70 V, and 350 °C, respectively. MSD was used in the positive and negative ion mode. Spectra were acquired over the scan range m/z 50–1500 using a step size of 0.1. Chromatographic analysis for drug encapsulation efficacy in the liposomal formulation, *in vivo* studies (Si306 and Si34 quantifications), and in general, the quantifications of Si306 were performed using a Phenomenex Kinetex EVO C18-100Å (150 x 4.6 mm, 5 μm particle size) at room temperature, at flow rate of 0.6 mL/min, and injection volume of 20 μL, operating with a gradient elution of A: water (H_2O) and B: acetonitrile (ACN). Both solvents were acidified with 0.1% v/v of formic acid. UV detection was monitored at 254 nm. Table 17 shows the gradient elution condition used for all described analyses.

TABLE 17. LC gradient elution used for the quantification of Si306.

LC Gradient Elution		
Time (min)	**%A** (H_2O/FA 0.1% v/v)	**%B** (ACN/FA 0.1% v/v)
0	95	5
1	95	5
10	5	95
19	5	95
20	95	5

For cholesterol quantifications, required during the preparation of liposomal formulations, were performed using the same chromatographic column and setting instrumentation described above, operating with an isocratic elution of methanol (MeOH) for 10 min. UV detection was monitored at 210 nm.

Analyses of blood samples and organs collected (PK at the dosage of 5 mg/kg), recovery, and matrix effect determination were performed by LC-MS/MS system consisted of HPLC Agilent 1200 Series (Agilent Technologies, Italy) coupled with a mass spectrometer TSQ Quantum Access (Thermo Scientific, Italy), equipped with electrospray ion source (ESI) and triple quadrupole analyzer. The Xcalibur software (Thermo Scientific) was available for managing the instrument, collecting, and analyzing data. The ESI-MS conditions were optimized through the direct injection of a Si306 standard solution (as well as for Si34), in negative ion current mode, using nitrogen as atomizing gas. The transitions as well as the capillary voltage and the collision energy used are appropriated for each tested compound. Preliminarily, to identify the analytes and relevant retention times, selected samples were analyzed on TIC mode (Total Ion Current) in the range of 300–1000 m/z. Then the quantification of selected species was carried out via SIM (single ion monitoring) method. Chromatographic separation was obtained using a Phenomenex Kinetex C18-100Å column (30 x 2.1 mm) with 2.6 μm particle size (bearing a guard column Phenomenex SecurityGuard™ ULTRA Holder) and operating with the same gradient elution described above. The flow rate was 0.2 mL/min and the injection volume was 5 μL. The analytical quantifications were performed by comparison with appropriate calibration curves using Si34 as internal standard, and calibration curves were acquired daily (in duplicates).

SECTION 2

AUNP PYRAZOLO[3,4-*d*]PYRIMIDINE NANOSYSTEM IN COMBINATION WITH RADIOTHERAPY AGAINST GLIOBLASTOMA

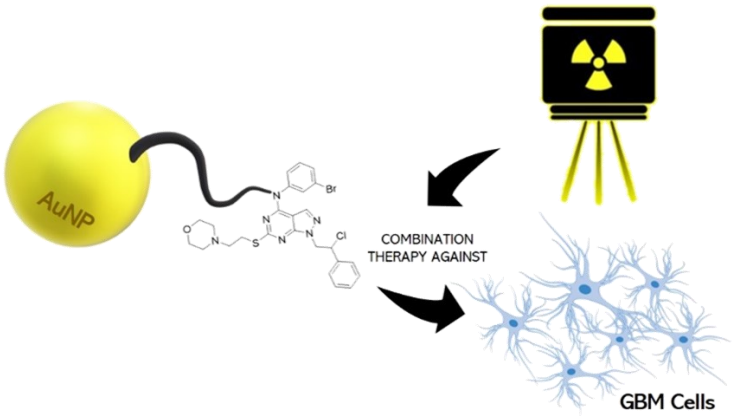

TAKEN FROM:

Alessio Molinari, Giulia Iovenitti, Arianna Mancini, Giovanni Luca Gravina, Monia Chebbi, Maura Caruana, Giulia Vignaroli, Francesco Orofino, Enrico Rango, Adriano Angelucci, Elena Dreassi, Silvia Schenone and Maurizio Botta. AuNP Pyrazolo[3,4-*d*]pyrimidine Nanosystem in Combination with Radiotherapy Against Glioblastoma. Reprinted with permission from *ACS Med. Chem. Lett.* **2020**, 11, 5, 664–670. Copyright 2020 American Chemical Society.

AIM OF THE PROJECT

Glioblastoma (GBM) is an aggressive intracranial tumor associated with high morbidity and mortality. The major issues associated with therapeutic failure are represented by the selection of an effective molecular target and the penetration of the blood-brain barrier (BBB). For these reasons, novel therapeutic approaches are needed to improve the prognosis of GBM patients, which still remains an unmet medical need. In this context, aberrant regulation of tyrosine kinases (TKs) associated with different types of cancer including GBM, may be exploited for the development of novel therapeutic agents. One of the most studied and promising targets in GBM is the protooncogene c-Src, a non-receptor tyrosine kinase whose inhibition by several agents is currently being evaluated in the clinical phase. Pyrazolo[3,4-*d*]pyrimidine derivatives, a promising class of c-Src TK inhibitors have been extensively studied by our research group. They exhibited strong antiproliferative and pro-apoptotic effects toward several cancer cell lines, including neuroblastoma, chronic myeloid leukemia, and GBM. In particular, compound Si306 has shown a very good activity profile against GBM, alone or in combination with RT, both *in vitro* toward U87 cell line and *in vivo* in both subcutaneous and intracranial GBM (U87 cells) models. Si306 was able to reduce the tumor mass volume by 40% when used alone and by 80% in combination with RT. Nevertheless, the good antitumor activity of these promising compounds is usually associated with sub-optimal aqueous solubility, which might hinder their further development. In this context, nanomedicine seems to be the most versatile approach to design anticancer agent carriers, target delivery, and tumor imaging systems, with the aim to overcome poor biodistribution characteristics and therapeutic resistance issues. Nanometer-scale particles are able to better extravasate into brain tumor tissue, due to the enhanced permeability and retention (EPR) effect, allowing a more efficient uptake of therapeutic molecules across the BBB. In particular, gold nanoparticles (AuNPs)-conjugated drugs represent a promising and innovative antitumor therapeutic and diagnosis approach due to

their low toxicity, ideal contrast agent properties for molecular Computed Tomography imaging, the possibility of functionalization with various chemotherapeutic agents or targeting ligands, and ability to enhance the efficacy of RT *in vitro* and *in vivo*. In this regard, this study will focus on the design, synthesis, preparation, and characterization of AuNPs conjugated to pyrazolo[3,4-*d*]pyrimidine derivative Si306. The loading efficiency and stability in polar media and human plasma will be evaluated for AuNPs-Si306 nanoparticles. Besides, the morphological profile in terms of size and ζ-potential will be evaluated. Finally, the *in vitro* antitumor activity of AuNPs-Si306 in the glioblastoma (GBM) model, also in combination with radiotherapy (RT), will be investigated.

RESULTS

1. PREPARATION OF Si306-LINKER

Synthesis and characterization of Si306 were previously reported[49]. First of all, the synthetic approach to prepare the Si306-linker/hydrolyzable function-derivative (**5**) was set up and developed in good yield as summarized in Figure 42.

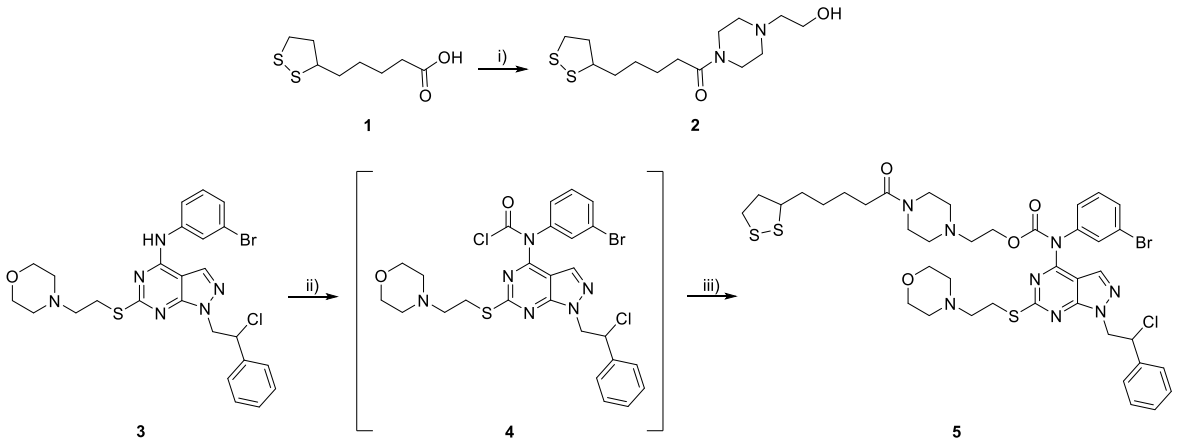

FIGURE 42. Preparation of SI306-linker/hydrolyzable function. Reagents and Conditions: i) 1-(2-hydroxyethyl)piperazine, HOBt, EDC.HCl, CH2Cl2, r.t, 12 h. ii) NaHCO3, triphosgene, CH2Cl2 dry, from 0 °C to r.t., 6 h. iii) linker 2, CH2Cl2 dry, r.t., 72 h. Reprinted with permission from *ACS Med. Chem. Lett*. 2020, 11, 5, 664–670. Copyright 2020 American Chemical Society. https://pubs.acs.org/doi/10.1021/acsmedchemlett.9b00538.

Linker **2** was synthesized by a coupling reaction between the α-lipoic acid and 1-(2-hydroxyethyl)piperazine using HOBt and EDC as activating agents. The preparation of **5** was performed applying the one-pot two-step synthetic approach previously developed in our laboratory[50]. The reaction of compound **3** (Si306) with triphosgene generated intermediate **4**, bearing the carbonyl-chloride group on the secondary amine at C4. The displacement of the chlorine using the appropriate alcohol (linker **2**) afforded the final product **5**.

2. PREPARATION OF AUNPS-SI306 NANOSYSTEM

Different methodologies for preparing AuNPs are widely reported in literature[154,155,45,156] and provide the use of different procedures and reagents. Turkevich and Frens method[157] was chosen because of its compatibility with the pyrazolo[3,4-*d*]pyrimidine core (Figure 43; see Materials and Methods for details).

$$HAuCl_4 \cdot 3H_2O + Na_3C_6H_5O_7 \cdot 2H_2O \xrightarrow{H_2O\ milli\text{-}Q} AuNPs$$

FIGURE 43. Preparation of AuNPs.

The procedure used encompassed the use of water as the solvent and trisodium citrate as reducing and stabilizing agent. Furthermore, the selected procedure allowed the preparation of AuNPs with the right size (< 30 nm).

After, the following reaction of functionalization was performed in H_2O: DMSO 90:10 to guarantee the disulfide bridge formation between AuNPs and **5** (Figure 44).

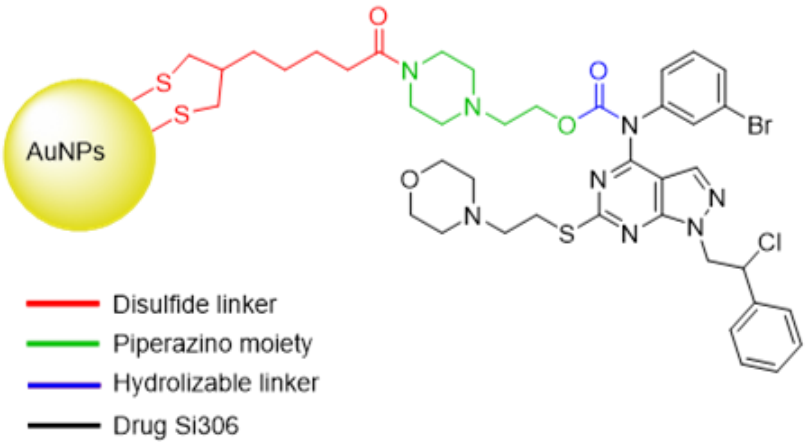

FIGURE 44. Si306-AuNPs nanosystem. Reprinted with permission from *ACS Med. Chem. Lett.* 2020, 11, 5, 664–670. Copyright 2020 American Chemical Society. https://pubs.acs.org/doi/10.1021/acsmedchemlett.9b00538.

3. PURIFICATION AND CHARACTERIZATION OF AUNPS-SI306

To eliminate and quantify the unbound **5**, the AuNPs suspension was ultracentrifuged (BeckMan Coulter Optima L-90 K, see Materials and Methods for details); after three ultracentrifugation cycles, the AuNPs-Si306 pellet was resuspended in water. The concentration of the compound in the supernatant solution was determined by UV/LC-MS and the amount of AuNPs-bound **5** was determined by the difference between the total amount of initial **5** added and the amount of **5** in the supernatants obtained during the purification step. Results showed a good loading efficacy % (LE%) with a value of 65%.

The successful functionalization was further confirmed by spectrophotometric UV-vis analysis (Figure 45): a red shift of about 3 nm[157] of the maximum absorption wavelength between AuNPs (530.78 nm) and AuNPs-Si306 nanosystem (533.01 nm) was recorded. In addition, usually, absorption maximum around 530 nm indicates a nanoparticle size of 40 nm[158].

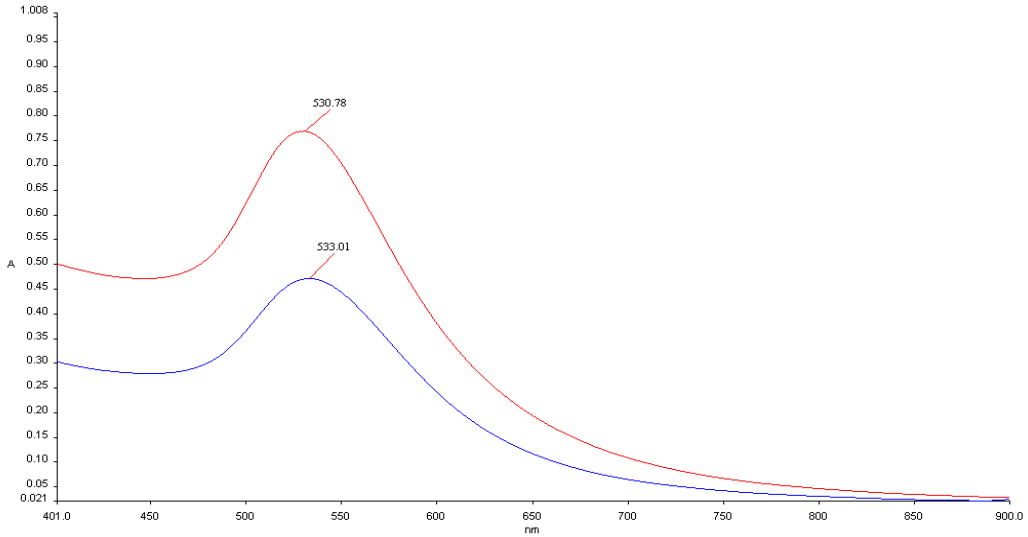

FIGURE 45. Spectrophotometric analysis in the UV-vis range (900-400 nm) of AuNPs (red line) and AuNPs-Si306 nanosystem (blue line). Reprinted with permission from *ACS Med. Chem. Lett*. 2020, 11, 5, 664–670. Copyright 2020 American Chemical Society. https://pubs.acs.org/doi/10.1021/acsmedchemlett.9b00538.

Moreover, the absence of peaks for high wavelengths suggested that no agglomeration of particles takes place in normal conditions.

With the aim to further confirm the successful functionalization of AuNPs by **5**, UV-Vis absorption measurements have been performed for three samples and are reported in Figure 46:

1. the free prodrug (**5**) spectrum which shows a maximum of absorption around 250 nm (Figure 46a);
2. the AuNPs-Si306 nanosystem spectrum which shows an absorption peak attributable to the prodrug (350-250 nm) and an absorption peak attributable to gold nanoparticles (530 nm) (Figure 46b);
3. The AuNPs and **5** were mixed and immediately measured (Figure 46c).

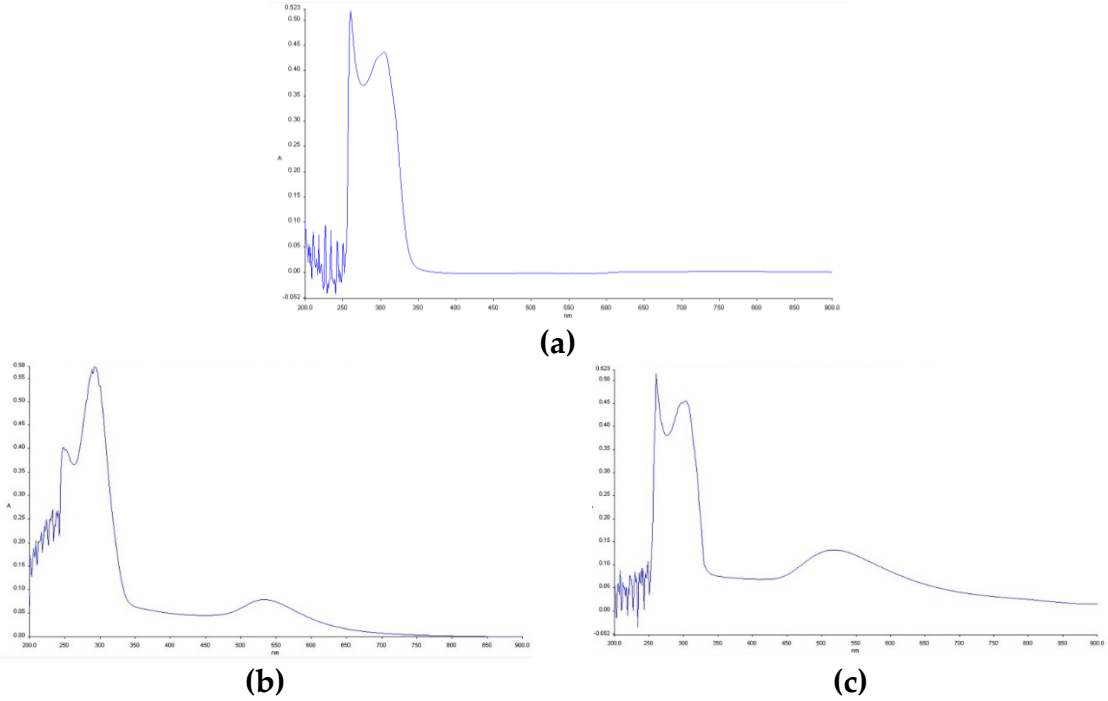

FIGURE 46. UV-vis absorption measurements. **(a)** Free prodrug (**5**) UV-Vis spectrum (concentration 0.012 μg/mL); **(b)** AuNPs-Si306 nanosystem UV-vis spectrum and **(c)** AuNPs and ProSi306 mixed together and immediately measured UV-vis spectrum. Reprinted with permission from *ACS Med. Chem. Lett*. 2020, 11, 5, 664–670. Copyright 2020 American Chemical Society. https://pubs.acs.org/doi/10.1021/acsmedchemlett.9b00538.

When measured as free or immediately after the mix with AuNPs, **5** showed a maximum of absorption around 250 nm. After the functionalization, the maximum of absorption changed to around 300 nm. This is a further confirmation of the successful functionalization of gold nanoparticles by **5**.

3.1 SIZE, Z-POTENTIAL AND PDI

Once determined the LE%, bare AuNPs and AuNPs-Si306 nanosystems were characterized for mean diameter, PDI and ζ-potential by Dynamic Light Scattering (DLS, Zeta Sizer Nano ZS90, Malvern Instruments Ltd, Malvern, UK). Nanoparticles were dispersed in water and measured at 24 °C with a scattering angle of 90°. Particle diameter should be in the 50-70 nm range to enhance the diffusion and transport through the BBB and allow the nanosystem to reach the brain[159], improving tumor penetration and retention[160]. Moreover, this diameter range strengthens the radiosensitization effects of gold nanoparticles[161]. Z-potential is a stability indicator and offers prediction about the tendency of nanoparticles to form aggregates over time: values greater than +25 mV or less than -25 mV are considered to be ideal[162].

TABLE 18. DLS Characterization of AuNPs-Si306 and bare AuNPs. Mean values ± S.D. calculated from three independent experiments (n=3).

Sample	Z-pot. (mV)[a]	Size (nm)[a]	PDI[a]
AuNPs-Si306	-43.9 ± 0.4	48.6 ± 1.3	0.441 ± 0.02
Bare AuNPs	-41.5 ± 1.1	41.8 ± 0.9	0.637 ± 0.05

[a]Measured by DLS (Dynamic Light Scattering).

DLS measurements showed optimal results for AuNPs-Si306 nanosystem, with no remarkable differences with bare AuNPs and revealing size and ζ-potential values of 48.6 nm and -43.9 mV, respectively. Moreover, the PDI value of 0.441 demonstrated a relatively monodispersed particle population (Table 18). These results suggest that the obtained nanosystem could represent a promising anti-GBM platform, especially in association with RT[163,164,165].

3.2 Stability Evaluation of AuNPs-Si306 in Salts and Protein Solutions

To probe the nanoparticles agglomeration state in presence of salts and proteins, UV-Vis spectra have been recorded upon the addition of NaCl or KCl (0.01-0.1 M concentration range, Table 19 and 20) or human serum albumin (HSA, 12.5, 25, 50 mg/mL, Table 21) to the AuNPs suspension. HSA and salts at lower concentrations did not affect the stability of AuNPs and no agglomeration took place. On the other hand, AuNPs showed a visible color change from red to blue upon addition of salts at higher concentrations, due to the formation of aggregates, highlighted also by a red-shift and broadening of the band.

TABLE 19. Time-resolved UV-Vis spectra of NaCl upon interaction with AuNPs and picture of the NaCl-AuNPs mixture immediately after salt addition. Reprinted with permission from *ACS Med. Chem. Lett.* 2020, 11, 5, 664–670. Copyright 2020 American Chemical Society. https://pubs.acs.org/doi/10.1021/acsmedchemlett.9b00538.

Final concentration	**AuNPs + NaCl spectra** AuNPs (Blue); AuNPs + NaCl after 1 min (Red); AuNPs/NaCl after 5 min (Green); AuNPs/NaCl after 10 min (Pink)	Aspect immediately after salt addition
NaCl 0.01 M	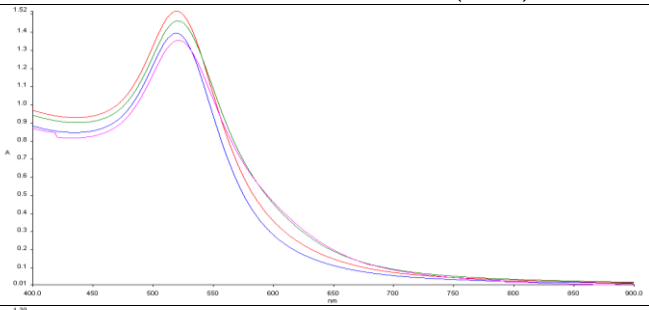	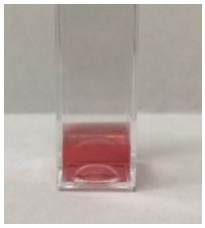
NaCl 0.05 M	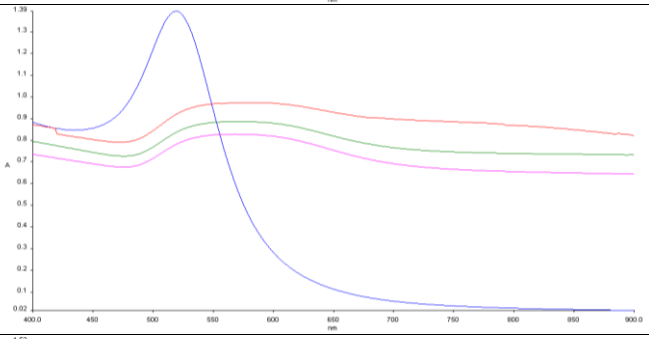	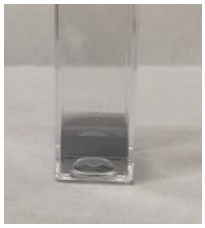
NaCl 0.07 M	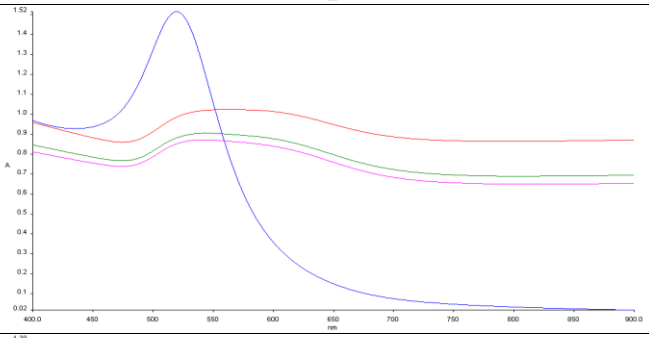	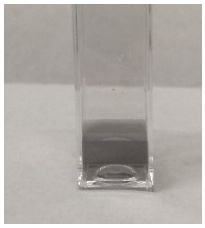
NaCl 0.1 M	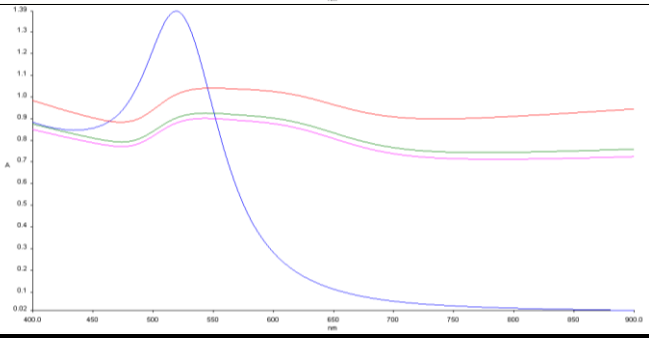	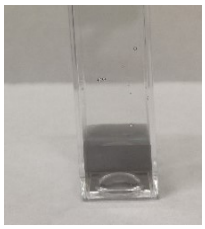

TABLE 20. Time-resolved UV-vis spectra of KCl upon interaction with AuNPs and picture of the KCl-AuNPs mixture immediately after salt addition. Reprinted with permission from *ACS Med. Chem. Lett*. 2020, 11, 5, 664–670. Copyright 2020 American Chemical Society. https://pubs.acs.org/doi/10.1021/acsmedchemlett.9b00538.

KCl final concentration	**AuNPs + KCl spectra** AuNPs (Blue); AuNPs + KCl after 1 min (Red); AuNPs + KCl after 5 min (Green); AuNPs + KCl after 10 min (Pink)	Aspect immediately after salt addition
KCl 0.01 M	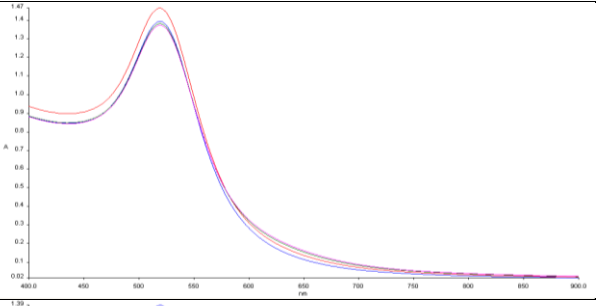	
KCl 0.05 M	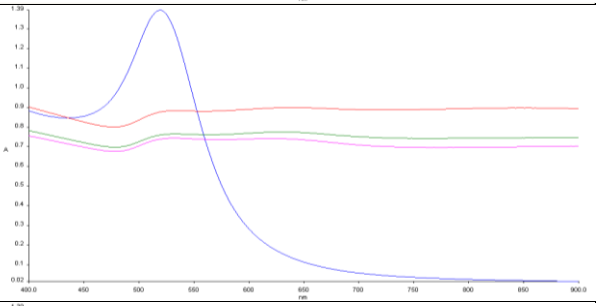	
KCl 0.07 M	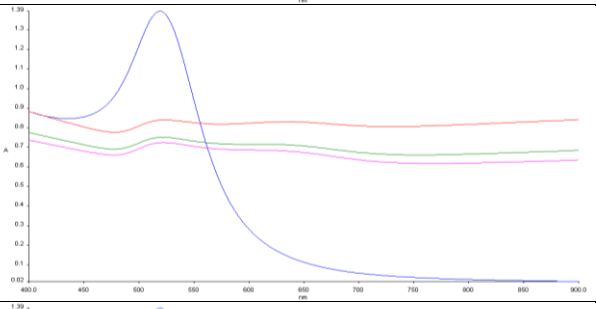	
KCl 0.1 M	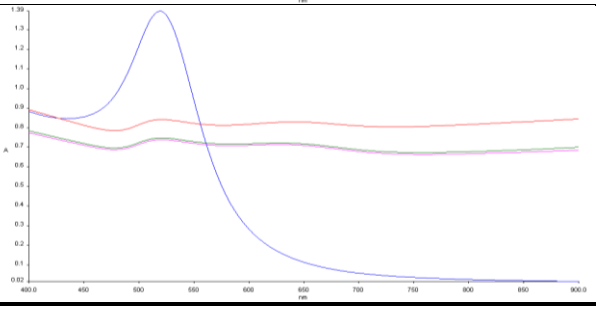	

TABLE 21. Time-resolved UV-vis spectra of HSA upon interaction with AuNPs. Reprinted with permission from *ACS Med. Chem. Lett*. 2020, 11, 5, 664–670. Copyright 2020 American Chemical Society. https://pubs.acs.org/doi/10.1021/acsmedchemlett.9b00538.

AuNPs + HSA Spectra

HSA final conc.	AuNPs (Blue); AuNPs + HSA immediantly (Red); AuNPs + HSA after: 10 min (Green), AuNPs + HSA 20 min (Pink), AuNPs + HSA 40 min (Aquamarine) AuNPs + HSA 60 min (Bordeaux).
12.5 mg/mL	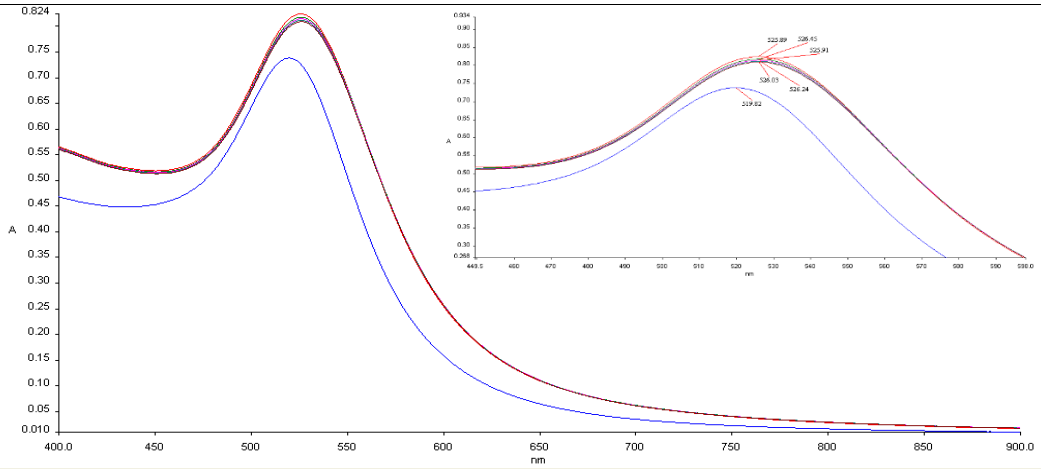
25 mg/mL	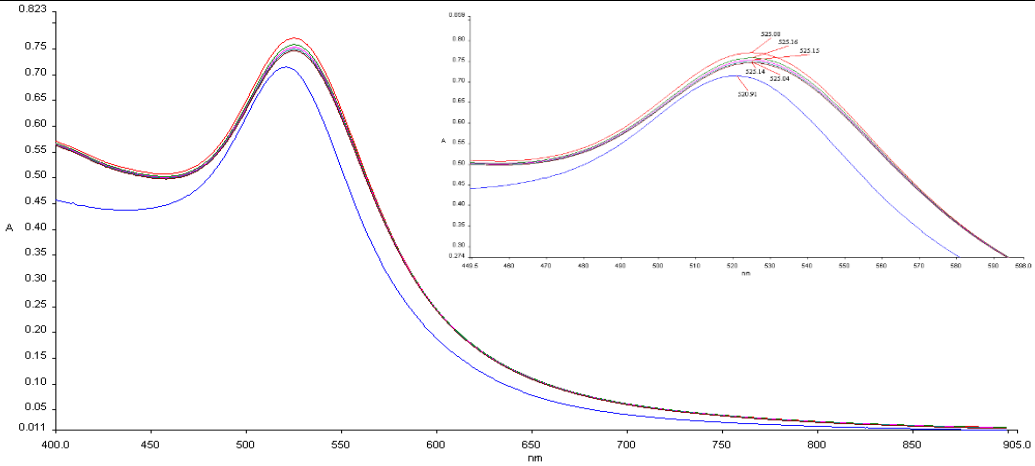
50 mg/mL	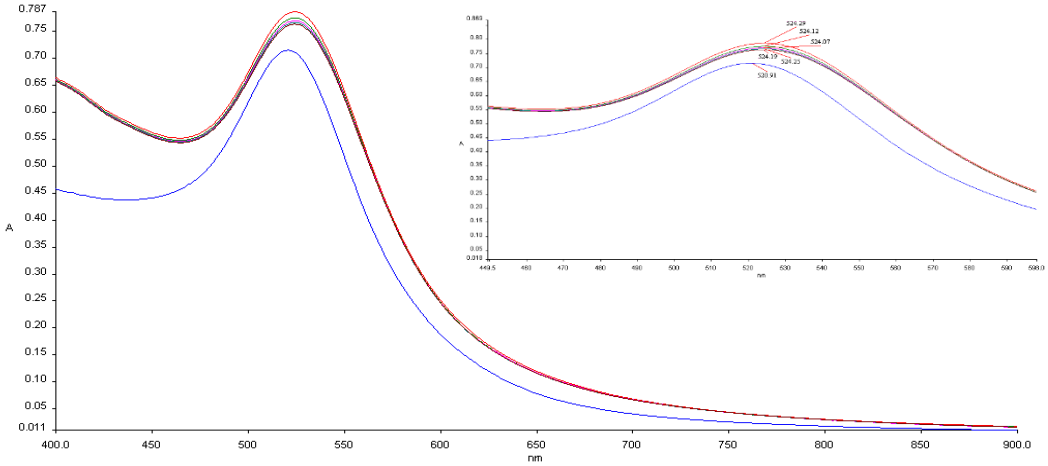

3.3 STABILITY IN POLAR MEDIA AND HUMAN PLASMA

To avoid potential side effects as well as guaranteeing the highest efficacy, the active compound Si306 should be released from AuNPs-Si306 nanosystem. In order to investigate this aspect, the rate of plasma hydrolysis was evaluated *in vitro*. First, stability in polar media such as H_2O, ACN, methanol, DMSO and PBS was evaluated by UV/LC-MS. The determined half-lives ($t_{1/2}$) resulted to be greater than 48h, confirming good stability of AuNPs-Si306 nanosystem. This good stability allowed running the subsequent studies. The nanosystem was then incubated in human plasma at 37°C and the release rate of Si306 was monitored by UV/LC-MS at different time points over 24 hours. As expected, good plasma hydrolysis of the carbamate-linker after 24 hours was found (76%), indicating the release of the antitumor compound by plasma esterases via enzymatic hydrolysis.

4. *IN VITRO* CYTOTOXICITY ASSAY

The antiproliferative effects of AuNPs-Si306 nanosystem, the respective not functionalized AuNPs, and free Si306 dissolved in DMSO evaluated alone (orange bars) and in combination with RT (blue bars) at two different final concentrations of Si306 (1 and 10 μM) by cell low density growth assay using U87 GBM cell line[166] has been shown in Figure 47.

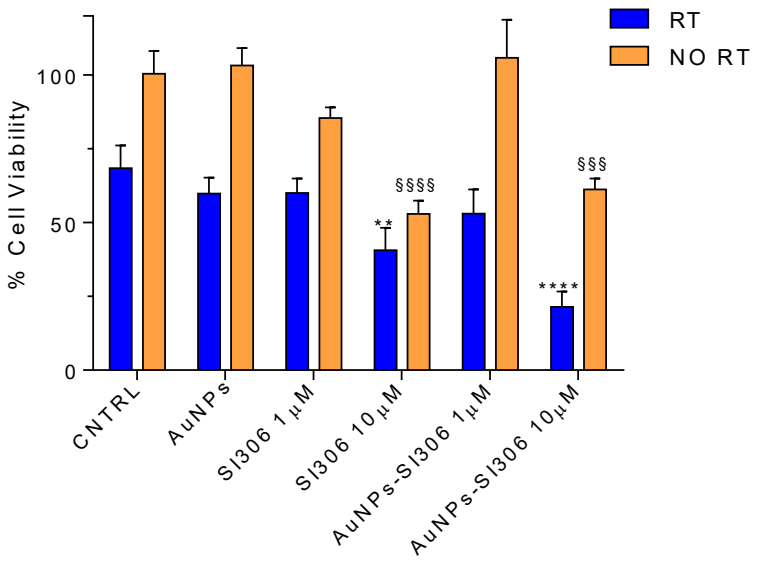

FIGURE 47. The *in vitro* antiproliferative effect of AuNPs, Si306 and AuNPs-Si306 nanosystem. Results are expressed as percentage mean ± S.D. (n=3). A Bonferroni's one-way multiple comparisons test (ANOVA) was performed to test the significance of the observed differences. *indicates statistically significant differences in group "RT" (blue bars) vs CNTRL RT (**p<0.01, ****p<0.0001); § indicates statistically significant differences in group "NO RT" (orange bars) vs CNTRL NO RT (§§§p<0.001, §§§§p<0.0001). Reprinted with permission from *ACS Med. Chem. Lett*. 2020, 11, 5, 664–670. Copyright 2020 American Chemical Society. https://pubs.acs.org/doi/10.1021/acsmedchemlett.9b00538.

In table 22, reduction in cell viability % in respect to corresponding control (vehicle associated or not with RT, CNTRL) has been reported for all the tested formulations. As expected, not functionalized AuNPs, when not associated with RT, did not provoke any mortality in cells, proving to be safe. Besides, not irradiated cell growth was inhibited exclusively by free Si306 (10 μM) and AuNPs-Si306 (10 μM).

TABLE 22. Mean reduction % in cell viability ± S.D. in respect to corresponding CNTRL (RT or NO RT).

Samples	RT	NO RT
AuNPs	12.60 ± 7.88	0
Si306 1 μM	12.35 ± 7.23	14.96 ± 3.60
Si306 10 μM	40.62 ± 11.07	47.32 ± 4.47
AuNPs-Si306 1 μM	22.57 ± 12.07 ##	0
AuNPs-Si306 10 μM	68.65 ± 7.51 ###	39.02 ± 3.68

Bonferroni's one-way multiple comparisons test (ANOVA) was performed. Values marked with asterisks represent significantly different between RT and NO RT in the row (## $p<0.01$; ### $p<0.001$).

However, since not functionalized AuNPs did not show any effect, it is likely that the inhibitory activity of AuNPs- Si306 is due to Si306 portion and not to AuNPs system. On the other hand, when combined with RT, not functionalized AuNPs was able to slightly reduce the proliferation of U87 cells in respect to its corresponding control (about 13% of reduction). Free Si306 has been proved to be active in reducing GBM cell viability but RT did not enhance its antiproliferative effect. Indeed, from statistical analysis, reported in Table 22, significant differences between free Si306 with or without RT have not been observed for both the concentrations 1 μM (12 and 15%, respectively) and 10 μM (40 and 47%, respectively). However, the highest antiproliferative effect was achieved by the combination treatment with AuNPs-Si306 (10 μM) and RT. This combination resulted in a significant decrease in the number of viable cells of about 70% in respect to RT alone.

DISCUSSION AND CONCLUSIONS

In conclusion, in this work, we have reported the design, preparation and characterization of AuNPs-Si306 nanosystem as a novel potential anticancer agent toward GBM. AuNPs were prepared using the Turkevich and Frens method, while key compound **5** was synthesized in good yield exploiting a one-pot two-step approach developed in our laboratories.

The functionalization of AuNPs with compound **5** was achieved (qualitatively confirmed by spectrophotometric analysis) with a 65% loading efficacy (quantitively confirmed by UV/LC-MS analysis) after the disulfide bridge formation between gold nanoparticles and **5**. The characterization of the nanosystem showed optimal stability and morphology profile: $t_{1/2}$ in polar media greater of 48 h, release of 76% of the active compound Si306 when incubated with human plasma, ζ-potential of -43.9 mV, nanoparticle diameter of 48.6 nm and 0.441 PDI value. Moreover, biological assay with U87 cell line has proved an effective antiproliferative activity of the association between AuNPs-Si306 nanosystem and RT that resulted significantly higher than the effect of Si306, AuNPs and RT alone.

Taken together, the results described in this work reflect the promising properties of the molecule Si306 when developed as AuNPs nanosystem toward GBM. This strategy might allow, not only to exploit the synergy of RT with both gold platform and the pyrazolo[3,4-*d*]pyrimidine compound but also to overcome problems related to tumor localization and pharmacokinetic issues related to the poor solubility of Si306.

These results offer a promising rationale for further development of AuNPs-Si306 nanosystem and experimental confirmation in different cancer models.

MATERIALS AND METHODS

1. DRUGS AND MATERIALS

All commercially available chemicals and solvents were used as purchased from Sigma Aldrich Srl (Milan, Italy). The human plasma for plasma stability was obtained by volunteers' donors. Milli-Q quality water (Millipore, Milford, MA, USA) was used. Synthesis and characterization of Si306 were previously reported[49].

2. SYNTHESIS OF AUNPS

To a solution of $HAuCl_4 \cdot 3H_2O$ (7.88 mg, 0.02 mmol) in 20.00 mL of H_2O Milli-Q heated upon boiling, was added a solution of sodium citrate dehydrate 1% prepared with 2.00 mL of H_2O Milli-Q (19.97 mg, 0.0679 mmol). The reaction mixture was stirred until the appearance of red color. The resulting solution was cooled at room temperature and stored in the dark.

3. FUNCTIONALIZATION OF AUNPS

2.79 mL of AuNPs was diluted with 8.00 mL of H_2O Milli-Q. A solution of **5** (3.00 mg, 0.0033 mol) solubilized in 0.20 mL of DMSO and diluted with 2.00 mL of H_2O Milli-Q was added dropwise to obtain a dark pink solution. The solution was stirred at room temperature for 8 hours. After, the solution was stored in the dark.

4. DRUG FUNCTIONALIZATION EFFICACY AND PURIFICATION

To determine the loading efficacy (LE%) of Si306 for AuNPs and to remove the unreacted compound, the AuNPs-Si306 suspension was ultracentrifuged by three repeated cycles at 13.000 rpm for 90 min at 24 °C each (BeckMan Coulter Optima L-90 K). Washing waters (H_2O: DMSO 1.5:2 v/v) were collected at the end of each cycle for the UV/LC-MS determination of free Si306. Finally, after the third ultracentrifugation cycle, the AuNPs-Si306 pellet was resuspended in water.

LE% was calculated with the following Equation:

$$\text{LE\%} = \frac{\text{Amount of total drug} - \text{ Amount of drug in the supernatant}}{\text{Amount of total drug}} \cdot 100$$

The experiments were repeated in triplicate and results compared with the standard curve.

5. DLS MEASUREMENTS

Mean particle size, polydispersity index (PDI) and ζ-potential were determined by Dynamic Light Scattering (DLS) (Zeta Sizer Nano ZS90, Malvern Instruments Ltd, Malvern, UK). AuNPs-SI306 nanosystem was diluted in water to give an optical density (OD) of 0.1 unit of absorbance at 420 nm and then measured at 24° C with a scattering angle of 90°. Z-potential measurements were carried out using folded capillary cells (Malvern). Results are expressed as mean values ± S.D. calculated from three independent experiments (n=3).

6. INTERACTION OF AUNPS WITH SALTS AND HSA

The interaction of AuNPs versus salts (NaCl and KCl) and proteins (HSA, human serum albumin) and the state of nanoparticle aggregation have been investigated by UV-Vis absorption measurements performed by UV-VISIBLE spectrophotometer Lambda 2 (Perkin Elmer).

AuNPs suspension (200 μL) was added with:

- Salt solution 0.02 M, 200 μL (final concentration 0.01 M)
- Salt solution 0.1 M, 200 μL (final concentration 0.05 M)
- Salt solution 0.14 M, 200 μL (final concentration 0.07 M)
- Salt solution 0.2 M, 200 μL (final concentration 0.1 M)

For each mixture, the UV-Vis absorption was measured at 1, 5, 10 minutes.

Regarding the evaluation of the interaction with HSA, AuNPs suspension (200 μL) was added with:

- HSA solution 25 mg/mL, 200 μL (final concentration 12.5 mg/mL)
- HSA solution 50 mg/mL, 200 μL (final concentration 25 mg/mL)
- HSA solution 100 mg/mL, 200 μL (final concentration 50 mg/mL)

For each mixture, the UV-Vis absorption was measured immediately, at 10, 20, 40, 60 minutes.

7. Stability in Polar Media and Human Plasma

AuNPs-Si306 nanosystem was dissolved at room temperature in H_2O, ACN, methanol, DMSO, or phosphate buffer (25 mM, pH 7.4) up to a final concentration of Si306 equal to 100 μM. Aliquot samples (20 μL) were taken at fixed time points (0.25, 0.50, 0.75, 1.0, 2.0, 3.0, 4.0, 5.0, 6.0, 7.0, 8.0, 24.0 and 48 h), ultracentrifuged (BeckMan Coulter Optima L-90 K, 13000 rpm for 90 min at 25 °C) and the supernatant was analyzed by UV/LC-MS. The experiments were repeated in triplicate and results were compared with the standard curve.

Pooled human plasma (1.50 mL, 55.70 μg protein/mL), phosphate buffer (1.40 mL, pH 7.4, 25 mM), and a solution of AuNPs-Si306 nanosystem (100 μL, Si306 3.0 mM) were mixed in a test tube that was incubated at 37 °C. At set time points (0.25, 0.50, 1.0, 3.0, 7.0, and 24.0 h), samples of 150 μL were taken, mixed with 600 μL of cold acetonitrile and ultracentrifuged (BeckMan Coulter Optima L-90 K, 13000 rpm for 90 min at 25 °C). The supernatant was removed and analyzed by UV/LC-MS to monitor the hydrolysis process. The experiments were repeated in triplicate and results were compared with the standard curve.

8. Statistical Analysis

Bonferroni's Multiple Comparison Test (One-way ANOVA) was performed by Software GraphPad Prism 6.0.

SECTION 3

TYROSINE KINASE INHIBITOR Si409 HAS *IN VITRO* AND *IN VIVO* ANTI-TUMOR ACTIVITY AGAINST DIFFUSE LARGE B-CELL LYMPHOMA

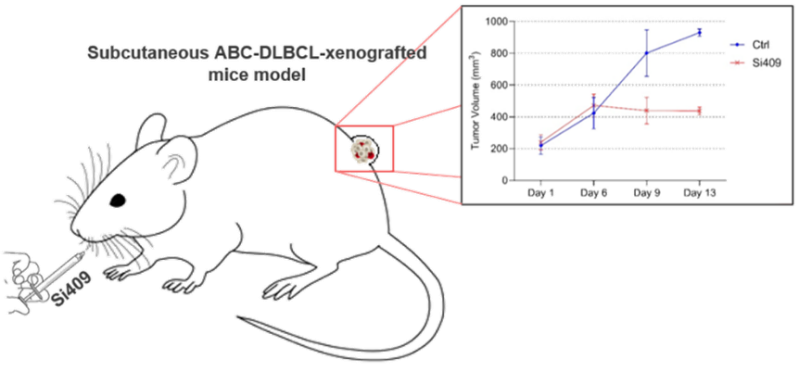

AIM OF THE PROJECT

The abnormal activation of Src family kinases (SFKs), due to the deregulation of the B-cell receptor (BCR) signaling pathway, in diffuse large B-cell lymphoma (DLBCL) represents a promising target for the development of a novel pharmacological strategy to overcome the ibrutinib-resistance. Data reported with the two SFK inhibitors dasatinib and masitinib suggest the possibility to overcome these resistances. The reason of the anti-tumor activities observed with dasatinib and masitinib may reside in the role of SFKs, such as the specific lymphocyte protein kinase Lyn, Blk, and Fyn, as effectors of BCR-triggered multi-enzymatic cascade. Hence, the inhibition of these SFKs would represent a rational pharmacological target in the treatment of different DLBCL subtypes. In this context, tyrosine kinase inhibitors, pyrazolo[3,4-*d*]pyrimidine derivatives showed antiproliferative activity in several ibrutinib-resistant lymphoma cell lines. Among these derivatives, Si409 emerged for its favorable aqueous solubility (134.2 μg/mL) and high *in vitro* metabolic stability (99.4 %). The low Ki value for c-Src (300 nM) and the ligand-site similarity in key SFK members involved in BCR lymphoma pathways, such as Fyn, Lyn, and Blk, prompted us to further investigate the role of Si409 as anti-lymphoma agent. In this regard, preclinical toxicity profile, *in vivo* pharmacokinetic properties, and therapeutic efficacy in the subcutaneous murine DLBCL model will be evaluated in order to fully characterize the promising role of Si409 as anticancer agent for the treatment of DLBCL.

RESULTS

1. *IN VITRO* KINASE INHIBITION ASSAY

The inhibitory activity of Si409 was first analyzed against several SFKs involved in BCR signaling pathway of DLBCL (Table 23). An important enzymatic inhibition of Fyn was observed obtaining Ki value equal to 0.18 μM, in contrast to Lyn and Blk for which Ki values above 1 μM were obtained. Moreover, significant enzymatic inhibition of c-Src was observed with Ki value of 0.30 μM[47].

TABLE 23. Inhibitory constant (Ki) values of Si409 against c-Src, Fyn, Lyn and Blk.

Target	Ki ± S.D. (μM)[a]
c-Src	0.30 ± 0.04
Fyn	0.18 ± 0.03
Lyn	1.17 ± 0.50
Blk	11.97 ± 3.35

[a]Values are the mean of at least two independent experiments.

2. CELL VIABILITY ASSAY

Antiproliferative activity on different lymphoma cell lines derived from both ABC- and GCB-DLBCL and expressing these SFKs members was assessed (Table 24). Si409 showed concentration-dependent antitumor activity in all cell lines analyzed with a median IC_{50} value of 1.70 μM (95% CI, 0.30 - 2.50 μM), and no significant difference between GCB- and ABC-DLBCL lines. Besides, low cytotoxic activity of Si409 (IC_{50} = 52 μM) was measured on healthy human peripheral blood mononuclear cells (PBMCs), revealing a selectivity index of over 25-fold as calculated in comparison with SU-DHL10 cells.

TABLE 24. *In vitro* cytotoxicity activity on DLBCL cell lines (IC_{50} values after 72h of incubation).

Cell line	IC_{50} ± S.D. (μM)[a]
U2932[b]	2.50 ± 0.13
SU-DHL2[b]	2.50 ± 0.13
TMD8[b]	0.90 ± 0.05
WSU-DLCL2[c]	1.50 ± 0.08
VAL[c]	2.50 ± 0.12
SU-DHL10[c]	0.30 ± 0.02
PBMCs[d]	51.80 ± 4.70

[a]Values are the mean of at least three independent experiments; [b]ABC-DLBCL cell line; [c]GCB-DLBCL cell lines; [d]PBMCs, peripheral blood mononuclear cells from healthy individuals.

3. Effect of Si409 on hERG Current

Considering the potential hERG liability for several tyrosine kinase inhibitors[167,168], the effect of Si409 on hERG currents recorded in hERG-HEK293 recombinant cells was investigated by using the patch-clamp technique. Disruption of hERG channel can result in long QT syndrome and the fatal arrhythmia Torsades de Pointes. Thus, identifying the potential hERG channel off-target interaction is an essential step during the early stages of drug discovery[169]. Si409 induced a significant reduction of hERG current but only at concentrations at least 10-fold higher than the median IC_{50} value recorded in tumoral cell lines, thus proving to be reasonably safe at the latter concentration (Figure 48).

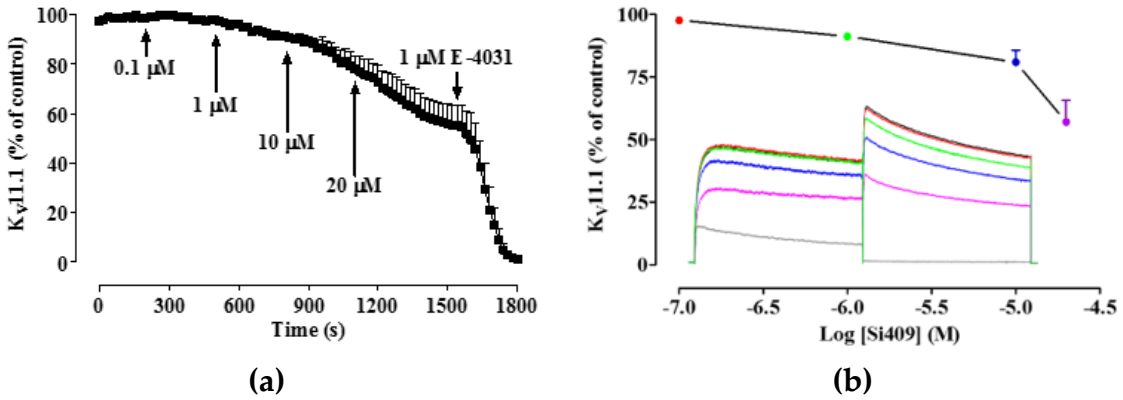

(a) **(b)**

Figure 48. (a) Time course of hERG current (KV11.1) inhibition induced by cumulative concentrations of Si409. The drug was applied at the time indicated by the arrows, and peak tail currents were recorded and subsequently normalized according to the current recorded just prior to Si409 addition. E-4031 (1 μM) suppressed current amplitude. Data points are the mean ± SEM (n=3). **(b)** Concentration-dependent inhibition by Si409 of hERG tail currents. On the ordinate scale, current amplitude is reported as percentage of that recorded prior to the addition of the first concentration of the drug. Data are mean ± S.E.M. (n=3). Inset: Average traces (recorded from 3 cells) of hERG channel currents measured in hERG-HEK293 cells under control conditions (black trace) and after the addition of cumulative concentrations (μM) of Si409. The effect of the specific blocker E-4031 (1 μM; grey trace) is also shown. Current was elicited from a Vh of -80 mV with a step to 20 mV (4 s), followed by a return to -50 mV (4 s) to elicit the tail current. This protocol was repeated every 20 s.

4. *IN VIVO* PHARMACOKINETIC STUDIES

A proof-of-concept PK study was designed to give preliminary indications of Si409's *in vivo* fate. In this regard, healthy BALB/C mice were treated intravenously with Si409 at a single dose of 25 mg/kg and sacrificed at defined time points. The plasma analyses revealed the presence of Si409 and a metabolite that was characterized as glucuronic acid conjugate by mass spectrometry studies (See Paragraph 5. for more details). After i.v. administration, the compound did not reach maximum plasma concentrations due to the metabolic transformation into its glucuronic acid conjugate, which was rapidly excreted (Figure 49a). Nevertheless, it was possible to calculate the pharmacokinetic parameters of Si409 showing a $t_{1/2}$ value of 3.12 h and a C_{max} of 12.13 ug/mL (Table 25). Based on these observations, it was decided to carry out further PK studies at an eight-fold higher dosage (200 mg/kg). For this dosage, the oral route was chosen because Si409 has poor water solubility at high concentration and a suitable formulation for intravenous use was more difficult to obtain. As expected, even for oral administration of Si409 an acute metabolism led to low plasma concentrations (Figure 49b) of the drug (C_{max} equal to 0.68 µg/mL), with a half-life of 10.25 h (Table 25).

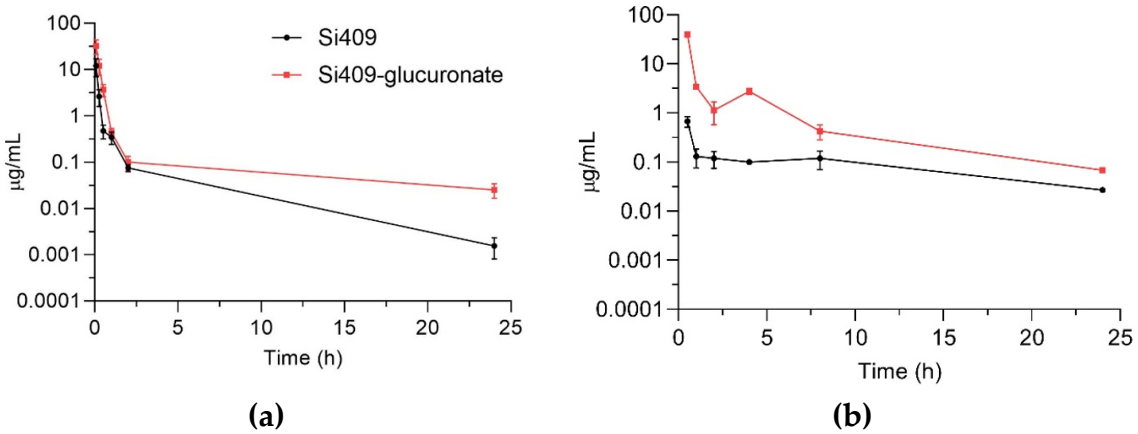

FIGURE 49. Si409 *in vivo* pharmacokinetic profile in healthy mice. **(a)** Plasma concentration-time curves of Si409 and its metabolite (mean ± S.E.M.) during 24 h after i.v. injection (25 mg/kg, n=2) and **(b)** oral by gavage (200mg/kg, n=5). The plasma concentration in the y-axis is expressed as log10 scale.

In addition, the MRT value is more than 10-fold higher than that observed intravenously. This indicates that, following absorption of Si409 at the

gastrointestinal tract, the amount of compound in the circulatory bloodstream is eliminated more slowly than by intravenous administration, although it cannot achieve high plasma concentration values.

TABLE 25. The plasma pharmacokinetic parameters were calculated by non-compartmental analysis using PKSolver software.

Parameters	Unit	Si409	
		Intravenous	*Per os*
Dose	mg/kg	**25**	**200**
$t_{1/2}$[a]	h	3.12	10.25
T_{max}[b]	h	0.08	0.50
C_{max}[c]	µg/mL	12.13	0.68
$AUC_{0\rightarrow 24h}$[d]	µg /mL·h	4.39	2.33
$AUC_{0\rightarrow \infty}$[e]	µg /mL·h	4.39	2.73
$MRT_{0\rightarrow \infty}$[f]	h	0.67	11.75
V_z[g]	L/Kg	25.64	1084.89
CL[h]	L/h/Kg	5.69	73.34

[a]Elimination half-life, [b]time of maximum plasma concentration, [c]maximum plasma concentration, [d]area under the plasma concentration versus time curve, [e]area under the plasma concentration versus time curve extrapolated to infinity, [f]mean residence time, [g]apparent volume of distribution during the terminal phase, [h]clearance.

Results of liver distribution, after oral administration, showed the presence of Si409 which is converted/eliminated already after 30 minutes and therefore decreased during the 24 h (Figure 50). On the contrary, the presence of the glucuronate increased over time and reached the maximum concentration after 4 h. Subsequently, the metabolite was eliminated and almost disappeared at 24 h.

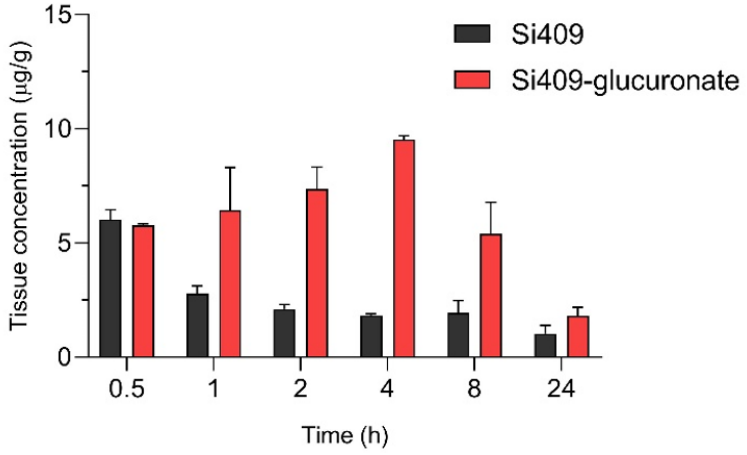

FIGURE 50. Hepatic distribution of Si409 and its metabolite (mean ± S.E.M., n=5) after oral administration (200 mg/kg).

Moreover, it is interesting to note that all treated animals survived during the experiments until the final sacrifice at 24 h, suggesting no systemic toxicity after both oral and i.v. administration of a single exposure to Si409.

5. UV/LC-MS AND MS/MS CHARACTERIZATION OF Si409-GLUCURONATE

UV/LC-MS analysis performed on plasma samples revealed the presence of a metabolite of Si409 with extract ion signal corresponding to the pseudo-molecular ion of 581 m/z (Figure 51 and 52). This suggests that Si409 underwent phase II metabolism in particular, the compound was involved in a glucuronidation reaction mediated by UDP-glucuronosyltransferase (UGT) which catalyzes the addition of glucuronic acid moiety (MW: 194.13 g/mol) at one of the two -OH groups present.

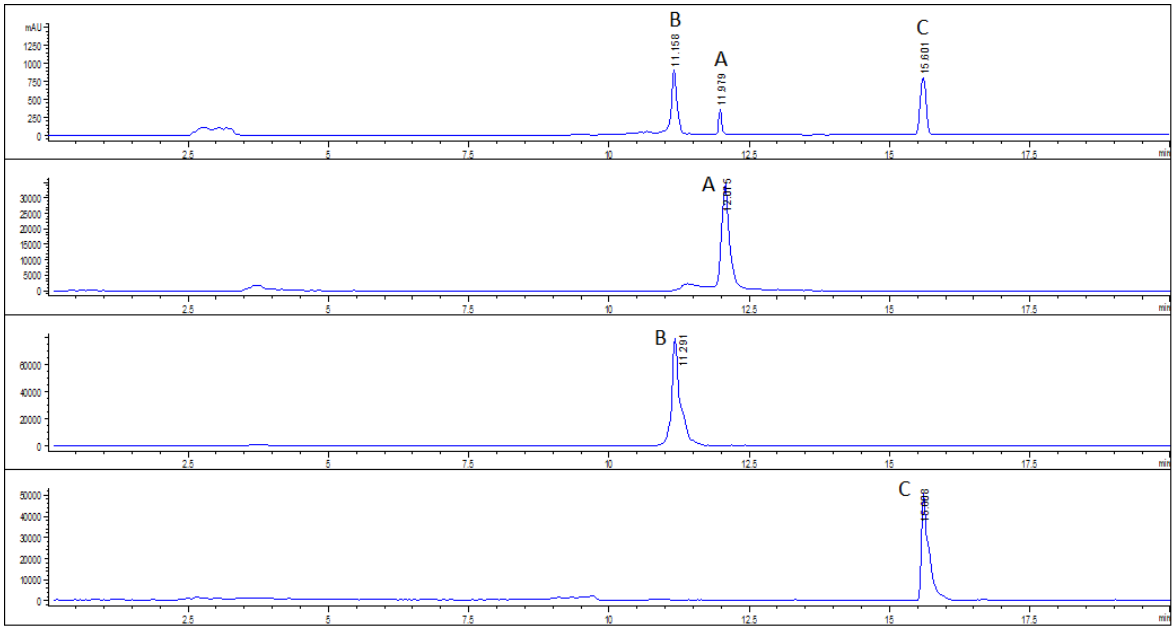

FIGURE 51. Chromatographic analysis of a mouse plasma extract; UV trace of Si409 (A), Si409-glucuronate (B) and Si34 used as internal standard (C) with extract ion signals corresponding to the pseudo-molecular ions (m/z: 405, 581 and 410, respectively).

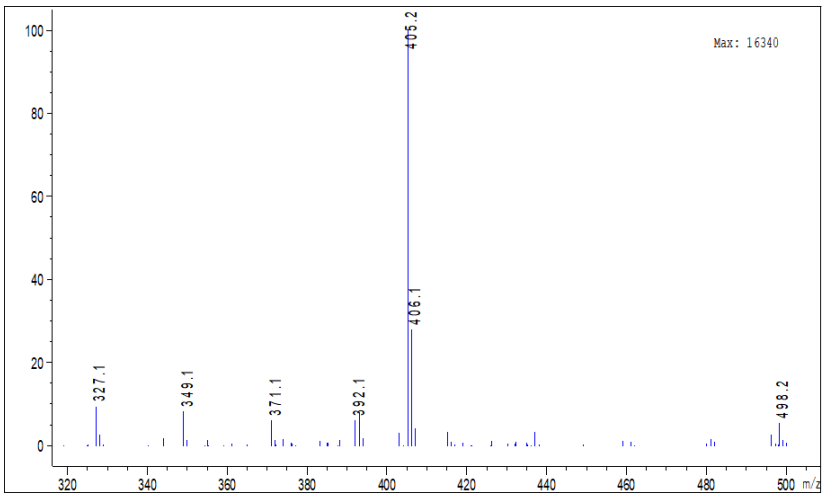

(a)

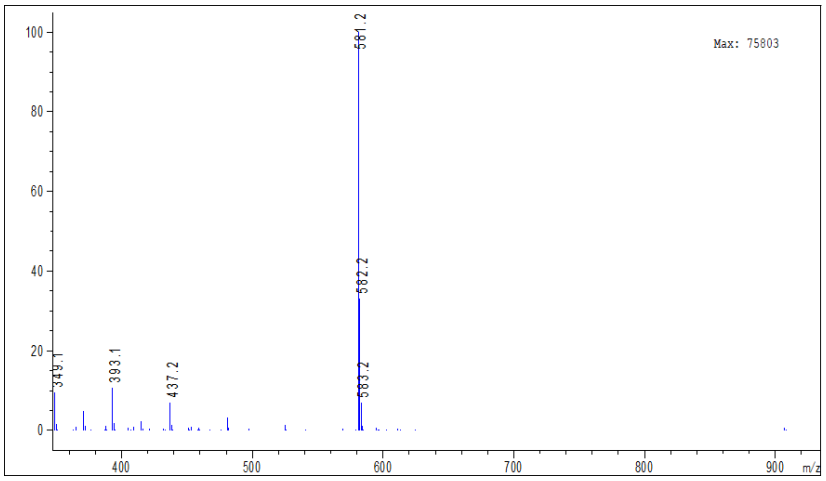

(b)

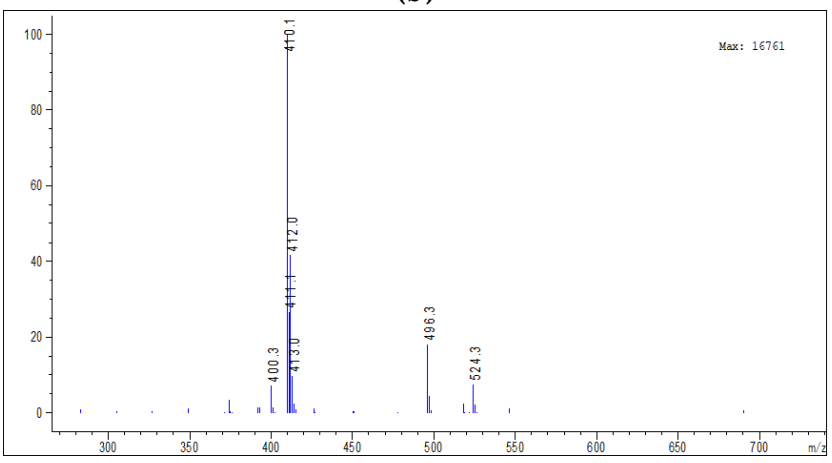

(c)

FIGURE 52. Mass spectra obtained after chromatographic separation with a single quadrupole detector of **(a)** Si409, **(b)** Si409-glucuronate and **(c)** internal standard Si34. Ionization was performed in positive mode.

To confirm the position in which conjugation with glucuronic acid occurred, MS/MS analysis was performed. Si409-glucuronate was ionized and fragmented by LC-MS/MS with progressively higher collision energy (from -10 V to -50 V) to produce spectra that were used for its identification and characterization. The optimal

collision energy was -25 V. In Figure 53, a schematic representation of the Si409 (A) and its metabolite Si409-glucuronate (B) sites that undergo MS/MS fragmentation, and the MS spectra are shown (collision energy equal to -25 V). Based on the analysis of the content of the spectra and fragments obtained, it is believed that the glucuronidation reaction on Si409 occurs on the phenolic portion.

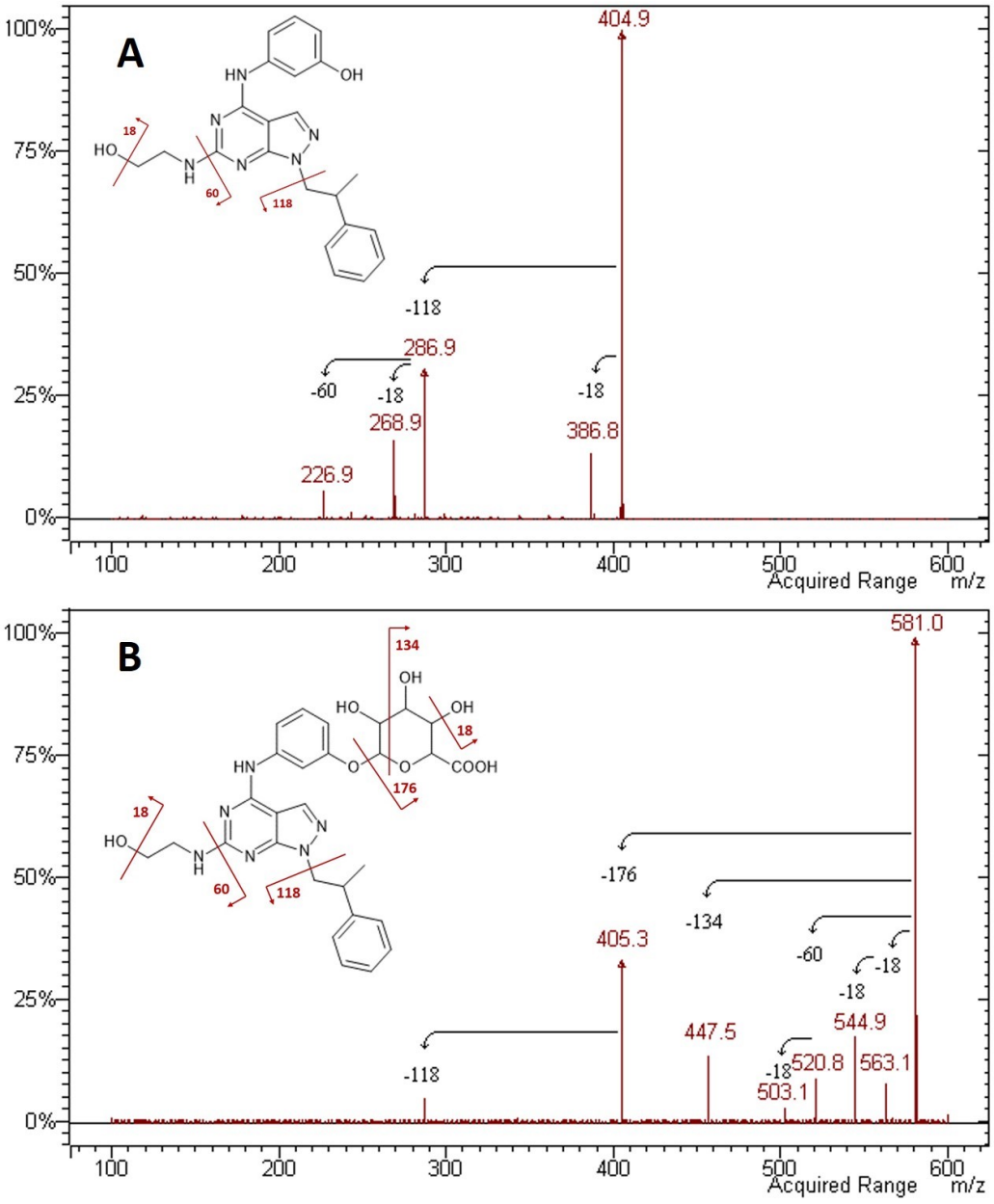

FIGURE 53. MS/MS spectra obtained in the MS/MS fragmentation experiments (collision energy -25 V). **(A)** Si409 and **(B)** Si409-glucuronate.

6. *IN VIVO* EFFICACY ON ABC-DLBCL MICE MODEL

Despite the PK results obtained, to prove that Si409 could be considered a good drug candidate, *in vivo* study on ABC-DLBCL xenograft model was performed. Mice inoculated subcutaneously with the ABC-DLBCL TMD8 cell line were divided into two groups (ten animals for each group) as soon as the average volume of 220-240 mm^3 was reached. Treatment started with Si409 (200 mg/kg *per os*, 5 days/week) or with vehicle only (30% PEG_{400} in water) on day 1. The treatment significantly delayed tumor growth ($p < 0.05$) starting from day 6 (Figure 54). At the end point, mice treated with Si409 had tumor masses up to two-fold smaller than vehicle-treated controls. Also, the administration of Si409 did not cause any loss of body weight or any other signs of suffering.

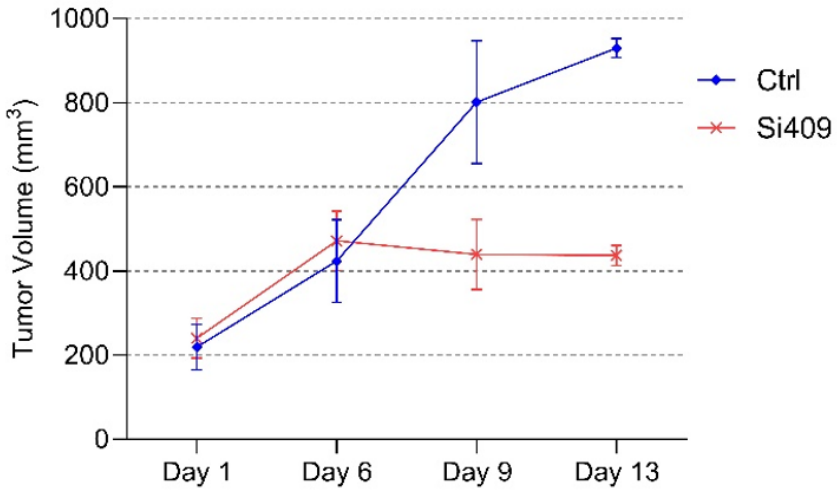

FIGURE 54. Si409 *in vivo* anti-lymphoma activity in subcutaneous ABC-DLBCL-xenografted mice model. Tumor volume reduction evaluated on TMD8 model after oral administration of Si409 at the dosage of 200 mg/kg (mean ± S.E.M., n=10).

DISCUSSION AND CONCLUSIONS

Recent works have shown the possibility of using dasatinib and other similar TKIs in DLBCL cases with primary resistance to the BTK inhibitor ibrutinib[80,170]. Here, we have analyzed several pharmacological properties of the pyrazolo[3,4-*d*]pyrimidine Si409 as a drug candidate for DLBCL. Si409 presented sub-micromolar Ki values against Src and Fyn kinases, and anti-lymphoma activity at low- and sub-micromolar concentrations, in both GCB- and ABC-DLBCL lines. The *in vitro* activity of Si409 in both DLBCL main subtypes was comparable or even higher to that reported for dasatinib and masitinib[80,170]. Moreover, important safety parameters were gathered from cytotoxicity assays performed on PBMCs and from hERG channel recordings, discriminating factors in the development of TKIs. PK studies showed high phase II metabolism caused by glucuronide conjugation, which reduces plasma levels and increases the clearance of Si409. Despite the low plasma levels, the treatment with Si409 of an ABC-DLBCL xenograft model revealed a considerable volumetric reduction of the tumor mass suggesting an interesting *in vivo* pharmacological potency of this compound. Although specific experiments have not been performed yet, the formation of Si409 glucuronide could underestimate the therapeutic potential of Si409. Thus, starting from these promising results, the design of prodrug or the use of drug delivery systems could be an effective strategy to overcome pharmacokinetic obstacles and to candidate Si409 as a possible alternative to commercially available TKIs employed in the treatment of DLBCL.

MATERIALS AND METHODS

1. DRUGS AND MATERIALS

All commercially available chemicals and solvents were used as purchased from Sigma Aldrich Srl (Milan, Italy). Synthesis and characterization of Si409 were previously reported[47].

2. *IN VIVO* PHARMACOKINETIC ASSAYS

Naive male BALB/c mice (Charles River, Wilmington, Massachusetts, USA) were used. All animals were maintained under pathogen-free conditions and approximately 4–6 weeks old when they arrived. The adaption period to the environment was not less than seven days. All the procedures used on animals in this study were approved by Institutional Animal Use and Care Committee at Università degli Studi di Siena and authorized by the Italian Ministry of Health, according to Legislative Decree 116/92, which implemented the European Directive 86/609/EEC on laboratory animal protection in Italy.

2.1 *IN VIVO* ADMINISTRATION OF SI409

For intravenous administration, Si409 was dissolved in a mixture of 10 mM solution of citric acid in presence of tween80 (10% v/v) and benzyl alcohol (1% v/v) as co-solvents. The compound was administered intravenously (caudal tail vein) as a single dose of 25 mg/kg in 200 μL of volume. At several time points (0.08, 0.25, 0.5, 1, 2, and 24h), after drug administration, mice were treated i.p. with heparin (5000 U/kg) and sacrificed under CO_2. Three animals were used for each time point. Orally, mice received a single dose of 200 mg/kg of Si409 (dissolved in the same vehicle used for i.v. studies) in 400 μL of final volume by gavage. At several time-points (0.5, 1, 2, 4, 8, and 24 h) after administration, mice were sacrificed under CO_2. Five animals were used for each time point.

For both administration routes, blood and organs were collected for the following quantitative analysis by UV/LC-MS. Approximately 500–600 μL of blood was

collected from each animal and transferred to a tube containing 10 μL of heparin and mixed briefly. The pharmacokinetic parameters were calculated by non-compartmental analysis using PKSolver software[151].

2.2 SAMPLE PREPARATION

The same procedures described in Section 1 - Materials and Methods, Paragraph 6.1 were used for the extraction of Si409 from biological samples (blood and liver tissue). All quantifications were performed by reference to the appropriate calibration curve.

3. UV/LC-MS INSTRUMENTATION AND ANALYSIS CONDITION

LC analyses were performed with the instrumentation described in Section 1 - Materials and Methods, Paragraph 7. The same experimental conditions for the determination of Si409 and IS were used.

4. MS/MS CHARACTERIZATION OF Si409-GLUCURONATE

The characterization of Si409-glucuronate was performed by LC-MS/MS system consisted of a Varian apparatus (Varian Inc.) including a vacuum solvent degassing unit, two pumps (212-LC), a Triple Quadrupole MSD (Mod. 320-LC) mass spectrometer with ES interface, and Varian MS Workstation System Control Vers. 6.9 software. The instrument operated in positive mode and parameters were: detector 1850 V, drying gas pressure 25.0 psi, desolvation temperature 300.0 °C, nebulizing gas 45.0 psi, needle 5000 V and shield 25 V. Nitrogen was used as nebulizer gas and drying gas. Collision induced dissociation was performed using argon as the collision gas at a pressure of 1.8 mTorr in the collision cell. The capillary voltage was set at 125.0 V and, for the fragmentation studies, the collision energy was progressively increased (from -10 V to -50 V).

LIST OF PUBLICATIONS

1. Alessio Molinari, Giulia Iovenitti, Arianna Mancini, Giovanni Luca Gravina, Monia Chebbi, Maura Caruana, Giulia Vignaroli, Francesco Orofino, Enrico Rango, Adriano Angelucci, Elena Dreassi, Silvia Schenone and Maurizio Botta. AuNP Pyrazolo[3,4-*d*]pyrimidine Nanosystem in Combination with Radiotherapy Against Glioblastoma. *ACS Med. Chem. Lett.* **2020**, *11*, 664-670.
2. Fallacara, A.L.; Zamperini, C.; Podolski-Renić, A.; Dinić, J.; Stanković, T.; Stepanović, M.; Mancini, A.; Rango, E.; Iovenitti, G.; Molinari, A.; Bugli, F.; Sanguinetti, M.; Torelli, M.; Martini, M.; Maccari, L.; Valoti, M.; Dreassi, E.; Botta, M.; Pesić, M.; Schenone, S. A New Strategy for Glioblastoma Treatment: *In Vitro* and *In Vivo* Preclinical Characterization of Si306, a Pyrazolo[3,4-*d*]Pyrimidine Dual Src/P-Glycoprotein Inhibitor. *Cancers* (Basel) **2019**, *11* (6), 848. https//doi.org/10.3390/cancers11060848.

LIST OF SEMINAR AND CONGRESS/WORKSHOP

- 22-25/09/2020 SCHOOL: From Gene to Protein Crystal Structure, GeCrySchool Session II.
- 22-24/07/2020 Italian Young Medicinal Chemistry Virtual Meeting, (DCF-SCI).
- 09/07/2020 8th MS J-Day (DSM-SCI).
- 10-28/03/2020 PERIOD ABROAD at the Goethe University (Frankfurt am Main, Germany) - Research group of Dr. Sebastian Mathea. Early interruption due to global pandemic COVID-19.
- 25/02/2020 Shining Light on Medieval Manuscripts, Andrew Beeby.
- 21-24/01/2020 SCHOOL: From Gene to Protein Crystal Structure, GeCrySchool Session I.
- 22/11/2019 Biosensor for the future, SIMONA SCARANO.
- 20-24/06/2019 SEMINAR: Minicourse in protein physics. Prof. PAOLO CARLONI.
- 19-24/05/2019 CONGRESS: XXII European Workshop in Drug Design – University of Siena (Italy). Prof. MAURIZIO BOTTA.
- 4-5/03/2019 CONGRESS: COST Action CM1406 – WG1 Workshop "Chemical Epigenetics" – University of Salerno (Italy). POSTER PRESENTATION: Enrico Rango, Anna Lucia Fallacara, Arianna Mancini, Giulia Iovenitti, Claudio Zamperini and Maurizio Botta. Formulation, drug delivery systems and pharmacokinetic evaluation of a pyrazolo[3,4-*d*]pyrimidine scaffold-based c-Src inhibitor for Neuroblastoma treatment.
- 13/12/2018 SEMINAR: Realization and application of an innovative technological platform powered by QM/MM simulations for the development of photoactive molecules. Prof. ANNALISA SANTUCCI.
- 14/11/2018 SEMINAR: Synthetic lethality. As a new paradigm for the development of anticancer agents. Prof. ANDREA CAVALLI
- 09/10/2018 SEMINAR "Variations on a theme – vinylogous Mukaiyama aldol reactions in the total syntheses of natural products". Prof. MARKUS KALESSE.
- 24/05/2018 CONGRESS: VII European Workshop in Drug Synthesis. University of Siena (Italy). Prof. MAURIZIO BOTTA.
- 22/03/2018 SEMINAR "Listening to macromolecular dynamics and interactions". Prof. LUCASZ JAREMKO.
- 21/03/2018 SEMINAR "The conformational universe of proteins". Dr. MARIUSZ JAREMKO.
- 12/02/2018 SEMINAR "Organic bioelectronics: fundamentals, biosensors, transducers". Prof. FABIO BISCARINI.

- 09/01/2018 SEMINAR WITH FINAL EVALUATION TEST "Modalità di anestesia e di eutanasia-sacrificio". ORGANISMO PREPOSTO al BENESSERE degli ANIMALI. University of Siena. Dr. GIACOMO MATTEUCCI and Dr. CARLA GAMBARANA.
- 21/11/2017 SEMINAR WITH FINAL EVALUATION TEST "Aggiornamento su legislazione in materia di sperimentazione animale". ORGANISMO PREPOSTO al BENESSERE degli ANIMALI. University of Siena. Dr. GIACOMO MATTEUCCI and Dr. CARLA GAMBARANA.
- 15/11/2017 SEMINAR "Coherent Movement of Charge through Molecules". Prof. THOMAS HANSEN.
- COMPLEMENTARY SKILLS – I corsi trasversali nei Dottorati di Ricerca:
    1. Scientific writing and presentation. Prof. John L. Telford.
    2. Nuovi strumenti per l'analisi della risposta immunitaria alla vaccinazione e all'infezione tramite un approccio di "systems biology". Prof. Annalisa Ciabattini e Francesco Santoro.
    3. Comunicare in ricerca. Prof. Elena Meli.
    4. Spin-off e start up della ricercar. Prof. Lorenzo Zanni e Francesco Senatore.
    5. Comunicare la ricerca. Prof. Agnes Allans Dottir.
    6. Creating value from large archive and big data. Prof. Laura Neri.

BIBLIOGRAPHY

(1) Manning, G.; Whyte, D. B.; Martinez, R.; Hunter, T.; Sudarsanam, S. The Protein Kinase Complement of the Human Genome. *Science* **2002**. https://doi.org/10.1126/science.1075762.

(2) Cheng, F.; Jia, P.; Wang, Q.; Zhao, Z. Quantitative Network Mapping of the Human Kinome Interactome Reveals New Clues for Rational Kinase Inhibitor Discovery and Individualized Cancer Therapy. *Oncotarget* **2014**, *5* (11), 3697–3710. https://doi.org/10.18632/oncotarget.1984.

(3) Cohen, P.; Tcherpakov, M. Will the Ubiquitin System Furnish as Many Drug Targets as Protein Kinases? *Cell* **2010**, *143* (5), 686–693. https://doi.org/10.1016/j.cell.2010.11.016.

(4) Knight, Z. A.; Lin, H.; Shokat, K. M. Targeting the Cancer Kinome through Polypharmacology. *Nature Reviews Cancer* **2010**, pp 130–137. https://doi.org/10.1038/nrc2787.

(5) Duong-Ly, K. C.; Peterson, J. R. The Human Kinome and Kinase Inhibition. *Curr. Protoc. Pharmacol.* **2013**, *0 2* (SUPPL.60), Unit2.9. https://doi.org/10.1002/0471141755.ph0209s60.

(6) Karavasilis, V.; Reid, A.; Sinha, R.; de Bono, J. S. Cancer Drug Resistance. In *Cancer Drug Design and Discovery* **2008**. pp 405–423. https://doi.org/10.1016/B978-012369448-5.50020-3.

(7) Roskoski, R. Src Protein-Tyrosine Kinase Structure and Regulation; *Academic Press Inc.* **2004**; Vol. 324. https://doi.org/10.1016/j.bbrc.2004.09.171.

(8) Roskoski, R. Src Protein-Tyrosine Kinase Structure, Mechanism, and Small Molecule Inhibitors. *Pharmacological Research* **2015**, pp 9–25. https://doi.org/10.1016/j.phrs.2015.01.003.

(9) Thomas, S. M.; Brugge, J. S. Cellular Functions Regulated By Src Family Kinases. *Annu. Rev. Cell Dev. Biol.* **1997**, *13* (1), 513–609. https://doi.org/10.1146/annurev.cellbio.13.1.513.

(10) Roskoski, R. Src Kinase Regulation by Phosphorylation and Dephosphorylation. *Biochem. Biophys. Res. Commun.* **2005**, *331* (1), 1–14. https://doi.org/10.1016/j.bbrc.2005.03.012.

(11) Abram, C. L.; Courtneidge, S. A. Src Family Tyrosine Kinases and Growth Factor Signaling. *Experimental Cell Research* **2000**, pp 1–13. https://doi.org/10.1006/excr.1999.4732.

(12) Playford, M. P.; Schaller, M. D. The Interplay between Src and Integrins in Normal and Tumor Biology. *Oncogene* **2004**, *23* (48), 7928–7946. https://doi.org/10.1038/sj.onc.1208080.

(13) Mitra, S. K.; Schlaepfer, D. D. Integrin-Regulated FAK-Src Signaling in Normal and Cancer Cells. *Curr. Opin. Cell Biol.* **2006**, *18* (5), 516–523. https://doi.org/10.1016/j.ceb.2006.08.011.

(14) Belsches-Jablonski, A. P.; Demory, M. L.; Parsons, J. T.; Parsons, S. J. The Src Pathway as a Therapeutic Strategy. *Drug Discovery Today: Therapeutic Strategies* **2005**, pp 313–321. https://doi.org/10.1016/j.ddstr.2005.11.005.

(15) Cartwright, C. A.; Kamps, M. P.; Meisler, A. I.; Pipas, J. M.; Eckhart, W. Pp60c-Src Activation in Human Colon Carcinoma. *J. Clin. Invest.* **1989**, *83* (6), 2025–2033. https://doi.org/10.1172/JCI114113.

(16) Egan, C.; Pang, A.; Durda, D.; Cheng, H. C.; Wang, J. H.; Fujita, D. J. Activation of Src in Human Breast Tumor Cell Lines: Elevated Levels of Phosphotyrosine Phosphatase Activity That Preferentially Recognizes the Src Carboxy Terminal Negative Regulatory Tyrosine 530. *Oncogene* **1999**, *18* (5), 1227–1237. https://doi.org/10.1038/sj.onc.1202233.

(17) Zhang, J.; Kalyankrishna, S.; Wislez, M.; Thilaganathan, N.; Saigal, B.; Wei, W.; Ma, L.; Wistuba, I. I.; Johnson, F. M.; Kurie, J. M. Src-Family Kinases Are Activated in Non-Small Cell Lung Cancer and Promote the Survival of Epidermal Growth Factor Receptor-Dependent Cell Lines. *Am. J. Pathol.* **2007**. https://doi.org/10.2353/ajpath.2007.060706.

(18) Zhao, R.; Wu, Y.; Wang, T.; Zhang, Y.; Kong, D.; Zhang, L.; Li, X.; Wang, G.; Jin, Y.; Jin, X.; et al. Elevated Src Expression Associated with Hepatocellular Carcinoma Metastasis in Northern Chinese Patients. *Oncol. Lett.* **2015**. https://doi.org/10.3892/ol.2015.3706.

(19) Varkaris, A.; Katsiampoura, A. D.; Araujo, J. C.; Gallick, G. E.; Corn, P. G. Src Signaling Pathways in Prostate Cancer. *Cancer Metastasis Rev.* **2014**, *33* (2–3), 595–606. https://doi.org/10.1007/s10555-013-9481-1.

(20) Hilbig, A. Src Kinase and Pancreatic Cancer. *Recent Results Cancer Res.* **2008**, *177*, 179–185.

(21) Ahluwalia, M. S.; Groot, J. de; Liu, W. M.; Gladson, C. L. Targeting SRC in Glioblastoma Tumors and Brain Metastases: Rationale and Preclinical Studies. *Cancer Letters* **2010**, pp 139–149. https://doi.org/10.1016/j.canlet.2010.08.014.

(22) Du, J.; Bernasconi, P.; Clauser, K. R.; Mani, D. R.; Finn, S. P.; Beroukhim, R.; Burns, M.; Julian, B.; Peng, X. P.; Hieronymus, H.; et al. Bead-Based Profiling of Tyrosine Kinase Phosphorylation Identifies SRC as a Potential Target for Glioblastoma Therapy. *Nat. Biotechnol.* **2009**. https://doi.org/10.1038/nbt.1513.

(23) Yang, X. M.; Walter, G. Specific Kinase Activity and Phosphorylation State of Pp60c-Src from Neuroblastomas and Fibroblasts. *Oncogene* **1988**, *3* (3), 237–244.

(24) Pene-Dumitrescu, T.; Smithgall, T. E. Expression of a Src Family Kinase in Chronic Myelogenous Leukemia Cells Induces Resistance to Imatinib in a Kinase-Dependent Manner. *J. Biol. Chem.* **2010**, *285* (28), 21446–21457. https://doi.org/10.1074/jbc.M109.090043.

(25) Ke, J.; Chelvarajan, R. L.; Sindhava, V.; Robertson, D. A.; Lekakis, L.; Jennings, C. D.; Bondada, S. Anomalous Constitutive Src Kinase Activity Promotes B Lymphoma Survival and Growth. *Mol. Cancer* **2009**. https://doi.org/10.1186/1476-4598-8-132.

(26) Migliaccio, A. R.; Malara, A.; Aliabadi, H. M.; Bousoik, E. "Do We Know Jack" About JAK? A Closer Look at JAK/STAT Signaling Pathway. *Front. Oncol.* **2018**, *1*, 287. https://doi.org/10.3389/fonc.2018.00287.

(27) Gu, Y.; Mohammad, I. S.; Liu, Z. Overview of the STAT-3 Signaling Pathway in Cancer and the Development of Specific Inhibitors (Review). *Oncology Letters* **2020**, pp 2585–2594.

https://doi.org/10.3892/ol.2020.11394.

(28) Bowman, T.; Broome, M. A.; Sinibaldi, D.; Wharton, W.; Pledger, W. J.; Sedivy, J. M.; Irby, R.; Yeatman, T.; Courtneidge, S. A.; Jove, R. Stat3-Mediated Myc Expression Is Required for Src Transformation and PDGF-Induced Mitogenesis. *Proc. Natl. Acad. Sci.* **2001**, *98* (13), 7319–7324. https://doi.org/10.1073/pnas.131568898.

(29) Summy, J. M.; Trevino, J. G.; Lesslie, D. P.; Baker, C. H.; Shakespeare, W. C.; Wang, Y.; Sundaramoorthi, R.; Metcalf, C. A.; Keats, J. A.; Sawyer, T. K.; et al. AP23846, a Novel and Highly Potent Src Family Kinase Inhibitor, Reduces Vascular Endothelial Growth Factor and Interleukin-8 Expression in Human Solid Tumor Cell Lines and Abrogates Downstream Angiogenic Processes. *Mol. Cancer Ther.* **2005**, *4* (12), 1900–1911. https://doi.org/10.1158/1535-7163.MCT-05-0171.

(30) Vantler, M.; Huntgeburth, M.; Caglayan, E.; ten Freyhaus, H.; Schnabel, P.; Rosenkranz, S. PI3-Kinase/Akt-Dependent Antiapoptotic Signaling by the PDGF α Receptor Is Negatively Regulated by Src Family Kinases. *FEBS Lett.* **2006**, *580* (30), 6769–6776. https://doi.org/10.1016/j.febslet.2006.11.034.

(31) Fincham, V. J.; Frame, M. C. The Catalytic Activity of Src Is Dispensable for Translocation to Focal Adhesions but Controls the Turnover of These Structures during Cell Motility. *The EMBO Journal* **1998**; Vol. 17. https://doi.org/10.1093/emboj/17.1.81.

(32) Johansson, M. W.; Larsson, E.; Lüning, B.; Pasquale, E. B.; Ruoslahti, E. Altered Localization and Cytoplasmic Domain-Binding Properties of Tyrosine-Phosphorylated B1 Integrin. *J. Cell Biol.* **1994**, *126* (5), 1299–1309. https://doi.org/10.1083/jcb.126.5.1299.

(33) Nyalendo, C.; Michaud, M.; Beaulieu, E.; Roghi, C.; Murphy, G.; Gingras, D.; Béliveau, R. Src-Dependent Phosphorylation of Membrane Type I Matrix Metalloproteinase on Cytoplasmic Tyrosine 573: Role in Endothelial and Tumor Cell Migration. *J. Biol. Chem.* **2007**, *282* (21), 15690–15699. https://doi.org/10.1074/jbc.M608045200.

(34) Shupnik, M. A. Crosstalk between Steroid Receptors and the C-Src-Receptor Tyrosine Kinase Pathways: Implications for Cell Proliferation. *Oncogene* **2004**, pp 7979–7989. https://doi.org/10.1038/sj.onc.1208076.

(35) Hidaka, H.; Inagaki, M.; Kawamoto, S.; Sasaki, Y. Isoquinolinesulfonamides, Novel and Potent Inhibitors of Cyclic Nucleotide Dependent Protein Kinase and Protein Kinase C. *Biochemistry* **1984**, *23* (21), 5036–5041. https://doi.org/10.1021/bi00316a032.

(36) Knighton, D. R.; Zheng, J.; Ten Eyck, L. F.; Ashford, V. A.; Xuong, N. H.; Taylor, S. S.; Sowadski, J. M. Crystal Structure of the Catalytic Subunit of Cyclic Adenosine Monophosphate-Dependent Protein Kinase. *Science* **1991**, *253* (5018), 407–414. https://doi.org/10.1126/science.1862342.

(37) Lozzio, C. B.; Lozzio, B. B. Human Chronic Myelogenous Leukemia Cell Line with Positive Philadelphia Chromosome. *Blood* **1975**, *45* (3), 321–334. https://doi.org/10.1182/blood.v45.3.321.bloodjournal453321.

(38) Bhullar, K. S.; Lagarón, N. O.; Mcgowan, E. M.; Parmar, I.; Jha, A.; Hubbard, B. P.; Rupasinghe, H. P. V. Kinase-Targeted Cancer Therapies: Progress, Challenges and Future Directions. *Mol Cancer* **2018**, 17(1):48. https://doi.org/10.1186/s12943-018-0804-2.

(39) Dar, A. C.; Shokat, K. M. The Evolution of Protein Kinase Inhibitors from Antagonists to Agonists of Cellular Signaling. *Annu. Rev. Biochem.* **2011**, *80* (1), 769–795. https://doi.org/10.1146/annurev-biochem-090308-173656.

(40) Puls, L. N.; Eadens, M.; Messersmith, W. Current Status of Src Inhibitors in Solid Tumor Malignancies. *Oncologist* **2011**, 16(5):566-78. https://doi.org/10.1634/theoncologist.2010-0408.

(41) Tatton, L.; Morley, G. M.; Chopra, R.; Khwaja, A. The Src-Selective Kinase Inhibitor PP1 Also Inhibits Kit and Bcr-Abl Tyrosine Kinases. *J. Biol. Chem.* **2003**, *278* (7), 4847–4853. https://doi.org/10.1074/jbc.M209321200.

(42) Schenone, S.; Bruno, O.; Ranise, A.; Bondavalli, F.; Brullo, C.; Fossa, P.; Mosti, L.; Menozzi, G.; Carraro, F.; Naldini, A.; et al. New Pyrazolo[3,4-d]Pyrimidines Endowed with A431 Antiproliferative Activity and Inhibitory Properties of Src Phosphorylation. *Bioorganic Med. Chem. Lett.* **2004**, *14* (10), 2511–2517. https://doi.org/10.1016/j.bmcl.2004.03.013.

(43) Spreafico, A.; Schenone, S.; Serchi, T.; Orlandini, M.; Angelucci, A.; Magrini, D.; Bernardini, G.; Collodel, G.; Di Stefano, A.; Tintori, C.; et al. Antiproliferative and Proapoptotic Activities of New Pyrazolo[3,4-d]Pyrimidine Derivative Src Kinase Inhibitors in Human Osteosarcoma Cells . *FASEB J.* **2008**, *22* (5), 1560–1571. https://doi.org/10.1096/fj.07-9873com.

(44) Angelucci, A.; Schenone, S.; Gravina, G. L.; Muzi, P.; Festuccia, C.; Vicentini, C.; Botta, M.; Bologna, M. Pyrazolo[3,4-d]Pyrimidines c-Src Inhibitors Reduce Epidermal Growth Factor-Induced Migration in Prostate Cancer Cells. *Eur. J. Cancer* **2006**, *42* (16), 2838–2845. https://doi.org/10.1016/j.ejca.2006.06.024.

(45) Tintori, C.; Fallacara, A. L.; Radi, M.; Zamperini, C.; Dreassi, E.; Crespan, E.; Maga, G.; Schenone, S.; Musumeci, F.; Brullo, C.; et al. Combining X-Ray Crystallography and Molecular Modeling toward the Optimization of Pyrazolo[3,4-d]Pyrimidines as Potent c-Src Inhibitors Active in Vivo against Neuroblastoma. *J. Med. Chem.* **2015**, *58* (1), 347–361. https://doi.org/10.1021/jm5013159.

(46) Navarra, M.; Celano, M.; Maiuolo, J.; Schenone, S.; Botta, M.; Angelucci, A.; Bramanti, P.; Russo, D. Antiproliferative and Pro-Apoptotic Effects Afforded by Novel Src-Kinase Inhibitors in Human Neuroblastoma Cells. *BMC Cancer* **2010**, *10* (1), 602. https://doi.org/10.1186/1471-2407-10-602.

(47) Molinari, A.; Fallacara, A. L.; Di Maria, S.; Zamperini, C.; Poggialini, F.; Musumeci, F.; Schenone, S.; Angelucci, A.; Colapietro, A.; Crespan, E.; et al. Efficient Optimization of Pyrazolo[3,4-d]Pyrimidines Derivatives as c-Src Kinase Inhibitors in Neuroblastoma Treatment. *Bioorganic Med. Chem. Lett.* **2018**, *28* (21), 3454–3457. https://doi.org/10.1016/j.bmcl.2018.09.024.

(48) Ceccherini, E.; Indovina, P.; Zamperini, C.; Dreassi, E.; Casini, N.; Cutaia, O.; Forte, I. M.; Pentimalli, F.; Esposito, L.; Polito, M. S.; et al. SRC Family Kinase Inhibition through a New Pyrazolo[3,4-d]Pyrimidine Derivative as a Feasible Approach for Glioblastoma Treatment. *J. Cell. Biochem.* **2015**, *116* (5), 856–863. https://doi.org/10.1002/jcb.25042.

(49) Calgani, A.; Vignaroli, G.; Zamperini, C.; Coniglio, F.; Festuccia, C.; Cesare, E. Di; Gravina, G. L.; Mattei, C.; Vitale, F.; Schenone, S.; et al. Suppression of SRC Signaling Is Effective in Reducing Synergy between Glioblastoma and Stromal Cells. *Mol. Cancer Ther.* **2016**, *15* (7), 1535–1544. https://doi.org/10.1158/1535-7163.MCT-15-1011.

(50) Vignaroli, G.; Iovenitti, G.; Zamperini, C.; Coniglio, F.; Calandro, P.; Molinari, A.; Fallacara, A. L.; Sartucci, A.; Calgani, A.; Colecchia, D.; et al. Prodrugs of Pyrazolo[3,4-d]Pyrimidines: From Library Synthesis to Evaluation as Potential Anticancer Agents in an Orthotopic Glioblastoma Model. *J. Med. Chem.* **2017**, *60* (14), 6305–6320. https://doi.org/10.1021/acs.jmedchem.7b00637.

(51) Casini, N.; Forte, I. M.; Mastrogiovanni, G.; Pentimalli, F.; Angelucci, A.; Festuccia, C.; Tomei, V.; Ceccherini, E.; Di Marzo, D.; Schenone, S.; et al. SRC Family Kinase (SFK) Inhibition Reduces Rhabdomyosarcoma Cell Growth in Vitro and in Vivo and Triggers P38 MAP Kinase-Mediated Differentiation. *Oncotarget* **2015**, *6* (14), 12421–12435. https://doi.org/10.18632/oncotarget.3043.

(52) Indovina, P.; Giorgi, F.; Rizzo, V.; Khadang, B.; Schenone, S.; Di Marzo, D.; Forte, I. M.; Tomei, V.; Mattioli, E.; D'Urso, V.; et al. New Pyrazolo[3,4-d]Pyrimidine SRC Inhibitors Induce Apoptosis in Mesothelioma Cell Lines through P27 Nuclear Stabilization. *Oncogene* **2012**, *31* (7), 929–938. https://doi.org/10.1038/onc.2011.286.

(53) Rossi, A.; Schenone, S.; Angelucci, A.; Cozzi, M.; Caracciolo, V.; Pentimalli, F.; Puca, A.; Pucci, B.; La Montagna, R.; Bologna, M.; et al. New Pyrazolo-[3,4-d]pyrimidine Derivative Src Kinase Inhibitors Lead to Cell Cycle Arrest and Tumor Growth Reduction of Human Medulloblastoma Cells . *FASEB J.* **2010**, *24* (8), 2881–2892. https://doi.org/10.1096/fj.09-148593.

(54) Morisi, R.; Celano, M.; Tosi, E.; Schenone, S.; Navarra, M.; Ferretti, E.; Costante, G.; Durante, C.; Botta, G.; D'Agostino, M.; et al. Growth Inhibition of Medullary Thyroid Carcinoma Cells by Pyrazolo-Pyrimidine Derivates. *J. Endocrinol. Invest.* **2007**, *30* (10). https://doi.org/10.1007/BF03349220.

(55) Radi, M.; Tintori, C.; Musumeci, F.; Brullo, C.; Zamperini, C.; Dreassi, E.; Fallacara, A. L.; Vignaroli, G.; Crespan, E.; Zanoli, S.; et al. Design, Synthesis, and Biological Evaluation of Pyrazolo[3,4-d]Pyrimidines Active in Vivo on the Bcr-Abl T315I Mutant. *J. Med. Chem.* **2013**, *56* (13), 5382–5394. https://doi.org/10.1021/jm400233w.

(56) Cozzi, M.; Giorgi, F.; Marcelli, E.; Pentimalli, F.; Forte, I. M.; Schenone, S.; D'Urso, V.; De Falco, G.; Botta, M.; Giordano, A.; et al. Antitumor Activity of New Pyrazolo[3,4-d] Pyrimidine SRC Kinase Inhibitors in Burkitt Lymphoma Cell Lines and Its Enhancement by WEE1 Inhibition. *Cell Cycle* **2012**, *11* (5), 1029–1039. https://doi.org/10.4161/cc.11.5.19519.

(57) Manetti, F.; Pucci, A.; Magnani, M.; Locatelli, G. A.; Brullo, C.; Naldini, A.; Schenone, S.; Maga, G.; Carraro, F.; Botta, M. Inhibition of Bcr-Abl Phosphorylation and Induction of Apoptosis by Pyrazolo[3,4-d]Pyrimidines in Human Leukemia Cells. *ChemMedChem* **2007**, *2* (3), 343–353. https://doi.org/10.1002/cmdc.200600214.

(58) Radi, M.; Tintori, C.; Musumeci, F.; Brullo, C.; Zamperini, C.; Dreassi, E.; Fallacara, A. L.; Vignaroli, G.; Crespan, E.; Zanoli, S.; et al. Design, Synthesis, and Biological Evaluation of Pyrazolo[3,4-d]Pyrimidines Active in Vivo on the Bcr-Abl T315I Mutant. *J. Med. Chem.* **2013**, *56* (13), 5382–5394. https://doi.org/10.1021/jm400233w.

(59) Delle Monache, S.; Sanità, P.; Calgani, A.; Schenone, S.; Botta, L.; Angelucci, A. Src Inhibition Potentiates Antitumoral Effect of Paclitaxel by Blocking Tumor-Induced Angiogenesis. *Exp. Cell Res.* **2014**, *328* (1), 20–31. https://doi.org/10.1016/j.yexcr.2014.08.002.

(60) Fallacara, A. L.; Zamperini, C.; Podolski-Renić, A.; Dinić, J.; Stanković, T.; Stepanović, M.; Mancini, A.; Rango, E.; Iovenitti, G.; Molinari, A.; et al. A New Strategy for Glioblastoma Treatment: In Vitro and in Vivo Preclinical Characterization of Si306, a Pyrazolo[3,4-d]Pyrimidine Dual Src/P-Glycoprotein Inhibitor. *Cancers (Basel).* **2019**, *11* (6). https://doi.org/10.3390/cancers11060848.

(61) Maness, P. F. Nonreceptor Protein Tyrosine Kinases Associated with Neuronal Development. *Developmental Neuroscience* **1992**, pp 257–270. https://doi.org/10.1159/000111670.

(62) Dolecek, T. A.; Propp, J. M.; Stroup, N. E.; Kruchko, C. CBTRUS Statistical Report: Primary Brain and Central Nervous System Tumors Diagnosed in the United States in 2005-2009. *Neuro-Oncology* **2012**. https://doi.org/10.1093/neuonc/nos218.

(63) Orphanet: Search a disease https://www.orpha.net/consor/cgi-bin/Disease_Search.php?lng=EN&data_id=3752&Disease_Disease_Search_diseaseGroup=glioblastoma&Disease_Disease_Search_diseaseType=Pat&Disease(s)/group of diseases=Glioblastoma Title=Glioblastoma Search=Disease Search_Simple (accessed Oct 25, 2019). (accessed Sep 3, 2020).

(64) Stettner, M. R.; Wang, W.; Nabors, L. B.; Bharara, S.; Flynn, D. C.; Grammer, J. R.; Gillespie,

G. Y.; Gladson, C. L. Lyn Kinase Activity Is the Predominant Cellular Src Kinase Activity in Glioblastoma Tumor Cells. *Cancer Res.* **2005**, *65* (13), 5535–5543. https://doi.org/10.1158/0008-5472.CAN-04-3688.

(65) Du, J.; Bernasconi, P.; Clauser, K. R.; Mani, D. R.; Finn, S. P.; Beroukhim, R.; Burns, M.; Julian, B.; Peng, X. P.; Hieronymus, H.; et al. Bead-Based Profiling of Tyrosine Kinase Phosphorylation Identifies SRC as a Potential Target for Glioblastoma Therapy. *Nat. Biotechnol.* **2009**, *27* (1), 77–83. https://doi.org/10.1038/nbt.1513.

(66) Weissenberger, J.; Steinbach, J. P.; Malin, G.; Spada, S.; Rülicke, T.; Aguzzi, A. Development and Malignant Progression of Astrocytomas in GFAP-v-Src Transgenic Mice. *Oncogene* **1997**, *14* (17), 2005–2013. https://doi.org/10.1038/sj.onc.1201168.

(67) Taylor, J. W.; Dietrich, J.; Gerstner, E. R.; Norden, A. D.; Rinne, M. L.; Cahill, D. P.; Stemmer-Rachamimov, A.; Wen, P. Y.; Betensky, R. A.; Giorgio, D. H.; et al. Phase 2 Study of Bosutinib, a Src Inhibitor, in Adults with Recurrent Glioblastoma. *J. Neurooncol.* **2015**, *121* (3), 557–563. https://doi.org/10.1007/s11060-014-1667-z.

(68) Cheung, N. K. V.; Dyer, M. A. Neuroblastoma: Developmental Biology, Cancer Genomics and Immunotherapy. *Nature Reviews Cancer* **2013**, pp 397–411. https://doi.org/10.1038/nrc3526.

(69) Matthay, K. K.; Villablanca, J. G.; Seeger, R. C.; Stram, D. O.; Harris, R. E.; Ramsay, N. K.; Swift, P.; Shimada, H.; Black, C. T.; Brodeur, G. M.; et al. Treatment of High-Risk Neuroblastoma with Intensive Chemotherapy, Radiotherapy, Autologous Bone Marrow Transplantation, and 13-Cis-Retinoic Acid. *N. Engl. J. Med.* **1999**, *341* (16), 1165–1173. https://doi.org/10.1056/NEJM199910143411601.

(70) Matsunaga, T.; Shirasawa, H.; Tanabe, M.; Ohnuma, N.; Takahashi, H.; Simi, B. Expression of Alternatively Spliced Src Messenger RNAs Related to Neuronal Differentiation in Human Neuroblastomas. *Cancer Research* **1993**, 53, 3179-3185.

(71) DeSeau, V.; Rosen, N.; Bolen, J. B. Analysis of Pp60c-src Tyrosine Kinase Activity and Phosphotyrosyl Phosphatase Activity in Human Colon Carcinoma and Normal Human Colon Mucosal Cells. *J. Cell. Biochem.* **1987**, *35* (2), 113–128. https://doi.org/10.1002/jcb.240350205.

(72) Pahlman, S.; Hammerling, U. Src Expression in Small-Cell Lung Carcinoma and Other Neuroendocrine Malignancies. In *American Review of Respiratory Disease* **1990**, Vol. 142. https://doi.org/10.1164/ajrccm/142.6_pt_2.s54.

(73) Kratimenos, P.; Koutroulis, I.; Marconi, D.; Syriopoulou, V.; Delivoria-Papadopoulos, M.; Chrousos, G. P.; Theocharis, S. Multi-Targeted Molecular Therapeutic Approach in Aggressive Neuroblastoma: The Effect of Focal Adhesion Kinase-Src-Paxillin System. *Expert*

Opinion on Therapeutic Targets **2014**, pp 1395–1406. https://doi.org/10.1517/14728222.2014.952280.

(74) Bieerkehazhi, S.; Chen, Z.; Zhao, Y.; Yu, Y.; Zhang, H.; Vasudevan, S. A.; Woodfield, S. E.; Tao, L.; Yi, J. S.; Muscal, J. A.; et al. Novel Src/Abl Tyrosine Kinase Inhibitor Bosutinib Suppresses Neuroblastoma Growth via Inhibiting Src/Abl Signaling. *Oncotarget* **2017**, *8* (1), 1469–1480. https://doi.org/10.18632/oncotarget.13643.

(75) Vitali, R.; Mancini, C.; Cesi, V.; Tanno, B.; Piscitelli, M.; Mancuso, M.; Sesti, F.; Pasquali, E.; Calabretta, B.; Dominici, C.; et al. Activity of Tyrosine Kinase Inhibitor Dasatinib in Neuroblastoma Cells in Vitro and in Orthotopic Mouse Model. *Int. J. Cancer* **2009**, *125* (11), 2547–2555. https://doi.org/10.1002/ijc.24606.

(76) Swerdlow, S. H.; Campo, E.; Pileri, S. A.; Harris, N. L.; Stein, H.; Siebert, R.; Advani, R.; Ghielmini, M.; Salles, G. A.; Zelenetz, A. D.; et al. The 2016 Revision of the World Health Organization Classification of Lymphoid Neoplasms. *Blood* **2016**, *127* (20), 2375–2390. https://doi.org/10.1182/blood-2016-01-643569.

(77) Ansell, S. M. Hodgkin Lymphoma: Diagnosis and Treatment. In *Mayo Clinic Proceedings*; Elsevier Ltd, 2015; Vol. 90, pp 1574–1583. https://doi.org/10.1016/j.mayocp.2015.07.005.

(78) Pasqualucci, L.; Dalla-Favera, R. Genetics of Diffuse Large B-Cell Lymphoma. *Blood* **2018**, *131* (21), 2307–2319. https://doi.org/10.1182/blood-2017-11-764332.

(79) Van Arnam, J. S.; Lim, M. S.; Elenitoba-Johnson, K. S. J. Novel Insights into the Pathogenesis of T-Cell Lymphomas. *Blood* **2018**, *131* (21), 2320–2330. https://doi.org/10.1182/blood-2017-11-764357.

(80) Battistello, E.; Katanayeva, N.; Dheilly, E.; Tavernari, D.; Donaldson, M. C.; Bonsignore, L.; Thome, M.; Christie, A. L.; Murakami, M. A.; Michielin, O.; et al. Pan-SRC Kinase Inhibition Blocks B-Cell Receptor Oncogenic Signaling in Non-Hodgkin Lymphoma. *Blood* **2018**, *131* (21), 2345–2356. https://doi.org/10.1182/blood-2017-10-809210.

(81) Palomero, T.; Couronné, L.; Khiabanian, H.; Kim, M.-Y.; Ambesi-Impiombato, A.; Perez-Garcia, A.; Carpenter, Z.; Abate, F.; Allegretta, M.; Haydu, J. E.; et al. Recurrent Mutations in Epigenetic Regulators, RHOA and FYN Kinase in Peripheral T Cell Lymphomas. *Nat. Genet.* **2014**, *46* (2), 166–170. https://doi.org/10.1038/ng.2873.

(82) Krejsgaard, T.; Vetter-Kauczok, C. S.; Woetmann, A.; Kneitz, H.; Eriksen, K. W.; Lovato, P.; Zhang, Q.; Wasik, M. A.; Geisler, C.; Ralfkiaer, E.; et al. Ectopic Expression of B-Lymphoid Kinase in Cutaneous T-Cell Lymphoma. *Blood* **2009**, *113* (23), 5896–5904. https://doi.org/10.1182/blood-2008-09-181024.

(83) Petersen, D. L.; Krejsgaard, T.; Berthelsen, J.; Fredholm, S.; Willerslev-Olsen, A.; Sibbesen, N. A.; Bonefeld, C. M.; Andersen, M. H.; Francavilla, C.; Olsen, J. V; et al. B-Lymphoid Tyrosine

Kinase (Blk) Is an Oncogene and a Potential Target for Therapy with Dasatinib in Cutaneous T-Cell Lymphoma (CTCL). *Leukemia* **2014**, *28* (10), 2109–2112. https://doi.org/10.1038/leu.2014.192.

(84) Fallacara, A. L.; Passannanti, R.; Mori, M.; Iovenitti, G.; Musumeci, F.; Greco, C.; Crespan, E.; Kissova, M.; Maga, G.; Tarantelli, C.; et al. Identification of a New Family of Pyrazolo[3,4-d]Pyrimidine Derivatives as Multitarget Fyn-Blk-Lyn Inhibitors Active on B- and T-Lymphoma Cell Lines. *Eur. J. Med. Chem.* **2019**, *181*, 111545. https://doi.org/10.1016/j.ejmech.2019.07.048.

(85) Cohen, M. H.; Gootenberg, J.; Keegan, P.; Pazdur, R. FDA Drug Approval Summary: Bevacizumab (Avastin®) Plus Carboplatin and Paclitaxel as First-Line Treatment of Advanced/Metastatic Recurrent Nonsquamous Non-Small Cell Lung Cancer. *Oncologist* **2007**, *12* (6), 713–718. https://doi.org/10.1634/theoncologist.12-6-713.

(86) Cohen, M. H.; Gootenberg, J.; Keegan, P.; Pazdur, R. FDA Drug Approval Summary: Bevacizumab Plus FOLFOX4 as Second-Line Treatment of Colorectal Cancer. *Oncologist* **2007**, *12* (3), 356–361. https://doi.org/10.1634/theoncologist.12-3-356.

(87) Pagnan, G.; Montaldo, P. G.; Pastorino, F.; Raffaghello, L.; Kirchmeier, M.; Allen, T. M.; Ponzoni, M. GD2-Mediated Melanoma Cell Targeting and Cytotoxicity of Liposome-Entrapped Fenretinide. *Int. J. Cancer* **1999**, *81* (2), 268–274. https://doi.org/10.1002/(sici)1097-0215(19990412)81:2<268::aid-ijc17>3.0.co;2-1.

(88) Wiegandt, H. The Chemical Constitution of Gangliosides of the Vertebrate Nervous System. *Behav. Brain Res.* **1995**, *66* (1–2), 85–97. https://doi.org/10.1016/0166-4328(94)00129-4.

(89) Ryan, J. M.; Rice, G. E.; Mitchell, M. D. The Role of Gangliosides in Brain Development and the Potential Benefits of Perinatal Supplementation. *Nutrition Research* **2013**, pp 877–887. https://doi.org/10.1016/j.nutres.2013.07.021.

(90) Posse de Chaves, E.; Sipione, S. Sphingolipids and Gangliosides of the Nervous System in Membrane Function and Dysfunction. *FEBS Letters* **2010**, pp 1748–1759. https://doi.org/10.1016/j.febslet.2009.12.010.

(91) Yu, R. K.; Nakatani, Y.; Yanagisawa, M. The Role of Glycosphingolipid Metabolism in the Developing Brain. *Journal of Lipid Research* **2009**. https://doi.org/10.1194/jlr.R800028-JLR200.

(92) Schnaar, R. L. Brain Gangliosides in Axon-Myelin Stability and Axon Regeneration. *FEBS Letters* **2010**, pp 1741–1747. https://doi.org/10.1016/j.febslet.2009.10.011.

(93) Sheikh, K. A.; Deerinck, T. J.; Ellisman, M. H.; Griffin, J. W. The Distribution of Ganglioside-like Moieties in Peripheral Nerves. *Brain* **1999**, *122* (3), 449–460. https://doi.org/10.1093/brain/122.3.449.

(94) Chang, H. R.; Cordon-Cardo, C.; Houghton, A. N.; Cheung, N. V.; Brennan, M. F. Expression

of Disialogangliosides GD2 and GD3 on Human Soft Tissue Sarcomas. *Cancer* **1992**, *70* (3), 633–638. https://doi.org/10.1002/1097-0142(19920801)70:3<633.

(95) Cheresh, D. A.; Harper, J. R.; Schulz, G.; Reisfeld, R. A. Localization of the Gangliosides GD2 and GD3 in Adhesion Plaques and on the Surface of Human Melanoma Cells. *Proc. Natl. Acad. Sci. U. S. A.* **1984**, *81* (18 I), 5767–5771. https://doi.org/10.1073/pnas.81.18.5767.

(96) Cheresh, D. A.; Pierschbacher, M. D.; Herzig, M. A.; Mujoo, K. Disialogangliosides GD2 and GD3 Are Involved in the Attachment of Human Melanoma and Neuroblastoma Cells to Extracellular Matrix Proteins. *J. Cell Biol.* **1986**, *102* (3), 688–696. https://doi.org/10.1083/jcb.102.3.688.

(97) Grimm, E. A.; Mazumder, A.; Zhang, H. Z.; Rosenberg, S. A. Lymphokine-Activated Killer Cell Phenomenon. Lysis of Natural Killer-Resistant Fresh Solid Tumor Cells by Interleukin 2-Activated Autologous Human Peripheral Blood Lymphocytes. *J. Exp. Med.* **1982**, *155* (6), 1823–1841. https://doi.org/10.1084/jem.155.6.1823.

(98) Restifo, N. P.; Dudley, M. E.; Rosenberg, S. A. Adoptive Immunotherapy for Cancer: Harnessing the T Cell Response. *Nature Reviews Immunology* **2012**, pp 269–281. https://doi.org/10.1038/nri3191.

(99) Adams, G. P.; Weiner, L. M. Monoclonal Antibody Therapy of Cancer. *Nature Biotechnology* **2005**, pp 1147–1157. https://doi.org/10.1038/nbt1137.

(100) Cheung, N.-K. V.; Saarinen, U. M.; Neely, J. E.; Landmeier, B.; Donovan, D.; Coccia, P. F. Monoclonal Antibodies to a Glycolipid Antigen on Human Neuroblastoma Cells. *Cancer Res.* **1985**, *45* (6).

(101) Cheung, I. Y.; Lo Piccolo, M. S.; Kushner, B. H.; Kramer, K.; Cheung, N. K. V. Quantitation of GD2 Synthase MRNA by Real-Time Reverse Transcriptase Polymerase Chain Reaction: Clinical Utility in Evaluating Adjuvant Therapy in Neuroblastoma. *J. Clin. Oncol.* **2003**, *21* (6), 1087–1093. https://doi.org/10.1200/JCO.2003.02.055.

(102) McGinty, L.; Kolesar, J. Dinutuximab for Maintenance Therapy in Pediatric Neuroblastoma. *Am. J. Heal. Pharm.* **2017**, *74* (8), 563–567. https://doi.org/10.2146/ajhp160228.

(103) Yu, A. L.; Gilman, A. L.; Ozkaynak, M. F.; London, W. B.; Kreissman, S. G.; Chen, H. X.; Smith, M.; Anderson, B.; Villablanca, J. G.; Matthay, K. K.; et al. Anti-GD2 Antibody with GM-CSF, Interleukin-2, and Isotretinoin for Neuroblastoma. *N. Engl. J. Med.* **2010**, *363* (14), 1324–1334. https://doi.org/10.1056/nejmoa0911123.

(104) Modak, S.; Cheung, N. K. V. Disialoganglioside Directed Immunotherapy of Neuroblastoma. *Cancer Investigation* **2007**, pp 67–77. https://doi.org/10.1080/07357900601130763.

(105) Cheung, N. K. V.; Cheung, I. Y.; Kushner, B. H.; Ostrovnaya, I.; Chamberlain, E.; Kramer, K.; Modak, S. Murine Anti-GD2 Monoclonal Antibody 3F8 Combined with Granulocyte-

Macrophage Colony-Stimulating Factor and 13-Cis-Retinoic Acid in High-Risk Patients with Stage 4 Neuroblastoma in First Remission. *J. Clin. Oncol.* **2012**, *30* (26), 3264–3270. https://doi.org/10.1200/JCO.2011.41.3807.

(106) Kushner, B. H.; Kramer, K.; Cheung, N. K. V. Phase II Trial of the Anti-GD2 Monoclonal Antibody 3F8 and Granulocyte-Macrophage Colony-Stimulating Factor for Neuroblastoma. *J. Clin. Oncol.* **2001**, *19* (22), 4189–4194. https://doi.org/10.1200/JCO.2001.19.22.4189.

(107) Ahmed, M.; Cheung, N. K. V. Engineering Anti-GD2 Monoclonal Antibodies for Cancer Immunotherapy. *FEBS Letters* **2014**, pp 288–297. https://doi.org/10.1016/j.febslet.2013.11.030.

(108) Ahmed, M.; Goldgur, Y.; Hu, J.; Guo, H.-F.; Cheung, N.-K. V. In Silico Driven Redesign of a Clinically Relevant Antibody for the Treatment of GD2 Positive Tumors. *PLoS One* **2013**, *8* (5), e63359. https://doi.org/10.1371/journal.pone.0063359.

(109) Navid, F.; M. Santana, V.; C. Barfield, R. Anti-GD2 Antibody Therapy for GD2-Expressing Tumors. *Curr. Cancer Drug Targets* **2010**, *10* (2), 200–209. https://doi.org/10.2174/156800910791054167.

(110) Parsons, K.; Bernhardt, B.; Strickland, B. Targeted Immunotherapy for High-Risk Neuroblastoma—The Role of Monoclonal Antibodies. *Ann. Pharmacother.* **2013**, *47* (2), 210–218. https://doi.org/10.1345/aph.1R353.

(111) Yang, R. K.; Sondel, P. M. Anti-GD2 Strategy in the Treatment of Neuroblastoma. *Drugs of the Future* **2010**, pp 665–673. https://doi.org/10.1358/dof.2010.035.08.1513490.

(112) Bangham, A. D. Physical Structure And Behavior Of Lipids And Lipid Enzymes. *Adv. Lipid Res.* **1963**, *1*, 65–104.

(113) Sercombe, L.; Veerati, T.; Moheimani, F.; Wu, S. Y.; Sood, A. K.; Hua, S. Advances and Challenges of Liposome Assisted Drug Delivery. *Frontiers in Pharmacology* **2015**. https://doi.org/10.3389/fphar.2015.00286.

(114) Riaz, M.; Riaz, M.; Zhang, X.; Lin, C.; Wong, K.; Chen, X.; Zhang, G.; Lu, A.; Yang, Z. Surface Functionalization and Targeting Strategies of Liposomes in Solid Tumor Therapy: A Review. *Int. J. Mol. Sci.* **2018**, *19* (1), 195. https://doi.org/10.3390/ijms19010195.

(115) Gabizon, A. A.; Barenholz, Y.; Bialer, M. Prolongation of the Circulation Time of Doxorubicin Encapsulated in Liposomes Containing a Polyethylene Glycol-Derivatized Phospholipid: Pharmacokinetic Studies in Rodents and Dogs. *Pharm. Res. An Off. J. Am. Assoc. Pharm. Sci.* **1993**, *10* (5), 703–708. https://doi.org/10.1023/A:1018907715905.

(116) Bulbake, U.; Doppalapudi, S.; Kommineni, N.; Khan, W. Liposomal Formulations in Clinical Use: An Updated Review. *Pharmaceutics* **2017**. https://doi.org/10.3390/pharmaceutics9020012.

(117) Torchilin, V. P.; Omelyanenko, V. G.; Papisov, M. I.; Bogdanov, A. A.; Trubetskoy, V. S.; Herron, J. N.; Gentry, C. A. Poly(Ethylene Glycol) on the Liposome Surface: On the

Mechanism of Polymer-Coated Liposome Longevity. *Biochim. Biophys. Acta* **1994**, *1195* (1), 11–20. https://doi.org/10.1016/0005-2736(94)90003-5.

(118) Drummond, D. C.; Meyer, O.; Hong, K.; Kirpotin, D. B.; Papahadjopoulos, D. Optimizing Liposomes for Delivery of Chemotherapeutic Agents to Solid Tumors. *Pharmacol. Rev.* **1999**, *51* (4), 691–743.

(119) Ngoune, R.; Peters, A.; von Elverfeldt, D.; Winkler, K.; Pütz, G. Accumulating Nanoparticles by EPR: A Route of No Return. *J. Control. Release* **2016**, *238*, 58–70. https://doi.org/10.1016/j.jconrel.2016.07.028.

(120) Golombek, S. K.; May, J. N.; Theek, B.; Appold, L.; Drude, N.; Kiessling, F.; Lammers, T. Tumor Targeting via EPR: Strategies to Enhance Patient Responses. *Advanced Drug Delivery Reviews* **2018**, pp 17–38. https://doi.org/10.1016/j.addr.2018.07.007.

(121) Ling, S. S. N.; Yuen, K. H.; Magosso, E.; Barker, S. A. Oral Bioavailability Enhancement of a Hydrophilic Drug Delivered via Folic Acid-Coupled Liposomes in Rats. *J. Pharm. Pharmacol.* **2009**, *61* (4), 445–449. https://doi.org/10.1211/jpp/61.04.0005.

(122) Sugano, M.; Egilmez, N. K.; Yokota, S. J.; Chen, F. A.; Harding, J.; Huang, S. K.; Bankert, R. B. Antibody Targeting of Doxorubicin-Loaded Liposomes Suppresses the Growth and Metastatic Spread of Established Human Lung Tumor Xenografts in Severe Combined Immunodeficient Mice. *Cancer Res.* **2000**, *60* (24), 6942–6949.

(123) Park, J. W.; Hong, K.; Kirpotin, D. B.; Meyer, O.; Papahadjopoulos, D.; Benz, C. C. Anti-HER2 Immunoliposomes for Targeted Therapy of Human Tumors. *Cancer Lett.* **1997**, *118* (2), 153–160. https://doi.org/10.1016/s0304-3835(97)00326-1.

(124) Pastorino, F.; Brignole, C.; Marimpietri, D.; Sapra, P.; Moase, E. H.; Allen, T. M.; Ponzoni, M. Doxorubicin-Loaded Fab' Fragments of Anti-Disialoganglioside Immunoliposomes Selectively Inhibit the Growth and Dissemination of Human Neuroblastoma in Nude Mice. *Cancer Res.* **2003**, *63* (1), 86–92.

(125) Pagnan, G.; Stuart, D. D.; Pastorino, F.; Raffaghello, L.; Montaldo, P. G.; Allen, T. M.; Calabretta, B.; Ponzoni, M. Delivery of C-Myb Antisense Oligodeoxynucleotides to Human Neuroblastoma Cells via Disialoganglioside GD(2)-Targeted Immunoliposomes: Antitumor Effects. *J. Natl. Cancer Inst.* **2000**, *92* (3), 253–261. https://doi.org/10.1093/jnci/92.3.253.

(126) Lopes de Menezes, D. E.; Pilarski, L. M.; Allen, T. M. In Vitro and in Vivo Targeting of Immunoliposomal Doxorubicin to Human B-Cell Lymphoma. *Cancer Res.* **1998**, *58* (15), 3320–3330.

(127) Nicholls, P.; West, J.; Bangham, A. D. Chlorophyll b Containing Liposomes: Effect of Thermal Transitions on Catalytic and Spectral Properties. *BBA - Biomembr.* **1974**, *363* (2), 190–201. https://doi.org/10.1016/0005-2736(74)90058-3.

(128) Koudelka, S.; Turánek, J. Liposomal Paclitaxel Formulations. *J. Control. Release* **2012**, *163* (3), 322–334. https://doi.org/10.1016/j.jconrel.2012.09.006.

(129) Needham, D.; Sarpal, R. S. Binding of Paclitaxel to Lipid Interfaces: Correlations with Interface Compliance. *J. Liposome Res.* **1998**, *8* (2), 147–163. https://doi.org/10.3109/08982109809035523.

(130) Zhou, Y.; Wang, C. Y.; Zhu, Y. R.; Chen, Z. Y. A Novel Ultraviolet Irradiation Technique for Shape-Controlled Synthesis of Gold Nanoparticles at Room Temperature. *Chem. Mater.* **1999**, *11* (9), 2310–2312. https://doi.org/10.1021/cm990315h.

(131) Zhang, W.; Wang, F.; Wang, Y.; Wang, J.; Yu, Y.; Guo, S.; Chen, R.; Zhou, D. PH and Near-Infrared Light Dual-Stimuli Responsive Drug Delivery Using DNA-Conjugated Gold Nanorods for Effective Treatment of Multidrug Resistant Cancer Cells. *J. Control. Release* **2016**, *232*, 9–19. https://doi.org/10.1016/j.jconrel.2016.04.001.

(132) Zhang, Y.; Qian, J.; Wang, D.; Wang, Y.; He, S. Multifunctional Gold Nanorods with Ultrahigh Stability and Tunability for in Vivo Fluorescence Imaging, SERS Detection, and Photodynamic Therapy. *Angew. Chemie - Int. Ed.* **2013**, *52* (4), 1148–1151. https://doi.org/10.1002/anie.201207909.

(133) Yin, D.; Li, X.; Ma, Y.; Liu, Z. Targeted Cancer Imaging and Photothermal Therapy via Monosaccharide-Imprinted Gold Nanorods. *Chem. Commun.* **2017**, *53* (50), 6716–6719. https://doi.org/10.1039/c7cc02247f.

(134) Yeh, Y. C.; Creran, B.; Rotello, V. M. Gold Nanoparticles: Preparation, Properties, and Applications in Bionanotechnology. *Nanoscale* **2012**, pp 1871–1880. https://doi.org/10.1039/c1nr11188d.

(135) Yang, Z.; Li, Z.; Lu, X.; He, F.; Zhu, X.; Ma, Y.; He, R.; Gao, F.; Ni, W.; Yi, Y. Controllable Biosynthesis and Properties of Gold Nanoplates Using Yeast Extract. *Nano-Micro Lett.* **2017**, *9* (1). https://doi.org/10.1007/s40820-016-0102-8.

(136) Wang, Y.; Black, K. C. L.; Luehmann, H.; Li, W.; Zhang, Y.; Cai, X.; Wan, D.; Liu, S. Y.; Li, M.; Kim, P.; et al. Comparison Study of Gold Nanohexapods, Nanorods, and Nanocages for Photothermal Cancer Treatment. *ACS Nano* **2013**, *7* (3), 2068–2077. https://doi.org/10.1021/nn304332s.

(137) Wang, J.; Zhu, G.; You, M.; Song, E.; Shukoor, M. I.; Zhang, K.; Altman, M. B.; Chen, Y.; Zhu, Z.; Huang, C. Z.; et al. Assembly of Aptamer Switch Probes and Photosensitizer on Gold Nanorods for Targeted Photothermal and Photodynamic Cancer Therapy. *ACS Nano* **2012**, *6* (6), 5070–5077. https://doi.org/10.1021/nn300694v.

(138) Manjunath, H. M.; Joshi, C. G.; Raju, N. G. Biofabrication of Gold Nanoparticles Using Marine Endophytic Fungus - Penicillium Citrinum. In *IET Nanobiotechnology* **2017**; Vol. 11, pp 40–44.

https://doi.org/10.1049/iet-nbt.2016.0065.

(139) Liu, J.; Detrembleur, C.; De Pauw-Gillet, M. C.; Mornet, S.; Jérôme, C.; Duguet, E. Gold Nanorods Coated with Mesoporous Silica Shell as Drug Delivery System for Remote near Infrared Light-Activated Release and Potential Phototherapy. *Small* **2015**, *11* (19), 2323–2332. https://doi.org/10.1002/smll.201402145.

(140) Liu, H.; Lian, T.; Liu, Y.; Hong, Y.; Sun, D.; Li, Q. Plant-Mediated Synthesis of Au Nanoparticles: Separation and Identification of Active Biomolecule in the Water Extract of Cacumen Platycladi. *Ind. Eng. Chem. Res.* **2017**, *56* (18), 5262–5270. https://doi.org/10.1021/acs.iecr.7b00064.

(141) Vignaroli, G.; Calandro, P.; Zamperini, C.; Coniglio, F.; Iovenitti, G.; Tavanti, M.; Colecchia, D.; Dreassi, E.; Valoti, M.; Schenone, S.; et al. Improvement of Pyrazolo[3,4-d]Pyrimidines Pharmacokinetic Properties: Nanosystem Approaches for Drug Delivery. *Sci. Rep.* **2016**, *6*, 21509–21509. https://doi.org/10.1038/srep21509.

(142) Horwacik, I.; Rokita, H. Modulation of Interactions of Neuroblastoma Cell Lines with Extracellular Matrix Proteins Affects Their Sensitivity to Treatment with the Anti-GD2 Ganglioside Antibody 14G2a. *Int. J. Oncol.* **2017**, *50* (5), 1899–1914. https://doi.org/10.3892/ijo.2017.3959.

(143) Gokhale, P. C.; Radhakrishnan, B.; Husain, S. R.; Abernethy, D. R.; Sacher, R.; Dritschilo, A.; Rahman, A. An Improved Method of Encapsulation of Doxorubicin in Liposomes: Pharmacological, Toxicological and Therapeutic Evaluation. *Br. J. Cancer* **1996**, *74* (1), 43–48. https://doi.org/10.1038/bjc.1996.313.

(144) Jonah, M. M.; Cerny, E. A.; Rahman, Y. E. Tissue Distribution of EDTA Encapsulated within Liposomes of Varying Surface Properties. *BBA - Biomembr.* **1975**, *401* (3), 336–348. https://doi.org/10.1016/0005-2736(75)90234-5.

(145) Zhao, L.; Wei, Y. meng; Zhong, X. dong; Liang, Y.; Zhang, X. mei; Li, W.; Li, B. bo; Wang, Y.; Yu, Y. PK and Tissue Distribution of Docetaxel in Rabbits after i.v. Administration of Liposomal and Injectable Formulations. *J. Pharm. Biomed. Anal.* **2009**, *49* (4), 989–996. https://doi.org/10.1016/j.jpba.2009.01.016.

(146) Dokka, S.; Toledo, D.; Shi, X.; Castranova, V.; Rojanasakul, Y. Oxygen Radical-Mediated Pulmonary Toxicity Induced by Some Cationic Liposomes. *Pharm. Res.* **2000**, *17* (5), 521–525. https://doi.org/10.1023/A:1007504613351.

(147) Knudsen, K. B.; Northeved, H.; Pramod Kumar, E. K.; Permin, A.; Gjetting, T.; Andresen, T. L.; Larsen, S.; Wegener, K. M.; Lykkesfeldt, J.; Jantzen, K.; et al. In Vivo Toxicity of Cationic Micelles and Liposomes. *Nanomedicine Nanotechnology, Biol. Med.* **2015**, *11* (2), 467–477. https://doi.org/10.1016/j.nano.2014.08.004.

(148) Immordino, M. L.; Dosio, F.; Cattel, L. Stealth Liposomes: Review of the Basic Science, Rationale, and Clinical Applications, Existing and Potential. *International Journal of Nanomedicine* **2006**, pp 297–315. https://doi.org/10.2217/17435889.1.3.297.

(149) Gregoriadis, G.; McCormack, B.; Obrenovic, M.; Saffie, R.; Zadi, B.; Perrie, Y. Vaccine Entrapment in Liposomes. *Methods* **1999**, *19* (1), 156–162. https://doi.org/10.1006/meth.1999.0841.

(150) Vignaroli, G.; Iovenitti, G.; Zamperini, C.; Coniglio, F.; Calandro, P.; Molinari, A.; Fallacara, A. L.; Sartucci, A.; Calgani, A.; Colecchia, D.; et al. Prodrugs of Pyrazolo[3,4-d]Pyrimidines: From Library Synthesis to Evaluation as Potential Anticancer Agents in an Orthotopic Glioblastoma Model. *J. Med. Chem.* **2017**, *60* (14), 6305–6320. https://doi.org/10.1021/acs.jmedchem.7b00637.

(151) Zhang, Y.; Huo, M.; Zhou, J.; Xie, S. PKSolver: An Add-in Program for Pharmacokinetic and Pharmacodynamic Data Analysis in Microsoft Excel. *Comput. Methods Programs Biomed.* **2010**, *99* (3), 306–314. https://doi.org/10.1016/j.cmpb.2010.01.007.

(152) Fallacara, A. L.; Zamperini, C.; Podolski-Renić, A.; Dinić, J.; Stanković, T.; Stepanović, M.; Mancini, A.; Rango, E.; Iovenitti, G.; Molinari, A.; et al. A New Strategy for Glioblastoma Treatment: In Vitro and in Vivo Preclinical Characterization of Si306, a Pyrazolo[3,4-d]Pyrimidine Dual Src/P-Glycoprotein Inhibitor. *Cancers (Basel).* **2019**, *11* (6). https://doi.org/10.3390/cancers11060848.

(153) Matuszewski, B. K.; Constanzer, M. L.; Chavez-Eng, C. M. Strategies for the Assessment of Matrix Effect in Quantitative Bioanalytical Methods Based on HPLC-MS/MS. *Anal. Chem.* **2003**, *75* (13), 3019–3030. https://doi.org/10.1021/ac020361s.

(154) Sillén, L. G.; Martell, A. E.; Bjerrum, J. Stability Constants of Metal-Ion Complexes. *Stability Constants. Part I: Organic Ligands.*; Chemical Society Special Publication No. 6, Ed.; **1964**.

(155) Lasic, D.; Papahadjopoulos, D. *Medical Applications of Liposomes* **1998**. https://doi.org/10.1016/B978-0-444-82917-7.X5000-5.

(156) Daniel, M.C.; Astruc, D. Gold Nanoparticles: Assembly, Supramolecular Chemistry, Quantum-Size-Related Properties, and Applications toward Biology, Catalysis, and Nanotechnology. *Chem Rev.* **2004**, *104* (1), 293–346.

(157) Kimling, J.; Maier, M.; Okenve, B.; Kotaidis, V.; Ballot, H.; Plech, A. Turkevich Method for Gold Nanoparticle Synthesis Revisited. *J. Phys. Chem. B* **2006**, *110* (32), 15700–15707. https://doi.org/10.1021/jp061667w.

(158) He, Y. Q.; Liu, S. P.; Kong, L.; Liu, Z. F. A Study on the Sizes and Concentrations of Gold Nanoparticles by Spectra of Absorption, Resonance Rayleigh Scattering and Resonance Non-Linear Scattering. *Spectrochim. Acta - Part A Mol. Biomol. Spectrosc.* **2005**, *61* (13–14), 2861–2866.

https://doi.org/10.1016/j.saa.2004.10.035.

(159) Stiti, M.; Cecchi, A.; Rami, M.; Abdaoui, M.; Barragan-Montero, V.; Scozzafava, A.; Guari, Y.; Winum, J. Y.; Supuran, C. T. Carbonic Anhydrase Inhibitor Coated Gold Nanoparticles Selectively Inhibit the Tumor-Associated Lsoform IX over the Cytosolic Isozymes I and II. *J. Am. Chem. Soc.* **2008**, *130* (48), 16130–16131. https://doi.org/10.1021/ja805558k.

(160) Khan, A. K.; Rashid, R.; Murtaza, G.; Zahra, A. Gold Nanoparticles: Synthesis and Applications in Drug Delivery. *Tropical Journal of Pharmaceutical Research* **2014**, pp 1169–1177. https://doi.org/10.4314/tjpr.v13i7.23.

(161) Libutti, S. K.; Paciotti, G. F.; Byrnes, A. A.; Alexander, H. R.; Gannon, W. E.; Walker, M.; Seidel, G. D.; Yuldasheva, N.; Tamarkin, L. Phase I and Pharmacokinetic Studies of CYT-6091, a Novel PEGylated Colloidal Gold-RhTNF Nanomedicine. *Clin. Cancer Res.* **2010**, *16* (24), 6139–6149. https://doi.org/10.1158/1078-0432.CCR-10-0978.

(162) Joh, D. Y.; Sun, L.; Stangl, M.; Al Zaki, A.; Murty, S.; Santoiemma, P. P.; Davis, J. J.; Baumann, B. C.; Alonso-Basanta, M.; Bhang, D.; et al. Selective Targeting of Brain Tumors with Gold Nanoparticle-Induced Radiosensitization. *PLoS One* **2013**, *8* (4). https://doi.org/10.1371/journal.pone.0062425.

(163) Huo, S.; Ma, H.; Huang, K.; Liu, J.; Wei, T.; Jin, S.; Zhang, J.; He, S.; Liang, X. J. Superior Penetration and Retention Behavior of 50 Nm Gold Nanoparticles in Tumors. *Cancer Res.* **2013**, *73* (1), 319–330. https://doi.org/10.1158/0008-5472.CAN-12-2071.

(164) Yamamoto, T.; Nakai, K.; Tsurubuchi, T.; Matsuda, M.; Shirakawa, M.; Zaboronok, A.; Endo, K.; Matsumura, A. Boron Neutron Capture Therapy for Newly Diagnosed Glioblastoma: A Pilot Study in Tsukuba. *Appl. Radiat. Isot.* **2009**, *67* (7-8 SUPPL.). https://doi.org/10.1016/j.apradiso.2009.03.011.

(165) Honary, S.; Zahir, F. Effect of Zeta Potential on the Properties of Nano-Drug Delivery Systems - A Review (Part 1). *Trop. J. Pharm. Res.* **2013**, *12* (2), 255–264. https://doi.org/10.4314/tjpr.v12i2.19.

(166) Calgani, A.; Vignaroli, G.; Zamperini, C.; Coniglio, F.; Festuccia, C.; Cesare, E. Di; Gravina, G. L.; Mattei, C.; Vitale, F.; Schenone, S.; et al. Suppression of SRC Signaling Is Effective in Reducing Synergy between Glioblastoma and Stromal Cells. *Mol. Cancer Ther.* **2016**, *15* (7), 1535–1544. https://doi.org/10.1158/1535-7163.MCT-15-1011.

(167) Coppola, C.; Rienzo, A.; Piscopo, G.; Barbieri, A.; Arra, C.; Maurea, N. Management of QT Prolongation Induced by Anti-Cancer Drugs: Target Therapy and Old Agents. Different Algorithms for Different Drugs. *Cancer Treatment Reviews* **2018**, pp 135–143. https://doi.org/10.1016/j.ctrv.2017.11.009.

(168) Curigliano, G.; Lenihan, D.; Fradley, M.; Ganatra, S.; Barac, A.; Blaes, A.; Herrmann, J.; Porter,

C.; Lyon, A. R.; Lancellotti, P.; et al. Management of Cardiac Disease in Cancer Patients throughout Oncological Treatment: ESMO Consensus Recommendations. *Ann. Oncol.* **2020**, *31* (2), 171–190. https://doi.org/10.1016/j.annonc.2019.10.023.

(169) Gintant, G.; Sager, P. T.; Stockbridge, N. Evolution of Strategies to Improve Preclinical Cardiac Safety Testing. *Nature Reviews Drug Discovery* **2016**, pp 457–471. https://doi.org/10.1038/nrd.2015.34.

(170) Scuoppo, C.; Wang, J.; Persaud, M.; Mittan, S. K.; Basso, K.; Pasqualucci, L.; Rabadan, R.; Inghirami, G.; Grandori, C.; Bosch, F.; et al. Repurposing Dasatinib for Diffuse Large B Cell Lymphoma. *Proc. Natl. Acad. Sci. U. S. A.* **2019**, *116* (34), 16981–16986. https://doi.org/10.1073/pnas.1905239116.